LBL-19287

MUOPRODUCTION OF J/ψ (3100)

Thomas Walter Markiewicz

Lawrence Berkeley Laboratory
University of California
Berkeley, CA 94720

October 1981

AAB-5177

This work was funded by the Director, Office of Energy Research,
Office of High Energy and Nuclear Physics, High Energy Physics Division
of the United States Department of Energy under Contract No. DE-AC03-76SF00098.

MUOPRODUCTION OF $J/\psi(3100)$

Thomas Walter Markiewicz

ABSTRACT

Interactions of 209-GeV muons within an instrumented magnetized-steel calorimeter have produced 4374 ± 87 $\mu^+\mu^-$ pairs from J/ψ decay, corresponding to the cross section $\sigma(\mu N \to \mu\psi X) = 0.64 \pm 0.10$ nb. These interactions are classified as either elastic ($\sigma = 0.36 \pm 0.07$ nb) or inelastic ($\sigma = 0.28 \pm 0.06$ nb) based primarily on the calorimetric determination of E_X. The cross section for elastic ψ production by virtual photons, $\sigma_{eff}(\gamma_V N)$, rises with energy ν as $\log \nu$. Its dependence on Q^2 fits the vector-meson dominance form $P(\Lambda) = (1 + Q^2/\Lambda^2)^{-2}$, with $\Lambda = (2.0 - 2.4) \pm 0.15$ GeV, where the spread in values arises from considering the possibility of a Q^2 dependence in the decay angular distribution $W(\theta, \phi)$ and in the nuclear shadowing factor. We find that $W(\theta, \phi)$ is consistent with the form expected if the reaction $\gamma_V N \to \psi N$ conserves helicity in the s channel through natural-parity exchange in the t channel. After correction for nuclear effects, $d\sigma_{eff}/dt$ is described by the sum of two exponential terms in t, with average t slope $b = 2.56^{+0.35}_{-0.32}(stat.)^{+0.21}_{-0.17}(syst.)$. The photon-gluon fusion ($\gamma g \to \psi$) perturbative quantum chromodynamic model for ψ production provides an excellent description of the ν dependence of σ_{eff}, but cannot simultaneously explain the observed cross section and value of Λ. The differential cross section $d^2\sigma_{eff}/dz dp_\perp^2$ for inelastically produced ψ's rises approximately linearly with elasticity $z \equiv E_\psi/\nu$. The $p_\perp^2$ dependence is flatter than that of $d\sigma/dt$ for elastic events, with average $p_\perp^2$ slope $b = 1.46 \pm 0.10$. The Q^2 dependence of σ_{eff} is that of $P(\Lambda)$ with $\Lambda = 3.0 \pm 0.2$ GeV, and the ν dependence is similar to that observed for elastic production. The shapes of these distributions are well described by perturbative QCD calculations that consider the funadamental subprocess in the interaction to be $\gamma g \to \psi g$, but the absolute cross section is 5.5 times higher than predicted.

To my parents

CONTENTS

Acknowledgements v

I. INTRODUCTION 1

I.1 Vector Meson Dominance 3

I.1.1 Virtual Photon Flux Factors 4

I.1.2 The Optical Model 4

I.1.3 The Angular Distribution of Dimuons in ψ Decay 6

I.2 Perturbative Quantum Chromodynamics 8

II. APPARATUS 13

II.1 The Muon Beam 14

II.2 The Magnet 16

II.3 The Calorimeter 18

II.4 The Trimuon Trigger 19

II.5 The PC-DC System 21

II.5.1. PC Construction 21

II.5.2. The Drift Chamber System 24

II.6 Data Acquisition 24

III. ANALYSIS 26

III.1 Reconstruction 28

III.1.1 Track Finding 28

III.1.2 Vertex Finding with the Calorimeter 28

III.2 Momentum Fitting 29

III.3 Analysis 30

III.3.1 Calculation of E_{cal} 30

III.3.2 Calorimeter Calibration 30

III.3.3 Constraining Events Kinematics with the Calorimeter 31

III.3.4 Spectator Algorithm 31

III.3.5 Background Subtraction; The Dimuon Mass Distribution 31

III.4 Acceptance Calculation 33

III.4.1 The Apparatus Simulation 34

III.4.2 Elastic Event Generator 36

III.4.3 Inelastic Event Generator 38

III.4.4 Extraction of Results 40

III.5 Analysis Cuts 41

III.6 Systematic Effects 43

III.6.1 Radiative Corrections 43

III.6.2 Nuclear Shadowing 44

IV. ELASTIC RESULTS 46

IV.1 Muoproduction Cross Section 46

IV.2 The t distribution 47

IV.3 The Q^2 and Angular Distributions 53

IV.4 The E_γ Distribution and its Variation with Q^2 58

V. INELASTIC RESULTS 62

V.1 The Muoproduction Cross Section 62

V.2 The Elasticity Distribution 65

V.3 The Angular Distribution of $\psi \to \mu^+\mu^-$ 66

V.4 The $p_\perp^2$ distribution 67

V.5 The Q^2 Distribution 69

V.6 The E_γ Distribution 71

VI. SUMMARY and CONCLUSIONS 74

APPENDIX A. The Angular Distribution of Di-leptons

in the Decay of Leptoproduced Vector Mesons 82

A.1 Kinematics 82

A.2 General decay angular distribution of $\psi \to \mu^+\mu^-, e^+e^-$ 84

A.3 General result for unpolarized incident leptons 86

A.4 General result for longitudinally polarized incident leptons 87

A.5 The decay angular distribution in the case of

natural parity exchange and s–channel helicity conservation 88

REFERENCES 91

TABLES 98

FIGURES 118

ACKNOWLEDGEMENTS

The design, construction, operation, and analysis of this experiment has occupied the majority of my waking hours for the last seven years. Its a great relief to me that its finally over. While most physicists today, myself included, lament the ever increasing size of the collaborations required to carry out modern high energy physics experiments, I can't help but feel that this experiment would have benefited from some additional manpower. This makes me very appreciative of all those people that actually did contribute their time and talent to making the experiment the success I think it is. The support of the group members from Berkeley, Fermilab, and Princeton transformed what could have been an ordeal into an enjoyable, educational experience.

I owe my greatest debt to the physicists from Berkeley: Al Clark, Karl Johnson, Roy Kerth, Stew Loken, Peter Meyers, Wes Smith, Bill Wenzel, and especially my advisor, Mark Strovink. Mark in particular devoted his considerable drive and problem-solving genius to the experiment from its inception to the publication of its final results, an increasingly rare phenomenon. Stu can probably get more accomplished per unit time than any physicist I've met. More than anyone else, in name and fact, he was the Person-In-Charge during the assembly and running of the experiment. Peter Meyers, through his cleverness, thoroughness, and razor-like ability to seperate wishful thinking from proven fact has influenced these results greatly. No aspect of the experiment escaped his ascerbic wit.

The support personel from Lawrence Berkeley Laboratory merit special mention. The technical expertise of Fred Goozen, Ducky Lucas, Tim Nuzum, and Tom Weber was invaluable. I am convinced that no mechanical problem exists that Fred cannot sovle elegantly. John Caron provided sophisticated programming support during the final data analysis at L.B.L. Teri Martin handled administrative details for most of the experiment. Donna Vercelli is responsible for typing most of

the dissertation, and Christopher T. Day and Ed Whipple were of great help in its typesetting.

The Fermilab group consisted of Rol Johnson, Craig Moore, Marshall Mugge, and Bob Shafer. Marshall, in particular, was indespensible to the experiment; he typically accounted for at least 1.5 full-time-equivalent physicists. Garvie Hale provided excellent on-site technical assistance at Fermilab. George Gollin, Frank Shoemaker, and Pam Surko made up the Princeton contingent. George, a fellow graduate student, was responsible for most of the dimuon analysis referred to so often in the text.

This work was funded by the Director, Office of Energy Research, Office of High Energy and Nuclear Physics, High Energy Physics Division of the United States Department of Energy under Contract No. DE-AC03-76SF00098.

I. INTRODUCTION

The discovery of the $J/\psi(3097)$ meson in both e^+e^- interactions[1] and proton–Be collisions[2] in 1974 ushered in a new era in our understanding of the fundamental forces governing the interactions of the elementary particles. In 1970 Glashow, Iliopoulos, and Maiani noticed[3] that the introduction of a fourth quark field[4] to the then standard SU(3) symmetric triplet of quarks[5] added terms to the weak hadronic charged current that would cancel amplitudes which gave rise, for example, to an anomalously large $K_L^0 - K_S^0$ mass difference[6] and $K_L^0 \to \mu^+\mu^-$ decay rate[7]. This new quark, carrying a charge of $+2/3$ and one unit of a new quantum number —charm, would eliminate strangeness changing neutral currents in the Weinberg–Salam model[8] of electro-weak interactions and bring a symmetry to the hadronic and leptonic sectors of the theory. After the discovery[9] of neutral weak currents in 1973 encouraged belief in gauge theories and charm, the extremely narrow width (63 KeV) of the 3.1 GeV resonance lead to its interpretation[10] as a bound state of the new c and $\bar{c}$ quarks. In 1976, peaks in the mass spectra of $K^-\pi^+$, $K^-\pi^+\pi^+\pi^-$, and $K^-\pi^+\pi^+$ events[11,12] produced in e^+e^- collisions at the 4.03 GeV resonance region provided final confirmation of the charm hypothesis. Because of the preferential strange quark to charm quark coupling in the weak current, these channels were expected[13] from the decay of D^0 and D^+ mesons composed of one "naked" c quark and one light ($\bar{u}$ or $\bar{d}$) antiquark.

In the period since 1974 many experiments have investigated the spectroscopy, production, and decay properties of the charmed particles. This paper reports the final results of the first experiment[14] to produce the $\psi(3097)$ through lepton-nucleon interactions. Using the Fermilab muon beam and the Berkeley-Fermilab-Princeton (BFP) Multimuon Spectrometer (MMS) the ψ's were produced in interactions of the form $\mu N \to \mu\psi X$ and detected through their $\psi \to \mu^+\mu^-$ decay mode. If we think of the ψ leptoproduction process as being intermediated by a spacelike virtual

photon of lab energy $E_\gamma = \nu$ and mass squared $q^2 \equiv -Q^2$ (Figure I.1) the data measured in this experiment complement the study of the charm system with timelike photons, as in e^+e^- interactions or in hadroproduction through the Drell-Yan process, and with real ($Q^2 = 0$) photons. The continuous Q^2 spectrum available in the μN interaction, however, allows for a measurement of the dependence of the ψ production on a dynamical variable inaccessible to the other types of experiment.

Theoretical interest in ψ muoproduction at this time arises because the ψ provides a simple, high mass system where the applicability of descriptions of the nature of matter on extremely small distance scales may be tested. Traditionally, the leptoproduction of the lighter mass vector mesons, $\rho(770)$, $\omega(783)$, and $\phi(1020)$ has been discussed in the framework of the Vector Meson Dominance (VMD) model[15–18]. While providing a qualitative physical picture of the process, the VMD model lacks the predictive power of a true theory of the strong interactions. Currently, the only available such theory is quantum chromodynamics[19–22] (QCD), wherein the strong interaction between pointlike quarks is said to be mediated by the exchange of colored gluons. The success of this theory in supplying testable predictions hinges on its ability to incorporate the concept of "asymptotic freedom" into its mathematical structure through a strong interaction coupling constant α_S, whose value depends on the mass scale M^2 of the problem being investigated. For sufficiently high mass scales $\alpha_S(M^2)$ is low enough that low order perturbation theory calculations should provide relevant predictions, once any appropriate fundamental parameters or distributions are specified. Because of this, however, it is difficult to separate any test of the QCD theory itself from that of the assumptions of a particular calculation. Below, after summarizing the aspects of the VMD approach used in the analysis, we will briefly describe the recently developed QCD based perturbative calculations which are later compared to the results of the experiment.

I.1 Vector Meson Dominance

The vector-meson dominance model was developed over the period from 1958 to 1962 as the result of attempts to explain the hadronic interaction properties[23] of the photon using either specific field theories[24] with vector mesons as the elementary constituents or the hypothesis that low mass vector meson poles dominate the dispersion relations[25] for the matrix elements of the electromagnetic current. The physical picture implied by the model for elastic ψ leptoproduction is shown in Figure I.2(a). The incident muon serves as a source of virtual photons which couple directly to off-shell ψ mesons. By exchanging momentum with the target the virtual ψ's are brought on-shell.

Quantitative predictions of the model arise from the assumption that the $\gamma_V - \psi_V$ coupling strength, denoted em_ψ^2/f_ψ, is approximately independent of Q^2. We then expect the simple propagator Q^2 dependence,

$$d\sigma/dt(\gamma_V N \to \psi N) = \left(\frac{e}{f_\psi}\right)^2 \left(\frac{m_\psi^2}{Q^2 + m_\psi^2}\right)^2 d\sigma/dt(\psi N \to \psi N), \qquad (I.1)$$

where $e^2 = 4\pi\alpha$ and f_ψ at any Q^2 is given by its value at $Q^2 = -m_\psi^2$, determined by, for example, measurement of the width for $\psi \to \mu^+\mu^-$. For ρ, ω, and ϕ production, the neglect of any Q^2 variation in the coupling constants from approximately -1 GeV^2 to $+1$ GeV^2, relative to that in the propagator term, has been justified by experiment. In the case of ψ production, however, the range of extrapolation is ~ 10 times as great, while the psi propagator term Q^2 variation is weaker, providing a more sensitive test of the VMD assumptions than has been previously available.

While the VMD model does not give predictions for the cross section's dependence on variables other than Q^2, it does provide a physical picture that is very useful in analyzing the ψ production process. For example, considering the virtual ψ-nucleon interaction as equivalent in first order to the scattering of two hard spheres suggests that the ψ production is predominately diffractive and thus can be described by the optical model. Similarly, if the $\gamma_V - \psi_V$ coupling is indeed direct, the polarization (helicity) state of the final state ψ should be related to that of the virtual photon

that produced it. In the following sections we discuss the supplementary assumptions to VMD that convert these unspecified relations into definite formulae.

I.1.1 Virtual Photon Flux Factors

In the one photon exchange approximation the differential cross section for electromagnetically producing ψ's has contributions from both of the photon's polarization states. We parameterize[26]

$$d^2\sigma/dQ^2d\nu = \Gamma_T\sigma_T + \Gamma_L\sigma_L,$$

where Γ_T (Γ_L) represents the flux of transversely (longitudinally) polarized virtual photons and σ_T (σ_L) the corresponding photon cross section. Typically we write

$$d^2\sigma/dQ^2d\nu = \Gamma_T\sigma_{eff}, \qquad \text{where} \quad \sigma_{eff} = (1+\epsilon R)\sigma_T.$$

Here $\epsilon \equiv \Gamma_L/\Gamma_T$ and $R \equiv \sigma_L/\sigma_T$. The transverse flux Γ_T is defined so as to allow $\sigma_T(\nu, Q^2 = 0)$ to be compared with the cross section for producing ψ's with real photons. We use

$$\Gamma_T = \frac{\alpha}{4\pi^2}\frac{K}{q^2}\frac{E'}{E}\left(\frac{2}{1-\epsilon}\right),$$

and

$$\epsilon = \left(1 + 2(1+\nu^2/q^2)\tan^2\frac{\Theta_V}{2}\right)^{-1},$$

where E is the beam energy and E' and Θ_V are energy and angle of the scattered muon (spectator) in the target rest frame. The quantity K must reduce to ν when $Q^2 \to 0$; we use the Hand convention[26], $K = \nu - Q^2/2m_n$, but other choices ($\sqrt{\nu^2+Q^2}$ for example) are equivalent for the kinematic range of the data.

I.1.2 The Optical Model

The square of the four momentum transferred from the virtual photon (or virtual ψ in the VMD picture) to the target in the ψ production process is defined as t. Its distribution is used to measure

the structure or size of the target. We denote the minimum value of t needed to bring the final state ψ on-shell as t_{min} and the maximum value of t allowed by the kinematics as t_{max}. In general, t is related to the $\gamma_V N$ center of mass (CM) scattering angle θ_{cm} via

$$t = t_{min} - 2p_{cm}^2(1 - \cos\theta_{cm}),$$

where p_{cm} is the momentum in the CM frame. The CM angular distribution $d\sigma/d\Omega_{cm}$ can then be related to $d\sigma/dt$ as

$$d\sigma/dt = \frac{\pi}{p_{cm}^2}\frac{d\sigma}{d\Omega_{cm}}.$$

In the optical model, the target is treated as the potential corresponding to a totally absorptive disk of area $O(R^2)$, whereupon $\sigma_{elastic}$ is caused by diffraction of the incident wave around the disk and $d\sigma/dt$ measures the size of the disk. Using the first Born approximation, one can show[27] that for small t,

$$d\sigma/dt = Ae^{bt}, \tag{I.2}$$

where b is proportional to R^2 and A is proportional to R^4. For elastic ψ production from a nuclear target we expect to see contributions to $d\sigma/dt$ from the large weakly bound Fe nuclei themselves (termed coherent production) at extremely small values of $|t|$, as well as from the individual nucleons (termed incoherent production) once the coherent term has diminished. Then,

$$d\sigma/dt = d\sigma/dt\,|_{t=0}\,(A_{eff}^2 e^{b_C t} + A_{eff} e^{b_I t}), \tag{I.3}$$

where b_C and b_I are the coherent and incoherent t slopes, respectively, and A_{eff} is the effective number of nucleons per Fe nucleus seen by virtual photons of the average Q^2 and ν of the experiment. The optical model thus specifies the functional form of $d\sigma/dt$ and fixes the relative size of the coherent and incoherent parts of $d\sigma/dt$ at $t = 0$.

An important goal of the first ψ photoproduction experiments[28–31] was to determine whether or not the ψ was a hadron. Since the optical theorem, which relates the imaginary part of the

elastic forward scattering amplitude to the total cross section, can be used to connect $d\sigma/dt(\gamma N \to \psi N)\,|_{t=t_{min}}$ to $\sigma_{tot}(\psi N)$, this was accomplished by comparing calculated values of $\sigma_{tot}(\psi N)$ to typical hadronic total cross sections. While the basic question has been answered, this experiment can also measure $\sigma_{tot}(\psi N)$ in an analagous manner for comparison. The necessary formalism is sketched below.

The optical theorem is

$$Imf(\theta)\,|_{\theta=0} = \frac{p_{cm}}{4\pi}\sigma_{tot}(\psi N).$$

Then, since

$$\frac{d\sigma}{d\Omega_{cm}} \equiv |f(\theta)|^2 = [Imf(\theta)]^2 + [Ref(\theta)]^2,$$

we have

$$d\sigma/dt(\psi_V N \to \psi N)\,|_{t=t_{min}} = \frac{\sigma^2_{tot}(\psi N)}{16\pi}(1+\beta^2),$$

where $\beta \equiv \frac{|Ref(0)|}{|Imf(0)|}$; $\beta = 0$ for purely diffractive processes. Using Eq. I.1 yields

$$d\sigma/dt(\gamma_V N \to \psi N)\,|_{t=t_{min}} = \frac{4\pi\alpha}{f^2_\psi}(1+Q^2/m^2_\psi)\frac{\sigma^2_{tot}(\psi N)}{16\pi}(1+\beta^2). \qquad (I.4)$$

Finally, the ratio of elastic to total ψN cross sections can be found in this picture by inserting the above equation into Eq. I.2 and integrating over t. The result is

$$\begin{aligned}\frac{\sigma_{elastic}(\psi N)}{\sigma_{tot}(\psi N)} &= \frac{1}{b}\frac{e^{-bt_{min}}}{16\pi}\sigma_{tot}(\psi N)\\ &= \frac{1}{b}\frac{e^{-bt_{min}}}{16\pi}\left[\frac{f^2_\psi}{4\pi\alpha}\frac{16\pi}{(1+\beta^2)}d\sigma/dt(\gamma N \to \psi N)\,|_{t=t_{min}}\right]^{\frac{1}{2}}.\end{aligned} \qquad (I.5)$$

I.1.3 The Angular Distribution of Dimuons in ψ Decay

The general form[32] for the angular distribution W of dimuons from ψ decay involves 36 different density matrix elements. If it happens, however, that the polarization of the final state ψ is simply related to that of the exchanged virtual photon, that is, if ψ–N elastic scattering conserves helicity

in some way, then the problem can be reduced to one containing only a small number of independent parameters that are simply related to σ_L and σ_T.

Three models for helicity conservation are often mentioned[33]: s–channel helicity conservation (SCHC), t–channel helicity conservation (TCHC), and the spin independence model (SIM). Each corresponds to a distinct physical picture of how the final state ψ polarization is related to that of the virtual photon. To simplify W we will use the SCHC model, as it has been observed[34–36] that the angular distribution of pions from the decay of electroproduced ρ, ω, and ϕ mesons are consistent with that hypothesis and the additional assumption of natural parity exchange (NPE). In the SCHC picture, helicity eigenstates with $\hat{z}$ defined along $\hat{p}_{\gamma_V}$ in the $\gamma_V N$ center of mass (c.m.) (the s–channel c.m. helicity system) produce helicity eigenstates with $\hat{z}$ defined along $\hat{p}_\psi$ in the $\psi N'$ c.m. (or equivalently, the ψ rest frame with $\hat{z} = -\hat{p}_{N'}$, here called the ψ helicity frame). NPE (as opposed to unnatural parity exchange) assumes that the reaction $\gamma_V N \to \psi N'$ proceeds via the t channel exchange of a particle with parity $P = (-1)^J$.

SCHC and NPE provide the relations among the matrix elements that reduce the 36 original amplitudes to the two amplitudes for ψ production by Γ_L and Γ_T. The final solution is represented in terms of the squares of these amplitudes, σ_L and σ_T, and their relative phase, δ. In Appendix A the general solution is presented, and the SCHC and NPE hypotheses applied, to calculate the expected distribution of dimuons from ψ decay,

$$\begin{aligned} W(R;\theta,\phi) = \frac{3}{16\pi}\frac{1}{1+\epsilon R}[&(1+\cos^2\theta) + 2\epsilon R\sin^2\theta - \epsilon\sin^2\theta\cos 2\phi \\ &+ \sqrt{2\epsilon R(1+\epsilon)}\sin 2\theta\cos\delta\cos\phi - H\sqrt{2\epsilon R(1-\epsilon)}\sin 2\theta\sin\delta\sin\phi]. \end{aligned} \tag{I.6}$$

Here θ is the polar angle of the beam-sign daughter muon in the ψ helicity frame, and $\phi = \phi_2 - \phi_1$ is the difference between the two physical azimuthal angles in the problem: ϕ_2, the azimuthal angle of the ψ decay plane, measured with respect to the $\gamma \to \psi$ production plane, and ϕ_1, the azimuthal angle of the $\gamma \to \psi$ production plane measured relative to the beam muon scattering plane. Figure I.3 illustrates these angles[37]. H is the muon beam longitudinal polarization, which is approximately equal to 0.8.

It is interesting to note that this form of $W(\theta, \phi)$ remains unchanged if we decide to abandon SCHC in favor of TCHC or SIM, as long as θ, ϕ_2, amd ϕ_1 are defined in the appropriate coordinate systems (use, for example, the ψ rest frame with $\hat{z} = \hat{p}_\gamma$ for the SIM). Experiments seeking to decide among these choices, or desiring to measure quantitatively the level to which any model is true find it more convenient to express W directly in terms of the original density matrix elements and to measure the level at which certain elements, predicted to vanish in a particular model, are ruled out.

I.2 Perturbative Quantum Chromodynamics

There are two fundamental assumptions underlying the current perturbative QCD approaches to ψ photoproduction. The first is that the c and $\bar{c}$ quarks of the ψ are not present in the wavefunctions of the interacting particles but are instead produced during the scattering process[38]. That is, any contribution due to an intrinsic charmed sea in the nucleon is ignored. The second assumption involves the distance (mass) scale appropriate to the problem. It is argued[39] that if the virtual photon fluctuates into a $c\bar{c}$ pair, the pair will propagate a distance on the order of

$$\Delta x \sim \frac{1}{\Delta p} \sim (Q^2 + 4m_c^2)^{-\frac{1}{2}} \sim \frac{1}{m_\psi},$$

and then materialize after scattering with a nucleon constituent, if the photon's energy is sufficiently high. The mass scale of the problem is thus set by m_c, not Q^2, and $\alpha_S(m_c^2)$ should be small enough to justify low order perturbation theory. By allowing the photon and nucleon constituents (partons) to interact according to the Feynman rules for QCD and folding in the assumed parton distribution functions, cross sections for $c\bar{c}$ production can be calculated.

The first calculations[40–47] of heavy quark photoproduction within this framework assumed that the dominant process is the fusion of the photon with a gluon in the nucleon, as shown in Figure I.2(b). In this picture, termed the photon-gluon fusion (γGF) model, the scattering amplitudes are

proportional to $\alpha\alpha_s$. As drawn in Figure L2(b) the final $c\bar{c}$ state is a color octet, since the exchanged gluon is itself colored. To produce color singlet hadrons, at least one other gluon must be exchanged. This color rearrangement is assumed to occur with unit probability and not affect the validity of the calculation.

The assumption that momentum is transferred to the nucleon target via the exchange of one massless gluon implies that

$$2p_i \cdot q = 2m_n \nu x = m_{c\bar{c}}^2 + Q^2,$$

and that

$$t = (p_n - p_{n'})^2 = m_g^2 = 0.$$

Here, $x \equiv p_i/p$ is the fraction of the target's momentum carried by the gluon. The x distribution, $G(x)$, and the value of m_c are inputs to the model. The form of $G(x)$ typically used is

$$G(x) = 0.5(\eta + 1)\frac{(1-x)^\eta}{x}, \tag{I.7}$$

where $\eta = 5$, as suggested by power counting arguments[48], and where the normalization is chosen so that the gluons account for half of the nucleon's momentum. The value of m_c used in the "standard" calculation is

$$m_c = 1.5 \text{ GeV} \simeq \frac{1}{2} m_\psi.$$

To the extent that the variation of $m_{c\bar{c}}^2 + Q^2$ in the data can be neglected compared to that of ν, $G(x)$ determines the energy dependence of the cross section. Its Q^2 behavior is dominated by the size of m_c.

As thus formulated, the γGF model describes *elastic* $c\bar{c}$ production only. While not specifying the color rearrangement mechanism limits predictions of ψ helicity and $d\sigma/dt$, once $G(x)$ and m_c are specified, definite predictions[49–51] for $\sigma_T(Q^2, \nu)$, $\sigma_L(Q^2, \nu)$, and $d\sigma/dm_{c\bar{c}}^2$ are obtained. To restrict its predictions for inclusive $c\bar{c}$ production to particular bound states, such as the ψ, an additional

assumption[38], known as semi-local duality (SLD), is required. It is prescribed that any bound state cross section is found by integrating $d\sigma/dm^2_{c\bar{c}}$ from the lower kinematic limit of $4m_c^2$ to the threshold for open charm ($D\bar{D}$) production $4m_D^2$, divided by the number of states f in that range. It is unfortunate that an experiment restricted to ψ production complicates a test of fundamental short distance ideas with that of the semi-local duality assumption. Taken literally, SLD predicts that each $c\bar{c}$ state will be photoproduced equally, regardless of its spin and parity. Then $f_{c\bar{c}\to\psi}$ and $\alpha_S(m^2_{c\bar{c}})$ will uniquely determine the normalization of the calculated cross section. Typically $f_{c\bar{c}\to\psi}$ is taken as $\frac{1}{6}$ – $\frac{1}{8}$. We will use $\frac{1}{8}$ in our "standard" calculation. α_S is calculated via

$$\alpha_S(m^2) = \frac{12\pi}{(33-2n)\ln(m^2/\Lambda^2)}, \tag{I.8}$$

with the number of active flavors $n = 4$, and the empirical scale parameter $\Lambda = 0.5$ GeV. Then $\alpha_S(m^2_\psi) \simeq 0.4$. We compare the γGF model described by Reference 50 and the above assumptions to the experiment's data on elastic ψ production. A less dogmatic approach[52] takes f as an a *priori* unknown parameter proportional to the density of $c\bar{c}$ states near the ψ and fixed by the experimentally measured cross section. This conceptual retreat allows the remaining fraction $1-f$ of the cross section below D threshold to appear in the open charm channel, rather than in ψ', χ, or η_c states.

The predictive limitations of the γGF approach can be viewed as the unfortunate by-product of the desire to make the calculation tractable. With the above assumptions, simple integral formulae for the differential cross sections are indeed available[46,50]. More recently, however, attempts[53–59] have been made to calculate non-diffractive and inelastic $c\bar{c}$ production within the same framework by considering specific subprocesses that are second order in α_S. While the earlier of these[53–56] limited their attention to manageable subsets of the second order diagrams, the most recent[57,59] by D.W. Duke and J.F. Owens encompass the complete set of subprocesses shown[60] in Figure I.4. In this general case inelastic ψ production occurs when a hard gluon or light quark appears in the final state. Elastic $c\bar{c}$ production is treated as one kinematic limit of all $c\bar{c}$ production, defineable

by whatever cuts an experiment might use to isolate an elastic sample. The duality assumption desribed above is used to restrict the model to ψ production, and while two gluon diagrams are included in the calculation, it is still not required that the $c\bar{c}$ system form a color singlet at the perturbative level – the color rearrangement being accomplished by soft gluons with unit probability. The algebraic difficulty in this general approach, involving 12 interfering amplitudes, necessitates a computer generated solution with graphical presentation of results. Both this fact and the recent nature of the calculation have prevented us from comparing our data with this model in more than a passing fashion.

A calculation[55] of inelastic ψ photoproduction through the 6 QCD subprocesses shown in Figure 1.4(a)–(c) has been presented by E. Berger and D. Jones. Analytic expressions for the differential photon cross section are given as a function of ν, the square of the ψ's transverse momentum with respect to the incident photon direction, $p_\perp^2$, and the elasticity, z, defined as $(E_\psi)_{lab}/\nu$. These predictions will be labeled as "$\gamma g \rightarrow \psi g$" in the following text. In addition to the choice of fundamental subprocesses included, certain conceptual differences exist between the $\gamma g \rightarrow \psi g$ calculation and that of the recent extensions of γGF. The first question is whether or not color must be conserved at the level of the perturbative calculation. Instead of allowing unspecified final state interactions involving gluons to produce the color singlet hadrons, as in γGF, the $\gamma g \rightarrow \psi g$ calculation abandons the semi-local duality prescription in favor of a representation of the final $c\bar{c}$ state by a definite color singlet, $J^P = 1^-$ wavefunction, normalized to produce the correct ψ leptonic width $\Gamma(\psi \rightarrow e^+e^-)$. Secondly, it is claimed by Berger and Jones that the use of perturbative QCD for ψ production is only applicable when both gluons in the process are hard enough to both justify the use of a parton model of hadron constituents and allow specific hadronic exclusive channels, such as $\gamma N \rightarrow \psi N$ or $\gamma N \rightarrow \psi N^*$, to be ignored. By placing conditions on the square of the momentum transfer to the nucleon, $|t| > 1$ GeV^2, and the mass of the state recoiling against the ψ, $m_X > 2$ GeV, similar to restrictions placed on the parton description of deep inelastic scattering, they limit the claimed region of validity of their own result to the elasticity region $z < 0.9$ and suggest that

all purely elastic calculations are invalid.

The $\gamma g \rightarrow \psi g$ calculation assumes $xG(x) = 3(1-x)^5$, $m_g = 0$, $m_c = m_\psi/2$, and $\alpha_S = 0.3$. In this form it is compared to the inelastic ψ production results from this experiment. Despite the above noted differences, to first order, except for overall normalization and the shape of $d^2\sigma/dzdp_\perp^2$ at high z, this model's predictions are qualitatively consistent with those of the generalized γGF calculations . The conclusions drawn from comparing data to it can be considered as applicable to the general perturbative QCD approach.

II. APPARATUS

The experiment was performed in the muon beam at the Fermi National Accelerator Laboratory using a newly constructed apparatus specifically designed for the study of rare muon induced reactions, particularly those characterized by having more than one muon in the final state. Data were taken at an average incident beam energy of 214 GeV, with typical fluxes of $1\text{–}2 \times 10^6$ muons/sec.

The detector, which also served as the target, is shown in Figure II.1. It consists of 90 magnetized steel plates of dimensions 8 ft $\times$ 8 ft $\times$ 4 in, instrumented with both plastic scintillator counters for triggering and calorimetry, and multi-wire proportional (PC) and drift chambers (DC) for tracking muons. The magnetic field of 19.6 kG is excited in the vertical direction by a coil run through vertical slots cut into each plate.

The Fe plates are arranged in 18 groups of 5 plates, called modules. Behind each module is a PC, measuring coordinates along 3 axes - parallel, perpendicular, and diagonal (x, y, and u, respectively) to the bending plane of the magnet, and a DC, providing better resolution in the x direction. After modules 4, 6, 8, ..., 18 are banks of 12 plastic scintillators for counting final state muons and triggering the apparatus. Mounted behind each of the first 75 steel plates is a large plastic scintillator; these counters serve as hadronic calorimeter and vertex detector. An elevation view of one module of the apparatus is shown in Figure II.2.

The most important features of the apparatus for the ψ production study are the distributed nature of the steel target, the non-toroidal geometry, and the full sensitivity of all detectors both inside and away from the beam region. The first 14 modules serve as target for the experiment. Muons arising from interactions in these plates are detected and measured by that part of the apparatus downstream of the vertex. The use of steel as the target medium is dictated by the desire to have a high integrated luminosity for the study of rare processes. By distributing the target

uniformly throughout the apparatus this is achieved while maintaining a high event acceptance that varies only slowly with outgoing muon scattering angle.

Because $\Gamma_T(Q^2) \sim 1/Q^2$, the beam muon in most $\mu N \rightarrow \mu\psi X$ events tends to scatter near the forward direction. Since the PC, DC, and counter systems do not need to be deadened in the beam region to handle the available flux of muons, the scattered muon ("spectator"), as well as the ψ daughter muons, can be used in the trigger and tracked in the spectrometer. This results in an acceptance that is approximately flat in Q^2 (Sec.III.4.3). Moreover, by measuring the momenta of all final state muons magnetically, as well as the energy E_X of any hadronic shower, a one constraint fit can be applied to the event kinematics, improving the spectrometer's ν resolution at low ν (Sec.III.3.3).

These features make the apparatus unique and well suited for the study of multi-muon physics. A description of the beam system, the various subsystems of the apparatus, and the ψ event trigger follow.

II.1 The Muon Beam

The 400-GeV beam of the Fermilab proton synchotron was extracted and focused on a 30-cm aluminum target to produce high energy pions and kaons. These secondaries were focused into a 400-meter evacuated pipe where π, $K \rightarrow \mu\nu$ decays occurred. Resulting muons of the desired energy were then extracted into the N1 beam line and transported to the muon laboratory, where the Chicago Cyclotron Magnet (CCM) bent them into the MMS.

The beam optics have been described in detail elsewhere[61]. Briefly, four sets of dipole magnets were used for the initial momentum selection, the minimization of muon halo (i.e., muons that have been bent or multiple scattered out of the beam line yet penetrate into the muon laboratory), and the final momentum determination. Hadron contamination was minimized by the use of 23 meters of high density polyethelene (CH_2) absorber. One triplet of quadrupole magnets (immediately

downstream of the production target) and three quadrupole doublets focused the beam through the various apertures and onto the MMS.

The design resulted in a muon momentum acceptance of $\pm 2.5\%$ and a low ($\pi/\mu \sim 10^{-7}$) hadron beam component[61] at the expense of muon intensity and halo. Multiple scattering in the CH_2 absorber was the primary cause of the beam halo. There were as many halo muons outside as there were beam muons inside the 8.0 inch high by 13.5 inch wide aperture defining the beam at the apparatus. The yield of positive (negative) muons per incident proton was $\sim 10^{-7}$ ($\frac{1}{3} \times 10^{-7}$). Typically, 1–2$\times 10^{13}$ protons were extracted onto the production target during a 1 sec period ("spill") every 10 sec. The resulting μ^+ intensity for beam passing all vetoes was 1–2$\times 10^6$ muons/sec.

The system used for defining the beam and measuring its momentum is shown in Figure II.3. In order to maintain the possiblity of simultaneously running an upstream experiment using the CCM, the MMS was installed at an angle of 8 mrad with respect to the beam as it entered the muon laboratory. The CCM field integral was set to supply a compensating bend to the beam. Thus two magnets were available for beam momentum determination — the CCM and the last set of dipoles (D104) of the beam line.

Beam x coordinates upstream of the CCM were measured by 2 sets of 2 PC's bracketing the D104 magnets; y coordinates were measured with 2 PC's downstream of D104. These were identical 6 inch by 6 inch uni-directional chambers employing 2 sets of offset wire planes. The wire spacing was 2 mm; the offset was 1 mm. Each chamber had a corresponding hodoscope of six 1 inch wide plastic scintillator counters (BH), aligned so as to shadow groups of PC wires. An eight segment open center "Jaw" counter (V_J) immediately downstream of the last D104 magnet was used to tag events where a beam muon might have scraped through the magnet aperture.

In the area immediately upstream of the MMS were another set of counters and PC's for beam definition. Two multiplane (x, y, and u) PC's provided spatial information. These chambers were 1 meter$\times$1 meter in area with 2 mm wire spacing. Except for sharing adjoining cathodes, the chamber signal (anode) planes were essentially independent and employed voltage sensitive preamplifier-latch

circuitry. A large 10 ft high by 24 ft wide wall (V_W) of 64 plastic counters (provided by the upstream experiment E444, a Chicago-Harvard-Illinois-Oxford collaboration) with a 8 ft high by 4 ft wide central opening was used as a beam halo veto in conjunction with smaller overlapping group of 18 counters (V_h) having a $9\frac{3}{8}$ in high by $14\frac{13}{16}$ in wide beam hole. Pulse height measurements in four 1 in thick counters (V_b), designed for signal uniformity in the beam area, were used as part of a system that vetoed events caused by more than one in-time muon . An x–y hodoscope of 8 vertical and 6 horizontal 1.55 in wide counters ($BH(x,y)$) served as the final target for beam alignment. One and only one count was demanded in each plane so as to veto spatially separated but in-time muons. Finally, a $8\frac{1}{4}$ in high by $12\frac{5}{16}$ in wide counter (BH) provided the final beam definition aperture for the experiment.

For most of the data reported here the CCM was run at 3100 amperes with a resulting field integral of 5.9686 kG-m. The measured field integral of the D104 magnets was 20.59 kG-m. The beam momentum was measured as 214 GeV/c with a $\pm 2\%$ width at half maximum.

II.2 The Magnet

The iron plates used in the MMS were manufactured at a steel mill[62] in five separate "heats" of the furnace. The steel was rolled to a nominal 4 in thickness, and flame cut to the size of 8 ft by 8 ft. The coil slots in each plate were also cut by a computer controlled flame-cutter and samples from the resulting scraps used for measurements of magnetic susceptibility μ.

A total of 91 plates were used in the spectrometer. These were arranged in 18 groups of 5 plates with the extra plate (plate 0) placed 10 in upstream of the first module. While this extra plate helped minimize magnetic field edge effects in the spectrometer and absorb incident hadrons and delta rays, its use was dictated more by its availability than by necessity. Ideally, each module would have 1.25 inch gaps between the plates for the calorimeter counters, followed by a 10 inch gap for the trigger counter–PC–DC package (Figure II.2). While variations in plate thickness and

warping caused fluctuations in these numbers, the wire chamber to wire chamber repetition distance was maintained at 35.000 ± 0.016 in. Substantial design effort was expended in minimizing this number, as it controls both the average density of the spectrometer (and thus susceptibility to π, K meson decays) and the maximum Q^2 accepted. Measurements of each plate's spatial parameters and magnetic susceptability were taken and the modules assembled so that they would be as identical as possible. The mean plate thickness was 4.040 in. The entire spectrometer weighed approximately 4.32×10^5 kg or 475 tons.

The coil slots (Figure II.4) were designed[63] to maximize the uniformity of the vertical field in the central region of each plate covered by the wire chambers (41.5-in wide by 71.2-in high). The coil itself was composed of 18 turns of 0.75-in square water cooled copper. Each 9 by 1 turn package was pulled to the outer corners of its slot by banding straps and interconnected so that current flowed in both upper and lower loops with the same sense of circulation. The coil power supply was operated at 4000 amperes (60 volts), driving the iron well into its magnetic saturation region and producing a field in the vertical direction. The sign of the field was periodically ($\sim$ once per day) reversed to minimize the effect of any systematic left-right difference in the apparatus.

The components of the magnetic field in the x-y plane of each module were mapped using both Hall probes and a rotating flip-coil. In addition, measurements of the induced voltage in flux loops wrapped in 12 orientations about each module when the magnet supply was ramped from —4000 amp to +4000 amp provided absolute field normalization and constraints on the field map. One large flux loop around the entire magnet gave the overall field normalization for the experiment. All measurements were constrained to satisfy Maxwell's equations and a detailed field map produced.[63] The average field was 19.65 kG, implying that each module provided a transverse momentum kick of 0.300 GeV/c. The field was uniform throughout the fiducial region of the spectrometer to 3% and mapped to 0.2%. Unconstrained fits to the ψ peak of the dimuon mass distribution (Sec. III.3.5) gave $m_\psi = 3.090 \pm 0.010$ GeV, giving independent information on the accuracy of the field measurement.

Since three consecutive banks of trigger counters are required for the ψ trigger (Sec.II.5) only

the first 14 modules (and plate 0) are available as a target. The total amount of target material in this region is 5.6 kg/cm^2. Given the total number of incident muons in the data presented here, this corresponds to an integrated luminosity of $\mathcal{L} = 1000$ events/nb. Additional fiducial cuts in z (Sec. III.5) in the ψ data analysis reduce these numbers slightly.

II.3 The Calorimeter

The use of sampling calorimeters for the measurement of hadronic energy in inelastic scattering events has been widespread.[64] The combination of the 4-in thick Fe plates and plastic scintillator employed in this experiment is typical of such devices. The technique involves sampling the number of particles along the length of a shower induced by the primary hadrons produced in a muon interaction and calibrating the total number seen versus energy. The primary figure of merit is its resolution, generally parameterized as $\sigma(E)/E \simeq a/\sqrt{E}$, where typically $a \sim 1$. Design considerations include: high average calorimeter density (to prevent decays occurring before the hadrons interact), number of samples obtained (thickness of shower medium), transverse size of counters (to minimize leakage), and the spatial uniformity, efficiency, time stability and dynamic range of the counters.

In this experiment we use 31.5-in high by 48-in wide plastic scintillation counters mounted after the first 75 steel plates of the apparatus. They are read out on one side with RCA 6655 photomultiplier tubes mounted on 36-in long ultra-violet absorbing (UVA) triangular light pipes. Counter spatial uniformity was measured with both cosmic rays and a source and found to be between 15 and 30%. Adjacent counters were read out on alternate sides of the beam to further enhance uniformity. Shower leakage, given the muon beam's transverse dimensions, was determined by simulating inelastic muon scattering and shower propagation and found to be less than 10%. The same simulation indicated that only a 10% improvement in resolution at high energies would be obtained by sampling every 2 inches. By taking signals from both the anode and last dynode of each phototube, amplifying the former 25 times, and measuring the signal on each with a 1024 channel

LRS 2249 analog-to-digital converter (ADC), we could detect from 1 to 1500 minimum ionizing particles in each counter. The sensitivity in the high resolution ADC was sufficient to allow us to use the difference between 1 and 3 minimum ionizing particles as a tool in determining the z vertex location of elastic ψ events. An amplified output signal was also used as part of the hadronic shower requirement in the experiment's di-muon trigger, described in detail in Reference 65.

The calibration of the calorimeter is described in Sec III.3.2. When complete we find that $\sigma(E) = 1.5\sqrt{E(\text{ GeV})}$, with a minimum value for σ of 2.5 GeV.

II.4 The Trimuon Trigger

The experiment ran with three simultaneous event triggers, basically corresponding to the number of muons observed in the final state, as well as a trigger which gathered a sample of beam particles for later use in simulations. The single muon trigger[66] was used to investigate deep-inelastic muon scattering at high Q^2, while the dimuon trigger's[65] primary physics motivation was the virtual photoproduction of promptly decaying charmed mesons. The dominant processes contributing to the trimuon trigger were ψ production and the electromagnetic production of muon pairs (so called muon tridents) by either bremsstrahlung or Bethe-Heitler graphs (Figure II.5).

Each trigger hodoscope consisted of 12 counters S_{1-12} (Figure II.6) mounted on a half inch thick aluminum plate. These were bolted flush against the downstream side of the last plate of modules 4, 6, 8, 10, 12, 14, 16, and 18 and centered on the beam. To be identified as a muon, a particle had to be seen in 3 successive hodoscopes, passing through a minimum of 80 inches, or 12 absorption lengths, of steel. Counters S_{4-9} (S_3, S_{10}) are 1.55 (5.98) inch high "slat" counters, responsible for counting muons and acting as a beam veto for the single muon trigger. Each is 41.5-in long. $S_{1,2,11,12}$ are 23.8-in high by 20.75-in wide "paddle" counters; hits in these counters are required for the single muon trigger. Note that the use of horizontal slat counters in the beam region limits the study of multimuon states to those where the produced muons separate enough in

the vertical direction. Events where the incident muon scatters, or the ψ decays, in the horizontal plane are not detected, thus substantially reducing acceptance from the full 4π. While the fact that the magnet bends muons in the horizontal plane makes vertical scattering a necessity for the single muon trigger, it is not a fundamental constraint on multimuon triggering schemes.

The efficiency of each individual counter was measured in the off-line analysis. The slat counters were found to be $> 99\%$ efficient. The paddles were seen to have an efficiency ϵ which varied linearly with distance d from the phototube. This was parameterized as

$$\epsilon = 0.88 + (36 - d(\text{inches}))0.0033$$

for each counter and used in the Monte Carlo simulation of the apparatus.

The simplest trimuon trigger for the apparatus would have merely required that 3 separate counters fire in 3 hodoscopes. Unfortunately, the copious production of low mass electromagnetic tridents forced us to implement an additional opening angle criterion. Basically, we require that by the time the 3 muons reach the second (and third) of three consecutive banks of counters participating in a trigger, they separate enough so that at least one fired counter is not adjacent to the other two. If a paddle counter is involved in a trigger or if more than 3 counters have fired, the non-adjancency requirement is dropped for that hodoscope. Figure II.7 shows the formation of the trigger in detail for one bank, numbered i, $i = 1$–8, and the definition of ψ^i_{adj} and ψ^i_{nadj}. The trigger fires when one or more of the 6 possible subtriggers, $\psi^i_{adj} \bullet \psi^{i+1}_{nadj} \bullet \psi^{i+2}_{nadj}$, is satisfied. Figure II.8 shows the spectrum of muon pair masses for the experiment under slightly more general cuts[67] than those used in the present analysis. The combination of finite width counters and the above trigger algorithm successfully turns over the rapidly climbing distribution as $m_{\mu^+\mu^-}$ goes to zero.

The total data aquisition rate for the trimuon trigger was 15×10^{-6} per incident muon. However, only a part of this was due to physically interesting processes. Random coincidences between multiply-hit hodoscopes were responsible for approximately a third of the data taken. Muons are continuously losing energy in the spectrometer. Both knock-on electons (delta rays) from the last

bit of steel before a hodoscope and small electromagnetic showers along a track can cause multiple counts in hodoscopes. These are uncorrelated from module to module but occur with sufficient probability to substantially contribute to the trigger rate. Shower punch-thru from single or dimuon events also contribute to the spurious background at a lower level.

II.5 The PC-DC System

Muon tracking in the spectrometer was accomplished with a system of 19 PC-DC pairs. These chambers were mounted behind each of the 18 magnet modules and plate 0. The (x, y, z) origin of the spectrometer coordinate system was located at the upstreammost PC. Both the PC's and DC's were designed to be as thin as possible, thereby minimizing the inter-module gap and overall spectrometer length while maximizing the spectrometer's average density. Each PC measured coordinates in the x, y, and u directions. Proportional chamber wire spacing in the x, or magnet bend plane, direction was chosen so that momentum resolution for average length tracks would be comparable to that caused by multiple coulomb scattering (MCS) in the steel plates. The DC system provided improved x spatial resolution so that the same MCS momentum limitation could be maintained for shorter (4 chamber) tracks. Each chamber was fully active over its entire area, including that occupied by the beam. As mentioned previously, this simplifies analysis of low Q^2 events. The PC signals were used to resolve the two-fold ambiguity inherent in the DC readout.

II.5.1. PC Construction

Each proportional chamber (PC) consisted of an anode plane of vertical wires, measuring the x coordinate, bracketed by two wire cathode planes. These were strung at 90 degrees and 60 degrees with respect to the vertical wires, measuring the y and u coordinates, respectively. The u coordinate was used for determining which x and y points should be paired together and provided an additional position measurement in case of non-unit efficiency on the other planes.

The anode, or sense, plane was composed of 336 gold plated tungsten wires 20 μm in diameter spaced every 0.125- in. Each wire was dc coupled to a comparator circuit, whose amplified signals were delayed via 200–400 ft of Ansley ribbon cable and latched for events satisfying a trigger. The cathode planes were constructed of 3 mil diameter Be-Cu wire spaced every 0.050 inches. Consecutive groups of 4 wires were ganged together and ac coupled to the input of a centerfinding - amplifier circuit. The Lorentzian shaped charge distribution induced on the cathode plane of a PC causes each wire to have the same sign voltage pulse - a problem not found on the sense plane. Rather than simply using a voltage comparator with a set threshold level, thus playing detection efficiency against pulse pair resolution, the design chosen (Figure II.9) essentially takes the second derivative of the charge distribution to convert signal polarity in the central region of the pulse to the opposite of that found on the remaining wires. In this scheme there is one output channel driving a comparator-delay line-latch circuit for every two input channels. The plane measuring the y coordinate had 176 such output channels, while the u coordinate plane used 192 channels.

The chambers were constructed out of Nema-G10 layers, bolted on 47.5 in wide by 96 in high by $\frac{1}{2}$ in thick aluminum jig plates and covered on the outside with 1/16 in aluminum sheets. The jig plate and mylar sheet formed a gas barrier; both were kept at ground potential. The jig plate was equipped with two vertically oriented 72 in $\times$ 2.5 in $\times$ 1 in thick aluminum support ribs and two horizontically oriented 46 in $\times$ 3 in $\times$ 1.5 in aluminum support ribs for flattening the chamber after wire tensions pulled it out of shape. The inner (outer) chamber dimensions were 41.5 in $\times$ 71.2 in (47.5 in $\times$ 83.2 in). There were two symmetrically positioned dowel pins on the 3 in wide vertical frame members and one on each 6 in wide horizontal member to locate the chamber. The sense - HV plane separation was 0.400-in, while the HV plane - jig plate, gas window separation was 0.555-in. The difference in these numbers comes from the fact that the wire sense plane cannot be treated exactly as a continuous ground plane for the purpose of balancing bulk forces on the HV planes. Instead, if s is the sense plane wire spacing, d the sense wire diameter, and L the sense-HV plane separation, the HV plane-true ground plane gap L' required for electrostatic equilibruim on the HV

plane is

$$L' = L - \frac{s}{\pi} \ln \frac{\pi d}{s}.$$

The sense-HV plane spacing L was set to optimize y and u plane spatial resolution, once the basic channel spacing (0.400-in) was fixed (by cost considerations). Since L affects the width of the induced charge distribution, it can be tuned so that the probability of firing either one or two output electronics channels is equal. Then the intrinsic resolution parameter of the plane corresponds not to the output channel width of 0.400-in, but rather to the input channel width of 0.200-in. The sense (HV) wires were strung at a tension of 60 g (150 g), approximately 2/3 of their elastic limit. Four double-sets of nylon wires interwoven across those of the sense plane provided protection against wire to wire electrostatic instabilities. Each plane used several larger diameter (5 mil) wires near the frames to avoid regions of abnormally high field. The gas used was "magic gas II", a blend of 60% argon, 35% isobutane, 4.7% methylal, and 0.3% freon, by number of molecules. Average operating voltages were between 5.0 and 5.7 kV. The readout system was gated on for a period of 70 nsec when a trigger was satisfied.

Besides minimizing cost and overall thickness, getting information on y and u coordinates from the cathode plane wires of a chamber whose anode wires measure x, rather than from other separate anode plane chambers, simplified track finding by eliminating the need for knowing the track slope before matching x, y, and u coordinates together. For the cathode readout chamber all measurements are automatically referenced to the z position of a single electron avalanche, independent of track direction.

Chamber resolution on the sense plane was equal to 900 μm, approximately $1/\sqrt{12}$ of the wire spacing. Cathode plane resolution reflected the 0.200-in semi-channel spacing of the electronics, as described above, so that $\sigma(y \text{ or } u) \simeq 1500 \mu m$. Chamber efficiency was measured in the off-line analysis by finding tracks and examing whether or not a particular chamber contributed. It was found that efficiency varied with track position in a form parameterized by

$$\epsilon_{ij}(x,y) = a_{ij} - b_{ij}e^{-r_j/r_{ij}},$$

where r_j is the radial distance of the point (x,y) from the beam centroid in chamber number j, and $i = x$ or y. Thus a_{ij} is the maximum chamber efficiency far from the beam and $(a_{ij} - b_{ij})$ is the chamber efficiency in the beam; r_{ij} determines how fast the transition occurs. These parameters were measured for μ^+ and μ^- running separately, as lower beam intensity improved efficiency somewhat, and included in the MC simulation of the spectrometer. The average values (over chamber number) and root mean square (rms) deviations of a_i, b_i, r_i for μ^+ and μ^- data are shown in Table II.1. Poor induced plane efficiency in the beam area increased the difficulty of the track finding substantially. This minimum efficiency systematically improves with distance from plate 0, since the beam is spreading as it scatters in the magnet steel.

II.5.2. The Drift Chamber System

Each DC consisted of one plane of 0.75-in wide cells, active over a 42-in wide by 72.5-in high area. The drift cell geometry and other construction details can be found in Reference 65.

The DC readout system involved the use of seven 8 input channel time-to-digital converters (TDC) per chamber and a 120 MHz clock. Each TDC could latch up to 4 signals arriving within 31 time bins of the trigger logic start pulse. By distributing each DC wire in a group of 7 consecutive wires to a different TDC it was possible to avoid overloading any given digitizer with beam related hits. The readout system is described more thoroughly in Reference 68.

The DC system was found to have a resolution of better than 250–μm and an efficiency in the beam greater than 98%. Multiple DC hits occurring in the 300 nsec trigger gate were sorted using information from the PC system.

II.6 Data Acquisition

The data acquisition system consisted of a PDP-15 computer reading trigger-latched information

from the hardware via a CAMAC interface. The total trigger rate was approximately 25×10^{-6} per incident muon; typically 50 events were recorded on magnetic tape each spill. Total dead-time from all causes (including all beam vetoes) was 50%. Readout related deadtime was only 10%. A major part of this 10% was due to electronic noise problems in the CAMAC interface which prevented us from using its double-buffer capability.

III. ANALYSIS

From January to June 1978 a total of approximately 4×10^{11} muons were incident on the MMS. The data reported here correspond to a sample of $0.6\times10^{11}\mu^-$ and $1.8\times10^{11}\mu^+$, 80% of the useable total. The remaining events are sufficiently flawed by equipment abnormalities to make analysis uncertain. For 60% (40%) of these events the MMS magnetic field was in the $+y$ ($-y$) direction. While the incident beam energy was 214 GeV, the average energy of an interacting muon was 209 GeV, due to dE/dx losses in the spectrometer.

Approximately 1100 data tapes, containing 1.2×10^6 triggered events, were written. These were divided into 14 basic analysis units, each consisting of runs taken at roughly the same time, having the same beam muon sign and MMS magnet polarity. Beam and calorimeter calibration constants, wire chamber alignment constants, and apparatus acceptance were determined separately for each group. The average values of the main kinematic variables and the ψ yield per incident muon were evaluated separately for each group and found to be consistent. Of the 7.2×10^5 trimuon triggers, 1.0×10^5 satisfied the analysis criteria (Sec. III.1) for true trimuon events. After choosing one of the beam sign final state muons as the spectator (Sec. III.3.4) one can plot the mass distribution of the remaining opposite signed pair (Figure II.8). This plot reveals a clear peak at the ψ mass containing 6700 events. Setting cuts that insure an accurate measurement of the apparatus acceptance reduces this sample to 4375 events.

These events are classified as either elastic (2625 events) or inelastic (1750 events) based on the amount of energy E_{cal} that is seen in the calorimeter in a region surrounding the interaction vertex. Figure III.1 shows the distribution of E_{cal} and the cut at 4.5 GeV which defines the two samples. Apparatus acceptance was calculated for each sample by separate, though similar, Monte Carlo (MC) simulations; results for each will be presented separately. The reason for this apparently

arbitrary division of events is historical: at the time results were first being prepared the only production models available were those of VMD and γGF, both of which pertained only to elastic events. Quantitative comparisons required a sample consistent with $E_{cal} = 0$, which, given the calorimeter resolution, the 4.5 GeV cut satisfied. The later publication of inelastic ψ production models seemed consistent with the concept of maintaining separate samples defined by the same cut. Using the final MC simulations (Sec.III.4.2 and III.4.3) the (appropriately normalized) integral distributions $\int_{-\infty}^{E_{cut}} P_{inelastic}(E_{cal})dE_{cal}$ and $\int_{E_{cut}}^{\infty} P_{elastic}(E_{cal})dE_{cal}$ were examined as a function of E_{cut}. As seen in Figure III.2, defining E_{cut}=4.5 GeV minimized the need for a resolution induced smearing correction between the samples.

Two problems are created by this method, due basically to the fact that the apparatus remains a device best suited for inclusive ψ production rather than one capable of studying the final state in detail. The first is artificial—the relative normalization of the samples. This is discussed in Sec.IV.1 and does not affect the total ψ production cross section. Second, and more important, is the difficulty of identifying events near E_{cut} as "truly elastic" or "truly inelastic". Its greatest effect is on the elasticity (z) distribution of the inelastic sample (discussed in Sec.V.1), where it creates a systematic error for points above $z > 0.7$, as the concept of an "inelastic event" at $z \sim 1.0$ is something of an experimental contradiction in terms. Operationally, these difficulties could have been solved by modeling the entire ψ sample with a single simulation, whose results could then have been cut to meet whatever theoretical constraints were needed. Not using this method is probably the single largest shortcoming in the analysis.

Below we describe those steps that must be taken to convert the raw information on the primary data tapes to acceptance-unfolded differential cross sections. Major topics include track finding, momentum fitting, and the acceptance measurement. Included under these headings at the appropriate point are discussions of the definitions, calculations, calibrations, and cuts used. A discussion of the effects that might contribute to a systematic error in the results concludes the section.

III.1 Reconstruction

III.1.1 Track Finding

Candidate track segments were formed at the downstream end of the spectrometer and projected to upstream chambers. Additional points inside a carefully defined search window were then added to the track and used to adjust further projections. Actual track formation was done only with MWPC information; DC coordinates were added to each track after reconstruction was complete. The finding process coupled x and y spectrometer views by placing greater importance on x–y pairs of points which had confirming hits on the u plane (x–y–u matches or "triplets") than on otherwise independent x and y points. Successive projections of the scattered tracks proceeded up to the MWPC downstream of the calorimeter supplied z vertex position. As triplet points were added to tracks, they were deleted from the available pool of points; the track finding process ended when the pool of points was sufficiently exhausted. Accepted tracks were required to have at least 4 x-points, two of which were triplets. A detailed description of the method can be found in Reference 65.

III.1.2 Vertex Finding with the Calorimeter

Two methods were used in finding the vertex position z_v of an event satisfying the trimuon trigger. When $E_{cal} < 36$ GeV a maximum likelihood approach was used to find the small step in pulse height expected from a change in the energy lost by one and three minimum ionizing particles. For events with $E_{cal} > 36$ GeV a search was made for the counter with the maximum pulse height.

Approximately 90% of the events employed the maximum likelihood method, which requires as input the parent pulse height distributions for one and three minimum ionizing particles. For the one muon case these were measured for each of the 75 counters j using beam sample events. After the mode was normalized to one "equivalent particle" (e.p.), fits to each distribution were made to find $P^1_j(n)$, the probability of observing n e.p. in counter j from the passage of 1 muon. Typically,

$$P^1(n) = 8.14(e^{-0.93n} - e^{-1.05n}).$$

The average three muon pulse height distribution was found using calorimeter information in a sample of handpicked trimuon events. $P^3(n)$ was fit to a gaussian whose mean was 4.17 e.p. and standard deviation was 1.54 e.p. The vertex was found by evaluating $\mathcal{L}_k$, the logarithm of the liklihood function for a vertex in the steel plate before counter K, $1 \leq K \leq 75$,

$$\mathcal{L}_k = \prod_{i=1}^{k} \frac{P_i^1(n_i)}{P_i^3(n_i)} \prod_{i=k+1}^{75} \frac{P_i^3(n_i)}{P_i^1(n_i)},$$

and finding the maximum. The method worked well for clean events, but could be fooled by small electromagnetic showers hitting a number of consecutive counters and creating a second peak in $\mathcal{L}_k$. The statistical error assigned to z_v was typically 1 plate spacing divided by $\sqrt{12}$, or 3.7 cm. When track information implied an incompatable result for z_v, the calorimeter vertex was dropped from the fit.

When the calorimeter signal is large, vertex finding is easier. Basically, the counter having the largest pulse height is found and a decision made on whether or not to move z_v slightly upstream to account for shower development. If A is the maximum pulse height, for each counter k, the algorithm calculates N_k, the difference in the number of upstream counters with pulse height less than and greater than $0.08A$. The middle of the plate having the maximum value of N_k is chosen as z_v.

III.2 Momentum Fitting

For each track candidate in every event the track finding program supplied an array containing the best x and/or y PC coordinates found (if any) and the two best DC coordinates attached (if any). It was the responsibility of the next program to determine which tracks were consistent with a common vertex, the position of the vertex, which track candidates were actually parts of the same track – broken by a large angle scatter, which points supplied for a given track truly belonged on it, and finally, the 4-momentum of each track at the vertex. It used an iterative solution to these

problems based primarily on rejecting information which would cause an unacceptable χ^2 in the momentum fit. In addition to finding each muon's vertex momentum, this fit solved for the multiple coulomb scattering angles in each magnet module and considered the effects of energy loss. The general iterative procedure is described in Reference 67.

III.3 Analysis

III.3.1 Calculation of E_{cal}

Once the final vertex position is known, the calorimeter counter pulse heights around v_z can be used to find E_{cal}. Basically, we sum the number of equivalent particles (e.p.) in the 5 counters upstream and 10 counters downstream of v_z, correct for the mean number of e.p. expected from the muons themselves, and convert the result to GeV using an inelastic muon scattering determined calibration. The sum over 15 counters is truncated if we run out of calorimeter, or extended, either upstream or downstream, if there is evidence of more signal than that expected from the observed number of minimum ionizing muons. While we typically consider E_{cal} as a measure of the hadronic energy seen in an event, having corrected for the mean energy less due to electromagnetic processes (i.e. the measured 1 and 3 particle probability distributions discussed in Section III.1.2), it is nonetheless an all inclusive measurement that might contain an electromagnetic component. This may arise from interesting physical processes, such as $\mu N \rightarrow \mu\chi$ with $\chi \rightarrow \psi\gamma$, or from large fluctuations in dE/dx losses from the mean.

III.3.2 Calorimeter Calibration

The amount of energy lost by muons in deep-inelastic scattering events, as measured magnetically by the spectrometer, was used to calibrate the calorimeter. Typically we found that 1 GeV corresponded to 6 e.p. The calorimeter's zero level was fine tuned by using samples of ψ events with $E_{cal} < 36$ GeV and demanding that the average beam energy equal the average energy seen

in both the spectrometer and calorimeter. The resulting rms resolution of the calorimeter $\sigma(E)$ was measured as $1.5\sqrt{E(\text{ GeV})}$, with a minimum value for σ of 2.5 GeV.

III.3.3 Constraining Events Kinematics with the Calorimeter

While true in an average sense, the requirement of visible energy conservation in ψ events is not automatically satisfied on an event-by-event basis due to the effects of resolution or improper analysis. When the missing energy $E_{miss} \equiv E_b - (E' + E_d^+ + E_d^- + E_{cal})$ is histogrammed, the resulting gaussian distribution has a rms standard deviation of 16 GeV. Only events statistically consistent with $E_{miss} = 0$ ($\sigma(E_{miss}) < E_{miss}/2.2$) were kept in the analysis. This cut is approximately equivalent to the requirement -34 GeV $< E_{miss} <$ 28 GeV. Events satisfying the cut then had the momentum components of the 4 muons and E_{cal} statistically adjusted so that $E_{miss} = 0$. This constraint can only be used if all energies involved are independently measured. Its major benefit is an improvement in resolution, especially at low values of ν. Figure III.3(a) shows the quantity $\sigma(\nu)/\nu$ versus ν before and after the constraint equation is applied. Figure III.3(b) shows the resolution in Q^2, $\sigma(Q^2)/Q^2$, vs. Q^2. Only one curve is presented in this case as no substantial change is induced by the E_{miss} constraint.

III.3.4 Spectator Algorithm

To calculate kinematic quantities for ψ events one of the two beam-sign muons in the final state must be chosen as the spectator. If one of the muons has an energy which is more than two times that of the other it is chosen, while if this condition is not met, the muon which minimizes the lab scattering angle θ_V is picked. Monte Carlo studies show that this algorithm is successful 91% of the time. It was designed so that when it did make a mistake, the resulting pair mass $m_{\mu^+\mu^-}$ would tend to fall below, rather than above, m_ψ, where the large electromagnetic trident background can ameliorate its effect.

III.3.5 Background Subtraction; The Dimuon Mass Distribution

As previously mentioned, the dominant trimuon background to $\mu N \to \mu\psi X$, $\psi \to \mu^+\mu^-$ is the

coherent electromagnetic production of muon pairs through the Bethe-Hiether or bremsstrahlung graphs (Figure II.5). These events, and any others due to less important processes (e.g. the virtual photoproduction of D meson pairs, with both D's decaying to muons), are removed from the ψ sample by making a smooth extrapolation of the continuum under the ψ peak in the $m_{\mu^+\mu^-}$ mass distribution. Since such a background subtraction is done for each bin in a kinematic variable for which a data point is presented, no assumptions as to how the background varies with any variable need be made. The statistical error presented for any result includes the estimated error in the subtraction.

Figures III.4(a) and (b) present the muon pair mass distribution above 1.12 GeV/c^2 for the final sample of trimuon events having E_{cal} less than and greater than 4.5 GeV, respectively. Since the mass resolution $\sigma(m_{\mu^+\mu^-}) \sim k m_{\mu^+\mu^-}$, the chosen abscissa coordinate u is logarithmic. Then the bins of equal width each correspond to a constant fraction ($\sim$ 2/3) of the mass resolution, independent of mass. Specifically, $u \equiv \ln(m_{\mu^+\mu^-}/3.1)$ and $\Delta u = 0.06$. The curves shown are fits to the data of the form

$$\frac{dN}{du} = g(u)\exp(f(u)) + N_\psi S(u),$$

where $S(u)$ is a unit-normalized sum of gaussian functions, N_ψ is the sought after number of ψ events, and f and g are quadratic polynomials in u.

The fitting procedure attempted to solve the the intrinsically non-linear problem in three linear steps. First, $\exp(f(u))$ was found by fitting the continuum outside the ψ region. Then, for a given value of N_ψ, the best quadratic polynomial fit $g(u)$ to $(dN/du - N_\psi S(u))/\exp(f(u))$ was found. The function $\exp(f(u))$ thus removed the rapid variation of the data, which typically dropped by more than 3 orders of magnitude over the mass range of interest. The best value of N_ψ was found by using it to minimize the χ^2 of the $g(u)$ fit. The error on N_ψ was calculated by finding those points for which χ^2 increased by one unit.

The parameters describing $S(u)$ were fixed separately for elastic and inelastic events by optimizing them using the total dimuon mass distributions of Figure III.4. Once determined, they

were not allowed to vary for any other fit. To describe the inelastic ψ peak required two gaussians, each centered at 3.07 GeV/c^2, with rms widths of 0.086 and 0.145 and relative areas of 0.63 and 0.37, respectively. The resulting value of N_ψ is 1747 ± 57 events, with $\chi^2 = 14.8$ for 22 degrees of freedom (df). In fitting the elastic ψ peak two gaussians were also required. These were centered at 3.12 GeV/c^2, and had rms widths of 0.080 and 0.127 and relative areas of 0.75 and 0.25. The elastic fit also assumed an additional 4.5% contribution to the signal from $\psi' \to \mu^+\mu^-$ events, as expected from VMD arguments (See III.5.3). The small shoulder above the ψ peak in Fig. III. 4(a) indicates the effect of such a contribution.

The additional gaussian function of larger width in $S(u)$ is a first attempt at describing the high mass tail of the $m_{\mu^+\mu^-}$ distribution. There may be reconstructed ψ masses at still higher values that would require additional terms to be fit. For simplicity, a third gaussian was not added to $S(u)$, but instead, an overall correction to the fit N_ψ was calculated and applied in all cases where absolute normalization of a result was required. The correction is determined by graphically fitting the background by hand, ignoring the region 2.3 GeV/c^2 $< m_{\mu^+\mu^-} <$ 4.5 GeV/c^2, and comparing the result with the fit value. We find that no correction is needed for the inelastic results, but that the elastic value of N_ψ must be raised by a factor of 1.05. The total number of elastic ψ and ψ' events above background is then 2627 ± 66, where the χ^2 of the fit was 21.5 for 23 df.

Finally, as a one-parameter description of the mass resolution, we use the full width at half maximum (FWHM) of the ψ peak divided by 2.36. For elastic events $\sigma(m_{\mu^+\mu^-}) = 0.086 m_{\mu^+\mu^-}$, while for inelastic events $\sigma/m = 0.096$.

III.4 Acceptance Calculation

A Monte Carlo (MC) simulation of ψ production in the spectrometer was used to unfold apparatus acceptance and resolution effects from the measured distributions of the data. Events were generated, the muons propagated through the apparatus, and simulated raw information written on

tape. These events were then analyzed with the same programs used on the data. The resulting distributions of measured variables were compared to those of the data to produce the final results.

The MC is composed of two parts: a physics generator and an apparatus simulation. The apparatus section, described below, models the beam, the various elements of the spectrometer, and the interactions of muons with matter. The use of an accurate model in the physics generator of a simulation is important when much of the cross section measurement to be reported lies in an area of low apparatus sensitivity, when poor resolution affects the measurement of rapidly changing distributions, when one desires to factor known physics from the results, or when the acceptance is a function of several inter-correlated variable. For the purposes of this analysis the third and fourth points are most pertinent, although the first does apply somewhat to our total cross section measurement. The "known" physics to be factored out in this case consists of the transverse flux of virtual photons $\Gamma_T(Q^2, \nu)$ and nuclear physics effects (coherent scattering, shadowing, Fermi motion). Differential results will be presented that are directly comparable with those from experiments using real photons and hydrogen targets. The fourth point refers to the fact that, while the simulation's dependence on any given variable is factored out by the procedure used to extract final results in that variable, there is an intrinsic assumption that the data's dependence on any other variable that is correlated to the one in question, either by the apparatus or by the physics, is correctly modeled.

Both elastic and inelastic MC simulations used VMD inspired phenomenological distributions to describe the Q^2, ν, (t or $p_\perp^2$), θ, ϕ, and z distributions of the generator. An iterative procedure was used to adjust the parameters in these distributions until the ratio of data to MC events was flat as a function of each variable. Convergence was achieved by the third iteration. The final set of generating functions can be viewed as the best phenomenological fits to the differential results presented in Sections IV and V.

III.4.1 The Apparatus Simulation

The MC program used as input the sample of beam trigger events accumulated during each data run. These muons were propagated through the spectrometer and interacted randomly in the

target material of the first 14 modules of the apparatus. The three muons arising from successfully generated ψ events were then also propagated until they either left or ranged out in the spectrometer. Raw information from the beam system was transferred intact to the MC and information from detectors in the spectrometer simulated for each of the four muons. Hit wires in each MWPC and DC and hit trigger counters in each hodoscope were registered according to the efficiencies discussed in Section II.5. The calorimeter was simulated in two ways: counter-by-counter and as a whole. Individual counter pulse heights were determined by converting total event shower energy (if any) in GeV to a number of e.p., spatially distributed as seen in pion-induced hadronic showers in similar calorimeters[69], and incrementing this by the number of final state muons passing through the counter. This information was used exclusively for calorimeter z vertex finding and for simulating the calorimeter part of the dimuon trigger. In order to get a measured value of E_{cal} for use in constraining event kinematics, the total generated shower energy was simply smeared by the resolution function discussed earlier. When events passed any one of the three triggers, the raw information was written on tape in the same format used by the data, along with the values of the generated variables that would later be used for understanding resolution and unfolding the final results.

Muons are propagated plate by plate using the measured magnetic field map, and taking into account the effects of MCS and electromagnetic energy loss mechanisms. The field map is tabulated on a 1 inch grid for one quadrant of the magnet. The same map, up to a normalization factor,is used for each module in the spectrometer. The net transverse momentum components p_x and p_y caused by the many independent small-angle Coulomb scatters are drawn from gaussian probability distributions whose standard deviations are given by $15\sqrt{L_R}$ MeV/c, where L_R is the number of radiation lengths of material traversed. A $p_\perp$ tail due to single large angle Coulomb scatters is generated according to the Rutherford formula[70] modified by the nuclear form factor for iron. Energy loss mechanisms considered include μ–e scattering, direct electron pair production, and muon bremsstrahlung.

III.4.2 Elastic Event Generator

Three separate physics generators were used to model elastic ψ muoproduction, corresponding to the processes: $\mu N \to \mu N \psi$ with $\psi \to \mu^+\mu^-$, $\mu N \to \mu N \psi'$ with $\psi' \to \mu^+\mu^-$, and $\mu N \to \mu N \psi'$ with $\psi' \to \psi\pi\pi, \psi\eta$ and $\psi \to \mu^+\mu^-$. The ψ' models are simple VMD extensions of the primary ψ generator. They contribute relatively few events to the MC sample and are included mostly for the sake of completeness. Each generator assumes that $\sigma(\mu N) = \Gamma_T \sigma(\gamma_V N)$, as described in Section I.1.1, and handles the nuclear effects of coherence, shadowing, and Fermi motion in the same way. Once an event is generated on the basis of Q^2 and ν, values of z, t, θ, and ϕ are chosen according to the distributions listed below. As mentioned previously, because of the iterative extraction procedure, the forms of the generating functions used in the final version of the MC are the best phenomenological fits to the results themselves. Here we compile those results from Sections IV and V without explanation and refer the reader to them for more detail.

The amount of coherent *vs.* incoherent scattering is fixed by the optical model inspired expression,

$$d\sigma/dt = d\sigma/dt\,|_{t=0}\,[A_{eff}^2 e^{b_c t} + A_{eff}(f e^{b_1 t} + (1-f)e^{b_2 t})],$$

where the values of b_c, b_1, b_2, and f are those of Fit 3 in Table IV.1. For the purposes of generating the MC we assume $A_{eff} = 0.85A$, independent of Q^2. This question of shadowing is dealt with more fully in Sec.III.6.2 and in those sections which describe results that can be affected by it. Fermi motion refers to the fact that, for incoherent events, the nucleon targets are not at rest in the laboratory. We assume that their kinetic energy T distribution is given by

$$\begin{aligned} dN/dT &\propto \frac{\sqrt{T}}{1+\exp((T-36)/6.4)} && \text{for} \quad T < 70 \text{ MeV}, \\ &\propto T^{-2.6} && \text{for} \quad T > 70 \text{ MeV}. \end{aligned}$$

A transformation to the target rest frame is made, assuming $m_n = 0.9045$ GeV/c^2 (empirically determined for this particular Fermi motion parameterization so that the atomic weight of iron is conserved), and the incident muon momentum boosted accordingly.

The integral of $d\sigma/dt$ from t_{min} to t_{max} gives the cross section for producing events as a function of Q^2 and ν. We have,

$$\sigma(\gamma_V N \to \psi N) \propto P(Q^2)S(\nu)T(t_{min}(Q^2,\nu)),$$

where,

$$\begin{aligned} P(Q^2) &= (1+Q^2/\Lambda^2)^{-2}, && \text{with} \quad \Lambda = 2.18 \text{ GeV}, \\ S(\nu) &= \log_{10}\nu/\nu_{th}, && \text{with} \quad \nu_{th} = 11.2 \text{ GeV}, \end{aligned}$$

and

$$\begin{aligned} T(t_{min}) &= e^{bct_{min}} && \text{for coherent events} \\ &= (f/b_1 e^{b_1 t_{min}} + (1-f)/b_2 e^{b_2 t_{min}})/(f/b_1 + (1-f)/b_2) && \text{for incoherent events.} \end{aligned}$$

The angular distribution $W(\theta,\phi)$ of the ψ daughter muons is assumed to be

$$W(\eta,R;\theta,\phi) = \frac{3}{16\pi}\frac{1}{1+\epsilon R}[(1+\cos^2\theta) + 2\epsilon R\sin^2\theta - \eta\epsilon\sin^2\theta\cos 2\phi],$$

with $\eta = 1.0$ and $R = \sigma_L/\sigma_T = 4Q^2/m_\psi^2$.

For the ψ' generators it is assumed that

$$\frac{\sigma(\mu N \to \mu N\psi')}{\sigma(\mu N \to \mu N\psi)} = \frac{\Gamma(\psi' \to \mu^+\mu^-)/m_{\psi'}}{\Gamma(\psi \to \mu^+\mu^-)/m_\psi} = 0.38,$$

in accord with VMD expectations of the virtual photon–vector meson coupling strength. The threshold ν_{th} is scaled up by the factor $(m_{\psi'}^2 + 2m_n m_{\psi'})/(m_\psi^2 + 2m_n m_\psi)$. The $\psi' \to \psi X$ angular distribution is asumed to be s–wave, and the dipion mass distribution given by equation 6 of Reference 71. The branching ratios of ψ' to $\mu^+\mu^-$, $\psi\pi^+\pi^-$, $\psi\pi^0\pi^0$, and $\psi\eta$ used are 0.009, 0.33, 0.17, and 0.042, respectively.

In parts (a)–(f) of Figure III.5 are plots of the MC measured apparatus acceptance (i.e. before analysis) as a function of Q^2, the minimum ψ daughter energy $(E_d)_{min}$, $p_\perp^2$, $\cos\theta$ (the polar decay angle of the μ^+ daughter in the ψ rest frame), the azimuthal angle ϕ, and the elasticity $z \equiv E_\psi/\nu$,

respectively. The Q^2 plot illustrates the advantages of maintaining an active region in the beam area of the spectrometer. The gradual increase of efficiency ϵ with Q^2 is due to the increased separation of the muons as the scattering angle increases. The $(E_d)_{min}$ plot shows how the sensitivity of the apparatus drops at low muon energy, due to muons stopping in the spectrometer steel. Fear of modeling this dependence over too large a range causes a cut to be applied (Sec.III.5) at 10 GeV. The drop off of ϵ with decreasing z has the same cause as that at low $(E_d)_{min}$. The $\cos\theta$ plot indicates how asymmetric muon energies limit acceptance at high values of $|\cos\theta|$. As will be discussed in Sec.IV.3, since the function $1+\cos^2\theta$ is approximately flat over most of its accessible range, this lack of sensitivity limits our measurement of $W(\theta,\phi)$ and through W, of σ_L/σ_T. The acceptance in $p_\perp^2$ is approximately flat. The ϕ plot implies that the apparatus is maximally efficient for events where all three muons are not coplanar. One should note that while the observed shape of this distribution is similar to that reported as an acceptance-unfolded result in Sec.IV.3, its variation is 3.75 times smaller than that required to account for the observed signal.

The average efficiency for detecting and analyzing an elastic ψ event is given by

$$\epsilon = \frac{\text{\# MC events analyzed, passing all cuts}}{\text{\# generated psi events}}.$$

We find that $\epsilon = 0.186$. Note that this assumes a 3.4% contribution to the cross section from the $\psi' \to \mu^+\mu^-$ channel and corrects for it.

III.4.3 Inelastic Event Generator

At least two different types of physics can contribute to the 1747 ± 57 event inelastic sample (Figure III.4(b)). One of these is true inelastic ψ production, such as that embodied by calculations in which hard final state gluons provide hadronic energy to the calorimeter. If bound $c\bar{c}$ pairs with masses greater than m_ψ are being produced (as expected in the γGF model), they may decay to the $\psi(3097)$ with the emitted hadrons contributing sufficient energy to the calorimeter to label the event as inelastic. These events are fundamentally elastic in nature. They include, for example, production of ψ' and χ states where $\psi' \to \psi\pi\pi$ and $\chi \to \psi\gamma$. It is possible to isolate a sample of

truly inelastic events by further cutting the data in elasticity $z \equiv E_\psi/E_\gamma$. Because of the limited mass difference of $m_{\psi'} - m_\psi$ and the peaked nature of the dipion mass distribution in $\psi' \to \psi\pi\pi$ we expect events from that source to satisfy

$$\frac{E_\psi}{E_\gamma} = 1 - \frac{E_{had}}{\nu} \simeq 1 - \frac{\gamma m_{\pi\pi}}{\nu} \approx 1 - \frac{m_{\pi\pi}}{m_{\psi'}} \simeq 0.8,$$

where γ is the Lorentz boost used to go from the ψ' rest frame to the laboratory frame. The smaller mass difference in χ decays will cause these events to be even closer to the elastic edge, $z = 1$, of the data. Calorimeter resolution and the angular distribution of the emitted ψ's will smear the resulting elasticity about this central value. Tabulated in Table V.1 and plotted in Figure V.1 (as filled triangles) is the result of the MC simulation of the $\psi' \to \psi\pi\pi, \psi\eta$ process described in the previous section. By considering separately the data satisfying $z < 0.7$ we can be assured of including very few of these events in the sample.

The generator assumes that all inelastic scattering is incoherent. As in the elastic case, only Q^2 and ν control the probability of an event being generated; every successful event has a value of z, $p_\perp^2$, θ, and ϕ chosen for it. It is assumed that

$$d^2\sigma/dzdp_\perp^2 = f(z)T(p_\perp^2),$$

$$\sigma_\gamma(\gamma_V N \to \psi N) = \int\left(d^2\sigma/dzdp_\perp^2\right)dzdp_\perp^2 = P(Q^2)S(\nu),$$

and that the ψ decay angular distribution is $W(\theta,\phi)$. One functional form of $f(z)$ is chosen, and $T(p_\perp^2)$, $P(Q^2)$, $S(\nu)$, and $W(\theta,\phi)$ each iteratively optimized for both the $z < 0.7$ and $z > 0.7$ regions. We use

$$f(z) = z(1 - \exp(-z^2/0.54)),$$

and

$$\begin{aligned} T(p_\perp^2) &\propto 0.072e^{-1.69p_\perp^2} + 0.28e^{-0.52p_\perp^2}, \\ W(\theta,\phi) &= 1 - 0.25\cos^2\theta, \\ P(Q^2) &= (1 + Q^2/(3.10\ \text{GeV})^2)^{-2}, \\ S(\nu) &= \nu^{0.95}, \end{aligned} \qquad (III.1)$$

for $z < 0.7$, and

$$\begin{aligned} T(p_\perp^2) &\propto 0.86e^{-2.42p_\perp^2} + 0.14e^{-0.45p_\perp^2}, \\ W(\theta,\phi) &= 1 + 0.58\cos^2\theta, \\ P(Q^2) &= (1 + Q^2/(2.61\ \mathrm{GeV})^2)^{-2}, \\ S(\nu) &= \nu^{0.63}, \end{aligned} \tag{III.2}$$

for $z > 0.7$.

We find that the average efficiency for detecting and analyzing an inelastic ψ event is:

$$\langle\epsilon\rangle_{z<0.7} = 0.120 \pm 0.008(stat.) \quad \text{and} \quad \langle\epsilon\rangle_{z>0.7} = 0.185 \pm 0.007(stat.).$$

III.4.4 Extraction of Results

The method used for extracting a result y_i for the ith bin of the measured (i.e., resolution smeared) variable $\tilde{x}_i$ is to calculate

$$y_i = \frac{D_i}{MC_i} G_{MC}(x_i), \tag{III.3}$$

where D_i and MC_i are the number of data and MC events in the bin, and $G_{MC}(x_i)$ is the generating function of variable x used in the simulation, for example $P(Q_i^2)$ or $S(\nu_i)$. Above, x_i refers to the average *true* value of x in bin i of measured $\tilde{x}$, found using the MC generated varibles passed along with each simulated event. This method unfolds both acceptance and resolution, as well as the effect of any function not included in G_{MC} (such as $\Gamma_T(Q^2,\nu)$). When comparing theoretical predictions which are a function of more than one variable to results extracted in this manner, those variables should be set to whatever their average values are for the data being considered.

The method used is optimally designed for extracting the x dependence of the kernel or generating function of the ψ photoproduction process. It should be distinguished from measurements of the general form $(d\sigma(\mu N \to \mu\psi X)/dx)_i$ *vs.* $\tilde{x}_i$, where variables other than x are integrated over and where phase space, the virtual photon flux factor, etc. can influence the result unless their effects are specifically removed later. Operationally, it is difficult to properly account for both resolution

and acceptance in this latter method as it requires knowing how many *generated* MC events lie in a given bin of a measured variable, whereas, in general, only events which *trigger* the apparatus are analyzed. We use it only for calculating the total cross section, where there is no problem with bin edges.

III.5 Analysis Cuts

Two analysis cuts have already been mentioned: we require that the event have two beam-sign and one opposite-sign tracks attached to the vertex and that the visible energy of an event be conserved at the level -34 GeV $< E_{miss} <$ $+28$ GeV. A number of other cuts are applied to both the data and MC events to define a region in which we are positive that the apparatus acceptance is understood and well modeled. We remove badly reconstructed events, and events lying in regions where either the acceptance varies rapidly or the MC has explicitly failed to duplicate the data. Two tools are used to set each cut: the D/MC ratio as a function of each variable and the number of ψ events lost per cut compared to the amount of background removed. The Q^2 and ν dependences of the D/MC ratio for events lost are checked to avoid introducing spurious effects to the analysis. Ultimately the need for any cut can be traced to an inadequacy in the simulation. Known defficiencies include the approximate handling of the calorimeter counter pulse heights (for MC events the calorimeter vertex almost always agrees with the track-reconstructed vertex) and the lack of chamber hits from halo muons, delta rays, and out-of-time beam muons.

The cuts applied fall into four categories, having to do with the beam quality, individual track quality, overall event quality, and acceptance-sensitive variables. The beam must: 1) have a momentum between 204 and 230 GeV/c, and 2) satisfy a 10-cm$\times$6-cm x–y aperture cut at the enclosure 104 magnet. The cuts applied to each track are: 1) that the χ^2/df in the final momentum fit be less than 4.5 and 2.5 in the x and y directions, respectively, 2) that there be a minimum of 6 contributing chambers, 3) that there be a maximum of 6 and 4 missing chambers when the found

track segment is projected upstream to the vertex and downstream until it leaves the spectrometer, respectively, and 4) that the ratio of contributing chambers to total track length (in chambers) be greater than 0.45. The cuts on event quality are: 1) that there be fewer than 8 hits in the chamber downstream of plate 0 (to guard against incident showers), 2) that if the calorimeter vertex v_z is used in determining the final vertex, the difference between the track reconstructed z-vertex position and v_z be greater than —115 cm and less than +85 cm, 3) that the calculated error on $m_{\mu^+\mu^-}$ (using errors supplied by the momentum fit) be between 5.5% and 10.5%, and 4) that the three final state tracks be sufficiently distinct that they occupy more than a minimum volume in their 6-dimensional x-p phase space. Finally, we require that the final reconstructed vertex lie downstream of the center of module 1 ($z = 44.5$ cm) and upstream of module 12 ($z = 977.8$ cm) and that each ψ daughter muon have an energy greater than 10 GeV. These cuts were applied to both elastic and inelastic events.

The average efficiencies $\langle\epsilon\rangle_{elastic}$ and $\langle\epsilon\rangle_{inelastic}$ for detecting and analyzing elastic and inelastic ψ events were found (Sec.III.4.2 and III.4.3) using only MC events with three tracks attached to the vertex, $(E_d)_{min} > 10$ GeV, and 44.5 cm$<z_{vertex}<$977.8 cm. These must be corrected for the different fractions of data and MC events that are lost by applying the other analysis cuts listed above, if they are to be used to produce a cross section measurement. In the elastic case, there are 3170.3 data and 13949 MC events before and 2502.4 data and 11245 MC events after the cuts are applied, implying that the elastic cross sections should be increased by

$$(c_1)_{elastic} = \frac{3170.3}{2502.4} / \frac{13949}{11245} = 1.021.$$

In the inelastic case, we correspondingly have

$$(c_1)_{inelastic} = \frac{2409.5}{1755.4} / \frac{10556}{8706} = 1.132.$$

Finally, we note that while each ϵ was constant over the above quoted z region chosen for the presentation of differential results, the D/MC ratio for elastic events increased by a factor of

$c_2 = 1.075$ in the more restricted region: 355.6-cm(module 4)$< z <$ 800.1-cm(module 9). Since analyzed events from this central part of the spectrometer should be more free of edge effects, we effectively choose this region of z for normalizing the elastic cross section by increasing its value by this factor.

III.6 Systematic Effects

III.6.1 Radiative Corrections

Radiative effects (Figure III.6) are considered only to the extent that they influence the relative normalization of the elastic and inelastic data samples. Since the range of Q^2/m_μ^2 in the ψ production process is small, corrections to the shapes of the differential cross section results presented in Sections IV and V have been ignored.

The normalization correction is due to the mislabeling of elastic events as inelastic when a sufficiently energetic real photon associated with the vertex is emitted and contributes to E_{cal}. Its size is determined by a separate MC simulation which uses the equivalent radiator approximation[72]. Here, the internal bremsstrahlung from the incident and scattered muon lines (Fig. III.6 (a)) is replaced by an external bremsstrahlung from a separate radiator whose length is given by

$$t = \frac{3}{4}\frac{\alpha}{\pi}[\ln(Q^2/m_\mu^2) - 1].$$

For radiation from the ψ daughter muons (Fig. III.6 (b)) we let $Q^2 \rightarrow m^2_{\mu^+\mu^-} = m^2_\psi$. The diagrams of Fig. III.6(c), involving virtual photons, are ignored, as they will not contribute energy to the calorimeter.

The radiation has the spectrum

$$k(y)dy = (1 - y + 3/4y^2)dy/y$$

where $y = E_\gamma/E_\mu$ is the fractional energy loss in the radiator. In this simplified treatment the MC generates events without regard to the effect of the radiation on Q^2 and ν; it merely calculates, after generation is complete, the probability of each muon to emit a photon of fractional energy $1 - y$:

$$\begin{aligned} P(y_{min}, Q^2) &= \frac{\alpha}{\pi}(\ln(Q^2/m_\mu^2) - 1)\int_{y_{min}}^{1} k(y)dy \\ &= \frac{\alpha}{\pi}(\ln(Q^2/m_\mu^2) - 1)[-\ln y_{min} - 5/8 + y_{min} - 3/8y_{min}^2] \end{aligned}$$

where y_{min} was chosen as 10^{-6}. Within the constraints imposed by energy conservation, all muons are handled independently and the total radiated energy loss taken to be the incoherent sum of the energies of the (up to 4) radiated photons. The increase in the net fraction of events with measured E_{cal}>4.5 GeV under these circumstances is 5.9%, implying that we should increase the elastic cross section of a factor of $1.063 \pm 0.008(stat)$.

III.6.2 Nuclear Shadowing

The phenomenon of "shadowing" of nucleons of complex nuclei in photon interactions, presumably arising from the absorption of the hadronic component of the photon, means that A_{eff}, the effective number of nucleons participating in a reaction, will be less than A, the atomic number of the target nucleus. The question of nuclear screening in iron arises from the desire to present results "per nucleon", comparable to equivalent experiments using hydrogen targets, rather than "per nucleus" or "per Fe nucleon". There are three areas where this question directly affects reported results: in absolutely normalized muon or photon cross sections, in the separation of coherent (off the nucleus) from incoherent (off the nucleons) elastic production, and in the measurement of the Q^2 dependence of ψ production through the possible Q^2 dependence of the screening factor. In addition, other variables are affected to the extent that their distributions are different for coherent and incoherent processes; for example ν, through the different $t_{min}(\nu, Q^2)$ suppression of the coherent and incoherent terms.

This experiment does not attempt to measure this effect and relies instead on published results. The experimental situation is clouded by the existence of contradicting evidence[73—77] and, until

recently, by the unavailability of data at photon energies typical of this experiment. The basic conclusion of the low energy photoproduction (< 20 GeV) data is that $A_{eff}/A \simeq 0.6 - 1.0$ and decreases with increasing photon energy and atomic number. The low energy electroproduction results show a significant reduction in shadowing, with less variation in ν and A than the photon results. Recently measurements[78,79] of A_{eff}/A have been made in a 215 GeV muon scattering experiment at Fermilab. Figure III.7 shows the results, together with the low energy data, as a function of the parameter $x' \equiv Q^2/(2m_n\nu + m_n^2)$. This variable is motivated by VDM arguments that predict a decrease in shadowing as the phase difference between the vector meson and photon (due to their different momenta) increases above a nuclear mean free path, and by a desire to simply combine all available data. The $A \approx 200$ data has been fit to the empirical form

$$\left.\frac{A_{eff}}{A}\right|_{A\approx 200} = 1.0 - a\exp(-bx'),$$

with the result $a = 0.33 \pm 0.03$, $b = 28 \pm 12$, $\chi^2 = 11$ for 9 degrees of freedom, and then scaled to $A = 56$ via the expression

$$\frac{A_{eff}}{A} = A^{\epsilon}.$$

The result is

$$\left.\frac{A_{eff}}{A}\right|_{A=56} \equiv S(x') = (1.0 - 0.33\exp(-28x'))^{0.76}.$$

This expression is used when discussing the effect of shadowing on the Q^2 dependence of ψ production. Since $S(x')$ varies from 0.7 to 1.0 as x' increases from zero, we use $\langle S(x')\rangle \equiv 0.85 \pm 0.15$ when an average value of A_{eff} is needed, as in the absolute normalization of the total cross section.

IV. ELASTIC RESULTS

IV.1 Muoproduction Cross Section

The cross section for ψ muoproduction on Fe is

$$\sigma = \frac{N_\psi}{L\epsilon_{el}B_{\mu^+\mu^-}} \times (c_1 c_2 c_3),$$

where,

N_ψ=number of observed $\psi + \psi'$ events=2627 ± 66,

L=integrated luminosiity=$(2.4 \times 10^{11}$ muons$)\times(4.4691$ kg/cm$^2) \times N_A$,

$B_{\mu^+\mu^-}$=branching ratio $\psi(3.1) \rightarrow \mu^+\mu^- = 0.069$,

ϵ_{el}=average detection and analysis efficiency=0.186.

Here $c_1 = 1.021$ and $c_2 = 1.075$ are the corrections to ϵ_{el} discussed in Section III.5 and c_3 is an estimate of the fraction of truly elastic psi events that are forced into the inelastic sample through the effects of radiative corrections and fluctuations in muon energy loss from the mean over the length of calorimeter which provides the measurement of E_{cal}. This latter effect is due to the high energy tail of the dE/dx distribution. While the mean energy lost by each muon is subtracted from E_{cal} for each event, as described in Sec. III.3.1, small coincidental electromagnetic showers in the region of the calorimeter surrounding the vertex can bring individual elastic events into the inelastic sample. To study this we look at the energy typically deposited in an equivalent number of calorimeter counters away from the vertex and find the fraction of events with E_{cal}>4.5 GeV. That fraction is $8.0^{+4.0}_{-2.5}$%. The error arises from considering different gaps between the vertex and the measurement area (small gaps are susceptible to punch-thru from true inelastic events, while

loss of particles or the finite size of the calorimeter can affect results using large gaps), different cuts on observed calorimeter energy, and various regions of muon pair mass. When we include the 5.9% feed-down factor due to radiative processes (Sec. III.6.1), we find that the net correction should increase the elastic cross section by a factor of $c_3 = 1.14$.

After applying these corrections, the cross section for elastic production of $\psi(3.1)$ on Fe is,

$$\sigma_{elastic}(\mu Fe \rightarrow \mu\psi X) = 0.40 \pm 0.01(stat.) \pm 0.08(syst.) \text{ nb/(Fe nucleon)}.$$

The result for σ(Fe) is converted to σ(nucleon) using the ratio of incoherent to all psi production, $f_{inc} = 0.78$ (section IV.2), and a nuclear screening factor (section III.7.2) of $(A_{eff}/A)_{Fe} = 0.85$. Then,

$$\sigma_{elastic}(\mu N \rightarrow \psi X) = 0.36 \pm 0.01(stat.) \pm 0.07(syst.) \text{ nb}.$$

The γGF prediction for $\sigma(\mu N \rightarrow \psi N) = 0.35$ nb, assuming $f_{c\bar{c}\rightarrow\psi} = 1/8$ and $\alpha_S = \alpha_S(Q^2 = m_\psi^2, \Lambda = 0.5 \text{ GeV}) = 0.41$.

The values of c_1 and c_2 give some estimate of the size of the systematic error in the elastic cross section normalization associated with uncertainties in the MC. In addition, $\sigma_{elastic}$ is sensitive to the 12% error in f_{inc} and the uncertainty in $(A_{eff}/A)_{Fe}$, which might be as much as $1.0/0.85 - 1 = 8\%$. Lastly, uncertainties in the factor c_3 which converts the calorimeter cut at 4.5 GeV into a definition of an "elastic event" increase the systematic error estimate. The value assigned to the above cross sections corresponds to an error of 20%.

IV.2 The t distribution

The optical model prediction for the general form of $d\sigma/dt$ in a nuclear target was presented in Eq. I.3. Previous experimental data[80,81] lead us to expect that $b_C \approx 150(\text{GeV/c})^{-2}$ and that the incoherent term will be better represented[82–84] by the sum of two exponential terms, $fe^{b_1 t} +$

$(1-f)e^{b_2 t}$, with $b_1^0 \approx 3(\mathrm{GeV/c})^{-2}$, $b_2^0 \approx 1(\mathrm{GeV/c})^{-2}$, and $f^0 \approx 7/8$. Therefore, were it possible, we would like to fit the data to the form,

$$d\sigma/dt = d\sigma/dt\,|_{t=0}\,[A_{eff}^2 e^{b_C t} + A_{eff}(f e^{b_1 t} + (1-f)e^{b_2 t})]. \qquad (IV.1)$$

Unfortunately, multiple Coulomb scattering in the spectrometer steel limits resolution at low t. This prevents us from resolving the coherent peak $e^{b_C t}$, and flattens the apparent slope of the incoherent part of $d\sigma/dt$ near $t = 0$.

The magnitude of the problem can be estimated from the form of the resolution function g which maps true t ($\equiv t$) into measured t ($\equiv \tilde{t}$). For $t \approx 0$,

$$g(\tilde{t} - t) = Ae^{b_{res}(\tilde{t}-t)},$$

where b_{res}=5 $(\mathrm{GeV/c})^{-2}$, implying poor sensitivity to any $b_C \gg b_{res}$. This is not a fatal problem, as the measurement of b_C itself is not of primary interest. Rather, the goals of the t analysis are the extraction of $d\sigma/dt$(incoherent), especially the measurement of the average t slope

$$(b_I)_{eff} = \left(\frac{f}{b_1} + \frac{1-f}{b_2}\right)^{-1}, \qquad (IV.2)$$

which can be used to convert normalized cross sections from σ to $d\sigma/dt$ if desired, and the measurement of the ratio of σ(coherent) to σ(incoherent) so that absolutely normalized results may be quoted independent of the steel target medium. Basically, these aims are accomplished by determining b_1, b_2, and f away from $t = 0$, and then extrapolating $d\sigma/dt$(incoherent) to $t = 0$ to measure the coherent to incoherent production ratio.

For these results the method of unfolding $g(\tilde{t} - t)$ and the acceptance $\epsilon(t)$ from the raw data is more complicated than that used for all other variables (Sec.III.4.4), as in this case one must subtract an a *priori* unknown amount of resolution smeared coherent signal from the data before

$d\sigma/dt$(incoherent) can be found. The relative size of the signal removed will depend on A_{eff}, b_C, b_1, b_2, and f, the quantities we seek to find. A straightforward way of accomplishing this would be to generate coherent and incoherent MC (C and I, respectively) using test values of these parameters (A'_{eff}, b'_C, b'_1, b'_2, and f') and to extract $d\sigma/dt$(incoherent) via an extension of Eqn. III.3 :

$$\frac{d\sigma}{dt}_{data}(t_i)(\text{incoherent}) = \frac{D_i - C_i}{I_i}\frac{d\sigma}{dt}_{MC}(t_i)(\text{incoherent}). \qquad (IV.3)$$

Here D_i, C_i, and I_i represent the observed number of events in the ith bin of measured $\tilde{t}$ for data, coherent MC, and incoherent MC, respectively, t_i is the average true value of t in that bin found using only the incoherent MC, and $d\sigma/dt_{MC}(t_i)$(incoherent) is that function $f'e^{b'_1 t} + (1-f')e^{b'_2 t}$ used to generate I_i. The best values of b_1, b_2, and f could then be determined by minimizing the χ^2 of $d\sigma/dt_{data}(t)$(incoherent) fit to $fe^{b_1 t} + (1-f)e^{b_2 t}$. This subtraction plus χ^2 minimization scheme is somewhat analagous to that described in Section III.3.5 for finding the number of ψ events above background.

The analysis procedure actually followed is a generalization of the above method, meant to overcome its requirement that we continually regenerate MC to form the final 5-parameter χ^2 grid. We instead use only one version of the MC (C^0 and I^0) generated according to Eq. IV.1 with the parameters set to the values b^0_C, b^0_1, b^0_2, f^0, and $A_{eff} = 0.85$ previously mentioned. If the MC simulation were the correctly normalized representation of reality we would have

$$D_i = C^0_i + I^0_i,$$

for each bin i in $\tilde{t}$. Since this will not in general be the case, we seek to find a set of coefficients a_i, d_i such that

$$C_i = a_i C^0_i$$
$$I_i = d_i I^0_i$$

can substitute for the C_i and I_i of Eq. IV.3. The a_i and d_i will be a function of the test parameters b'_C, f', b'_1, and b'_2 of C_i and I_i and those parameters used to generate C^0_i and I^0_i. If the efficiency

$\epsilon(t)$ and the resolution $g(\bar{t}-t)$ were known analytically, these functions could be found for each bin i by evaluating

$$\begin{bmatrix} C_i \\ I_i \end{bmatrix} = \int_{(\bar{t}_1)_i}^{(\bar{t}_2)_i} d\bar{t}\left(\int_{t_{min}}^{t_{max}} dt\begin{bmatrix} \epsilon_C(t)d\sigma/dt\,|_{t=0}(\nu,Q^2)A^2_{eff}e^{b_C t} \\ \epsilon_I(t)d\sigma/dt\,|_{t=0}(\nu,Q^2)A_{eff}[fe^{b_1 t}+(1-f)e^{b_2 t}] \end{bmatrix} g(\bar{t}-t)\right),$$

for each set of parameters. However, as this is not the case, we must make an approximation to this optimum solution.

Since any $b_C \gg 5$ (GeV/c)$^{-2}$ will have the same distribution in $\bar{t}$, changing b^0_C to b'_C will not change the ratio C_i/C^0_i as a function of i. It will only have the effect of changing the average coherent to incoherent mixture. That is, since $b_C t_{max} \gg 1$, we can approximate,

$$a_i = a = \frac{A'_{eff}/b'_C e^{b'_C t_{min}}}{A^0_{eff}/b^0_C e^{b^0_C t_{min}}}.$$

In general, because the incoherent distribution is spread over a larger range in true t, making the same simplification, $d_i = d$, is not as accurate. However, if the values of b^0_1, b^0_2, and f^0 used in the MC generation are not very different from the final result the approximation should be adequate. Then, since $b_{1,2}t_{min} \ll 1$ and $b_{1,2}t_{max} \gg 1$, we similarly have,

$$d_i = d = \frac{f'/b'_1 + (1-f')/b'_2}{f^0/b^0_1 + (1-f^0)/b^0_2}.$$

Thus we set

$$D_i = N(aC^0_i + dI^0_i),$$

where,

$$N \simeq \frac{D_T}{aC_T + dI_I}, \qquad \text{and} \qquad D_T = \sum_i D_i, \quad C_T = \sum_i C^0_i, \quad I_T = \sum_i I^0_i,$$

and find a, b_1, b_2, and f by minimizing the chisquared for

$$\frac{D_i - NaC^0_i}{dI^0_i}[f^0 e^{b^0_1 t} + (1-f^0)e^{b^0_2 t}]$$

fit to

$$N'[fe^{b_1 t} + (1-f)e^{b_2 t}].$$

Here N' is a normalization constant which should be approximately unity if the method and approximations used are valid. Five fits of this type were performed; their results are summarized in Table IV.1. In each b_1, b_2, and f were allowed to vary. The fits differ in which, if any, of the remaining parameters are constrained to fixed values.

Figure IV.1 (a) displays the number of events having $E_{cal} < 4.5$ GeV and muon pair masses in the region $-0.052 < \log_{10}(m_{\mu^+\mu^-}/3.1) < 0.052$ versus measured t, defined as $t_{min} + p_\perp^2$. The upper histogram is all data; the lower histogram is that fraction assumed caused by incoherent production, as parameterized by Fit 3, which is described below. Despite the fact that, as anticipated, no clear coherent peak is visible, when all parameters are left free to vary, the fitting procedure can measures the sizes of the coherent and incoherent components of $d\sigma/dt$ directly from the data, independent of additional assumptions. This is done in Fit 1, where the main parameter of interest is a. Deviations of a from unity are interpreted as changes in b_C from b_C^0, changes in A_{eff}/A from 0.85, or a breakdown in the optical model which fixes the relationship between coherent and incoherent contributions to $d\sigma/dt$ at $t = 0$. We find that $a = 0.62^{+0.98}_{-0.56}$. The corresponding measurements of b_1, b_2, and f can be used to calculate the average t slope $(b_I)_{eff}$ through Eq. IV.2 and f_C, the fraction of coherent events in the *measured* (i.e. uncorrected for acceptance) data,

$$f_C = \frac{aC_T}{aC_T + \frac{(b_I)^0_{eff}}{(b_I)_{eff}} I_T}.$$

These quantities are also shown in Table IV.1 for Fits 1 and 3. For Fit 1 we find that $f_C = 24^{+20}_{-16}\%$, implying that, even with our poor t resolution, we can independently determine that at the 1σ level at least 8% of the events recorded must arise from photons scattering off the iron nuclei.

In Fit 2, N' is fixed to unity and deviations of the other parameters from their N' free values (Fit 1) observed. This fit tests the sensitivity of the reported results to a parameter which gauges

the validity of the analysis procedure. Since the results of Fits 1 and 2 are within their quoted one sigma statistical errors, for the remaining fits N' is allowed to vary, with no significance attached to its value.

Since a is consistent with unity, and because there is no reason to doubt either the optical model constraint or the value of b_C^0 used, the best values for the incoherent parameters are calculated with $a \equiv 1$. These results are presented as Fit 3 in Table IV.1. We find that, the incoherent differential cross section is well fit by the sum of two exponentials,

$$(d\sigma/dt)_{incoherent} = 49.5 \text{ nb}/(\text{GeV}/c)^2[0.82e^{4.25t} + 0.18e^{0.93t}].$$

This curve is displayed in Figure IV.1(b), where we have plotted the absolutely normalized values of $d\sigma/dt$, corrected for coherent production, against true t. It is evident that one exponential term is not sufficient to describe $d\sigma/dt$(incoherent) over the range $|t| < 4\ (\text{GeV}/c)^2$.

Fits 4 and 5 are identical to Fit 3, but have a fixed at $0.70/0.85 = 0.82$ and at $1.0/0.85 = 1.18$, respectively, to provide an estimate of the systematic errors in b_1, b_2, and f of Fit 3 that are associated with variations in the assumed nuclear screening factor. When applied to $(b_I)_{eff}$ and f_C, we find that $(b_I)_{eff} = 2.56^{+0.35}_{-0.32}(stat.)^{+0.21}_{-0.17}(syst.)\ (\text{GeV}/c)^{-2}$ and $f_C = 0.30 \pm 0.03(stat.) \pm 0.02(syst.)$.

This value of $(b_I)_{eff}$ has been used to normalize the data and the curve in Figure IV.1(b) by requiring agreement between the integral of Fit 3 and the value of $\sigma_{\gamma\nu N\to\psi N}(\langle\nu\rangle, Q^2 = 0)$ reported in Section IV.4. The normalization uncertainty associated with $d\sigma/dt\,|_{t=0}$ is therefore greater that in $\sigma(\langle\nu\rangle)$ because of the errors in $(b_I)_{eff}$. To avoid introducing similar uncertainties when we later compare the ν dependence of this data with that of other experiments which explicitly measure the cross section through $d\sigma/dt$, we will present those results in terms of $\sigma(\nu)$, the primary measured quantity, and convert other measurements of $d\sigma/dt$ to σ by the reverse procedure.

Since b_C is large, t_{min} effects force coherent events to have a higher mean value of ν, and thus a higher detection efficiency, than the incoherent events. Once these acceptance effects are removed through the MC simulation, we find that the fraction of coherent events in the generated sample,

corresponding to $f_C = 30\%$, is $(f_C)_{gen} = 0.22$. This number is used to convert the ψ muoproduction cross section off iron to one which is independent of the target material.

In Table IV.2 are listed the values of $d\sigma/dt$(incoherent) plotted in Figure IV.1(b) versus their corresponding values of t. Also tabulated, in order to quantify the coherence correction displayed in Figure IV.1(a), are the apparent total differential cross section in each bin of measured $\tilde{t}$ (before any coherent signal subtraction is applied) and the value of the coherence correction specified by Fit 3.

IV.3 The Q^2 and Angular Distributions

While the general problem of ψ leptoproduction involves both $\sigma_T(Q^2,\nu)$ and $\sigma_L(Q^2,\nu)$, as described in Section I.1.1, the experimentally measured quantity is the effective cross section $\sigma_{eff} = (1+\epsilon R)\sigma_T$, where $R = \sigma_L/\sigma_T$ and $\epsilon = \Gamma_L/\Gamma_T$. In this section we describe[85] a measurement of the Q^2 dependence of σ_{eff}, and an attempt to measure R using as a tool the angular distribution $W(R;\theta,\phi)$ of the ψ daughter muons. As discussed in Section I.1.3, the decay angular distribution is a function of the ψ's polarization. If the SCHC and NPE model accurately describes how the helicity of the ψ is related to that of the exchanged virtual photon, as it does for the lower mass vector mesons, σ_L and σ_T can be seperated by analyzing $W(R;\theta,\phi)$.

This is not the standard technique usually employed, for example, by experiments[86] that seek to measure R for inclusive lepton inelastic scattering. There, one algebraically separates σ_L and σ_T by varying ϵ while keeping Q^2 and ν fixed, plotting σ_{eff} against ϵ to find the $\epsilon = 0$ intercept, σ_T, and the slope, σ_L. This method requires data at different beam energies, with large statistics and careful conrol of systematic effects at each energy. Since only data at $E_\mu = 209$ GeV are available for this analysis, we use the ψ polarization technique to measure R.

Note that the experiment does not attempt to quantitatively measure the level at which the SCHC and NPE hypothesis is satisfied, or other model choices ruled out. Rather, we introduce an *ad hoc* factor η to monitor the size of the $\cos 2\phi$ azimuthal asymmetry term in W, which must be

present if SCHC and NPE are satisfied, regardless of the value or form of R. Equation I.6 then becomes,

$$W(\eta,R;\theta,\phi) = \frac{3}{16\pi}\frac{1}{1+\epsilon R}[(1+\cos^2\theta) + 2\epsilon R\sin^2\theta - \eta\epsilon\sin^2\theta\cos 2\phi + \sqrt{2\epsilon R(1+\epsilon)}\sin 2\theta\cos\delta\cos\phi - H\sqrt{2\epsilon R(1-\epsilon)}\sin 2\theta\sin\delta\sin\phi]. \qquad (IV.4)$$

By fitting the data binned in θ, ϕ, and Q^2 to the product of $W(\eta,R)$ and the propagator $P(\Lambda) \simeq (1+Q^2/\Lambda^2)^{-2}$ we will simultaneously measure Λ and R while checking if the data are *consistent* (i.e., η=1) with SCHC and the NPE hypothesis.

An important feature of this analysis is that it allows for the possibility that the decay angular distribution is a function of Q^2 through the Q^2 dependence of R, e.g. $R \propto Q^2/m_\psi^2$ as suggested[87] by VMD. Since the experimental acceptance falls off rapidly away from $|\cos\theta| = 0$, such a Q^2 dependence could have biased our measurement of Λ if the data had been summed over all angles and the wrong form for W used. This global technique allows us to estimate the systematic errors introduced in the one quantity unique to leptoproduction experiments by one of the two variables on which the apparatus acceptance is most sensitive.

The terms in $W(\theta,\phi)$ proportional to $\sqrt{\epsilon R}\sin 2\theta$, sometimes called single-spin-flip terms, arise from the interference of the longitudinal and transverse scattering amplitudes. They predict a front-back asymmetry in the emitted μ^+ relative to the ψ direction of motion and involve an unknown phase δ. Since most of our data fall in the region around $\theta = \pi/2$ we expect our sensitivity to these terms to be low. Thus after first checking to see if an asymmetry is present, in order to prevent uncertainties in the measurement of δ from affecting R and η, we bin the data in θ and ϕ in such a way as to eliminate any effect of the $\sin 2\theta$ terms on $W(\theta,\phi)$.

To examine the $\sin 2\theta\cos\phi$ term, data and MC are accumulated in two regions defined as: (P)=[$\cos\theta > 0$, $|\phi| < \pi/2$ or $\cos\theta < 0$, $|\phi| > \pi/2$], and (N)=[$\cos\theta > 0$, $|\phi| > \pi/2$ or $\cos\theta < 0$, $|\phi| < \pi/2$]. Since finite Q^2 is needed to define a scattering plane from which to measure azimuthal angles, we remove the region of poorest ϕ resolution by requiring Q^2>0.3 (GeV/c)^2. Then data/MC

ratios for regions P and N are used to find

$$A_1 = \frac{2(P-N)}{(P+N)} = 0.12 \pm 0.16.$$

Similarly, the $\sin 2\theta \sin\phi$ term is isolated by considering (P)=[$\cos\theta > 0$, $\phi < 0$ or $\cos\theta < 0$, $\phi > 0$] and (N)=[$\cos\theta > 0$, $\phi > 0$ or $\cos\theta < 0$, $\phi < 0$]. In this case

$$A_2 = -0.21 \pm 0.16.$$

Using the average values of $\cos^2\theta$, $\cos 2\phi$, $\cos\phi$, $\cos 2\theta$, ϵ, and Q^2 for each region we can calculate the expected values of A_1, and A_2 as a function of R and δ. In Figure IV.2 these are presented as a family of curves in A_1 and A_2 space where each curve is labeled by a value of R and δ is the parameter along the curve. The region allowed by the data is indicated by the data point, where the errors are statistical only. All values of R are allowed and $\pi < \delta < 2\pi$. The single-spin-flip terms are henceforth dropped from the analysis.

The data were divided into a $4 \times 5 \times 3$ grid in Q^2, $|\cos\theta|$ and $\phi_F \equiv \frac{1}{2}\cos^{-1}|\cos 2\phi|$ (mapping $(-\pi, \pi)$ into $(0, \pi/2)$). Dimuon-mass-continuum subtractions were performed in each of the 60 bins to obtain a raw number of ψ events per bin. This raw ψ yield was corrected for acceptance and resolution effects by using the number of events and the average values of true Q^2, ϵ, $\cos^2\theta$, and $\cos 2\phi$ from the MC simulation for each bin in the standard manner described in Sec. III.4.4. The resulting acceptance corrected ψ yield, $d^2\sigma_{eff}(\gamma_V Fe \rightarrow \psi(diffractive))/d\phi d\cos\theta$, and the average values of true Q^2, $\cos^2\theta$, $\cos 2\phi$, and ϵ are tabulated in Table IV.3 (a)–(e), respectively. These differential effective cross sections are plotted in Figure IV.3 as a function of $|\cos\theta|$ for the 4×3 bins of Q^2 and ϕ_F. In order to provide a more compact display, Figure IV.4 shows the data summed over ϕ_F ($|\cos\theta|$) and plotted versus $|\cos\theta|$ (ϕ_F), for each Q^2 bin and for all Q^2. In order to leave out those data with very low resolution in ϕ, the ϕ_F plot labelled "all Q^2" is composed of data from all but the lowest Q^2 bin. In Figure IV.5 the data have been summed over ϕ_F and $|\cos\theta|$, normalized to unity at $Q^2 = 0$, and are plotted versus Q^2.

It is important to note that the ψ yields plotted in Figures IV.4 and IV.5 have *not* been corrected by any assumed dependence of the undisplayed variables. This implies that any coupling among Q^2, $\cos\theta$, and ϕ in the data could cause the displayed projections to have additional dependencies that one might not naively expect. The most striking example of this occurs in the $|\cos\theta|$ plots of Figure IV.4, because of the apparent need for the $-\epsilon\sin^2\theta\cos 2\phi$ term in W. When the data are summed over ϕ_F, each $|\cos\theta|$ point has an $\langle\cos 2\phi\rangle$ associated with it. These average values are in general not equal to zero (in fact, $\langle\cos 2\phi\rangle_{all} = -0.27$), and, in addition, can systematically vary from point to point (from —0.41 to —0.06 in the worst, $\langle Q^2\rangle = 1.6$, case). This behavior in $\cos 2\phi$ can result in a "spurious" $\sin^2\theta$ contribution in the plotted $\cos\theta$ projection that causes the shape of the data to look flatter than might be expected for any given value of R. In the example for instance, $R = 0$, implying $W(\theta) = 1 + \cos^2\theta$, would look like $1 + \cos^2\theta + 0.27\langle\epsilon\rangle\sin^2\theta$. These remarks only apply to the *displays* mentioned. The fits, being global in nature, do not have this complication. In Figures IV.4 and IV.5, the curves are plotted in exactly the same manner as the corresponding data, so that comparison between them does indicate the level of agreement with the assumptions of a given fit.

The details of the fits are presented in Table IV.4. In each fit A, η, and either R or ξ^2, as well as one adjustable normalization constant are parameters. Fits 1, 2, and 4 are to the SCHC formula with $R = \xi^2 Q^2/m_\psi^2$, constant, and zero, respectively; fit 3 corresponds to the flat angular distribution that would be expected in the production of unpolarized ψ's. In fit 5, A is fixed at 3.1 (GeV/c^2) and R at 0 to correspond to the simplest VMD expectation. In fit 6, an additional factor of $(1 + \epsilon R)$ is multiplied times $W(\eta, R)P(A)$ so that the resulting parameters apply to the transverse cross section, σ_T, rather than σ_{eff}. The γGF model has yielded no prediction for the ψ polarization, but does make a statement about the Q^2 dependence. We have fit the data in Figure IV.5 to the γGF prediction (fit 7), assuming the standard input to the model: a charmed quark mass $m_c = 1.5$ GeV/c^2 and a gluon fractional-momentum distribution $G(x) = 3(1-x)^5/x$.

An additional complication is the possible Q^2-dependence of any nuclear shadowing in the Fe target. In Sec III.6.2 we have summarized evidence for this effect in terms of the function $S(x')$,

where $x' \equiv Q^2/(2m_n\nu + m_n^2)$. The value of $S(x')$ for each of the 60 data bins is tabulated in Table IV.3(f). All fits are made both with and without $S(x')$ multiplying W. As the results in Table IV.4 indicate, including $S(x')$ lowers the fit propagator mass Λ, but hardly affects the angular results.

The results of fits 1 (solid) and fit 4 (dash) are shown in Fig. IV.3; fits 1–4 (so labeled) are shown in Fig. IV.4. All curves are for $S(x')$ "out" of the fit. The main feature of these angular distributions is a strong dependence upon ϕ_F, in the form predicted by SCHC. The production of unpolarized ψ's would yield a flat distribution (fit 3) which is ruled out. The data show no strong dependence on $|\cos\theta|$, but do not rule out $R = 0$ (fit 4). Comparison of fits 1 and 2 indicates that significant Q^2 dependence of R is not required. Unfortunately, variations of the fits attempted differ significantly only at $|\cos\theta| \approx 1$ where the acceptance substantially limits the amount of data.

The Q^2 dependence of fits 1, 5, and 7 is displayed in Figure IV.5. When the angular distribution is parameterized in the SCHC form with $R \propto Q^2$ and $S(x')$ included (Table IV.4, Fit 1) $\Lambda = 2.03^{+0.18}_{-0.12}$ GeV/c^2, where the statistical errors take into account the uncertainties in η and ξ^2. If instead, R=constant and $S(x')$ is left out (Fit 2) $\Lambda = 2.43 \pm 0.15$ GeV/c^2. The other fits to Λ, either for σ_{eff} or σ_T (fit 6), are within this 2.0–2.4 GeV/c^2 range; this ± 0.2 GeV/c^2 uncertainty is the principal systematic error in Λ. We conclude that Λ is between 1.9 and 2.6 GeV/c^2. The simplest VMD prediction, $\Lambda = m_\psi$ (fit 5) is at least 4σ away from the best fit. The Q^2 dependence of the γGF prediction is similar in nature to the VMD result, being determined primarily by the value assumed for m_c. The data fall faster than the γGF curve, giving a barely acceptable fit (7% confidence) when $S(x')$ is omitted. We have reached a similar, but less definitive, conclusion comparing γGF predictions with open-charm muoproduction, using a different analysis[88]. In that case, a redefinition of the point at which the strong coupling constant is evaluated suffices to bring the theory into agreement with the data. In the next section we will use the Q^2 and ν spectra of the ψ data to determine those parameters affecting the γGF predictions.

IV.4 The E_γ Distribution and its Variation with Q^2

These data, in addition to supplying a measurement of $\sigma_{\gamma N \to \psi N}(\nu, Q^2 = 0)$, are used to provide a definitive test for the γGF model. By fitting the combined Q^2 and ν spectra of the data simultaneously, we can determine the three basic input parameters to the model: the charmed quark mass, m_c, the power of $(1-x)$, η, in the assumed form (Eq. I.7) of $G(x)$, and the fraction of bound $c\bar{c}$ pairs produced that are realized as ψ's, $f_{c\bar{c}\to\psi}$.

As mentioned in Section I.2, the mass scale in the problem that allows the use of short distance ideas, and thus the perturbative QCD calculation, is $m_{c\bar{c}}^2 \simeq 10(\text{ GeV}/c^2)^2$, not Q^2. However, choosing $m_{c\bar{c}}^2$ as the point at which to evaluate the strong coupling constant α_S (as in Eq. I.8) is somewhat arbitrary. It has been suggested[89] that $m_{c\bar{c}}^2$ be replaced with $m_{c\bar{c}}^2 + Q^2$, as this additional Q^2 dependence is useful in bringing open-charm muoproduction calculations into agreement with experiment. In the fits, both forms of α_S will be considered.

To prepare for these fits, the data were divided into a 4×4 grid in measured Q^2 and ν, and dimuon-mass-continuum subtractions were performed for each bin to obtain a raw number of ψ events per bin. The MC simulation was used to correct these yields for acceptance and resolution effects and to produce the absolutely normalized effective cross sections for $\gamma_V N \to \psi N$. These are presented in Table IV.5 and Figure IV.6(b)-(e). The same correction factors that were discussed in connection with the normalization of the total elastic muoproduction cross section were applied to these results. We estimate the systematic error in the normalization as 20%. The form of the summed-over angular distribution used in extracting these differential Q^2 and ν results is that embodied by Fit 1 of Table IV.4 — the SCHC form with $R = 4Q^2/m_\psi^2$. Had we chosen to use $R = 0$ (Fit 4) the measured cross section would be larger at high $Q^2(\Lambda = 2.40 \pm 0.14)$, as indicated in the discussion of those fits. Likewise, the nuclear shadowing factor $S(x')$ is ignored. The changes to the results that would be introduced by its inclusion can be estimated from its effect on $P(\Lambda)$ as discussed earlier.

To report a measurement of $\sigma_{eff}(\nu)$ independent of Q^2 the data were summed over Q^2 and

extrapolated to $Q^2 = 0$ using $P(\Lambda) = (1+Q^2/\Lambda^2)^{-2}$ with $\Lambda = 2.18$ GeV/c^2. The data were divided into 6 bins in measured ν and, in the manner described above, normalized effective cross sections were independently measured for the process $\gamma N \to \psi N$. These results are tabulated in Table IV.5 and plotted in Figure IV.6(a), where we have also included the results[29] of a SLAC photoproduction experiment to cover the region $\nu < 25$ GeV. That experiment measured $d\sigma/dt\,|_{t=t_{min}}$ as a function of ν and t; we have converted their results to $\sigma(\nu)$ by dividing the data by the measured exponential t slope, $b = 2.9 \pm 0.3$(GeV/c)$^{-2}$. In some of the fits that follow we include the SLAC data with our own, but allow the relative normalization of the two data sets to vary by an amount consistent with the reported systematic error estimates of each. This is done so as to give the theory being fit any advantage the data might allow. This relative normalization constant is denoted as k; it is a number which multiplies the function being fit and which is defined as unity for our own data.

The details of the fits are presented in Table IV.6. Fits 1 and 2 have been made using only the Berkeley-Fermilab-Princeton (BFP) data differential in ν and Q^2. In Fit 1 $\sigma_{eff}(\nu, Q^2)$ is that calculated in the γGF model using the nominal values for the parameters m_c, η, and α_S; in Fit 2, $f_{c\bar{c}\to\psi}$, m_c, and η are allowed to vary. Fit 3 is of the same form as Fit 2, but includes the $Q^2 = 0$ SLAC data and the relative normalization constant k. Fit 4 is identical to Fit 3 in all respects except the specification of $m_{c\bar{c}}^2 + Q^2$ as the point at which α_S is to be evaluated. In Fits 5 and 6 the ν dependence of σ_{eff} is examined independently of Q^2 by considering only the SLAC data and the BFP data extrapolated to $Q^2 = 0$. In Fit 5 (6) m_c is fixed at 1.5 GeV/c^2 (1.1 GeV/c^2), and all other parameters are allowed to vary. The results of Fits 1 (dash) and 2 (solid) are shown in Figure IV.6(b)-(e), and results of Fit 3 (solid), extrapolated to $Q^2 = 0$, and Fit 5 (dash) in Figure IV.6(a). For reference we note a phenomenological fit to the data in Figure IV.6(a) as plotted (i.e. $k \equiv 1$) to be $\sigma(\nu) = (20.5 \pm 0.7)\log_{10}\frac{\nu}{11.5\pm0.3}$, $\chi^2 = 5.2$ for 9 degrees of freedom.

The inescapable conclusion of this analysis is that the γGF model provides an excellent description of the ν dependence of elastic ψ production but cannot be made to explain simultaneously the observed value of the cross section and the low Q^2 propagator mass. The model with standard

parameters (Fit 1) yields a χ^2 of 40.3 for 15 degrees of freedom, corresponding to a confidence level of 4.5×10^{-4}. Examination of Figure IV.6(b)-(e) shows this to be predominantly a Q^2 effect. When the parameters are set free to optimize the fit we find (Fit 2) $m_c = 1.10 \pm 0.08$ (corresponding to $\Lambda = 2.18^{+0.18}_{-0.13}$). The increase in phase space made available by the lowered threshold of $2m_c$ causes the predicted cross section to rise to approximately 9 times that seen in the data; the data would imply that $f_{c\bar{c}\to\psi} \simeq 1/72.7$ rather than the 1/8 originally assumed. In this case the best fit value of η is 9.2 ± 1.2, higher than the value 5 gotten from power counting arguments. These conclusions remain unchanged whether or not we include the SLAC photoproduction data in the fit (Fit 3) or, more significantly, change the "Q^2" equivalent term in α_S from $m^2_{c\bar{c}}$ to $m^2_{c\bar{c}} + Q^2$. (Fit 4). We note again that speculations concerning $W(\theta, \phi)$ and $S(x')$ can slightly reduce the significance of these results.

Fit 5 isolates the ν dependence of the γGF model with m_c fixed at its standard value of 1.5 GeV/c^2. If the problems in Q^2 can somehow be solved, Fit 5 becomes a model dependent measurement of the gluon distribution in a nucleon at values of "Q^2" $\simeq m^2_{c\bar{c}} \simeq 10$(GeV/$c^2$)^2. The resulting power of $(1 - x)$ is $\eta = 5.25 \pm 0.41$, in agreement with a similar measurement[49] made using a previously published fraction of this data. Fit 6 indicates that η is forced to a value of ~ 9 whenever m_c is constrained by the fit or the Q^2 binned data to the low value of 1.1 GeV/c^2. Thus the high values of η found in fits 2, 3, or 6 do not necessarily imply that the gluon frational momentum distribution $G(x)$ need be changed from the standard γGF choice in order to explain the ν dependence of the data; they are more the algebraic result of redefining $x = (m^2_{c\bar{c}} + Q^2)/2m_n\nu$ when m_c is lowered.

In the general quantum chromodynamic calculation the exponent η would develop with Q^2 in the manner described by the Altarelli-Parisi equations[90]. In that case we would view[91] η as a function of $s \equiv \ln(\ln(\text{"}Q^2\text{"})/\Lambda^2/\ln(Q_0^2/\Lambda^2))$ with "Q^2" $\equiv m^2_{c\bar{c}} + Q^2$ in the γGF calculation. For the choice of $Q_0^2 = 1.8$(GeV/c)^2 and the range of Q^2 in our data from $4m_c^2$ to $4m_D^2 + Q^2_{max}$ we expect a maximum range in s of approximately 0.4 (using $m_c = 1.1$ GeV/c^2, $Q^2_{max} = 20.6$(GeV/c)^2, $\Lambda =$

0.5 GeV/c). The data are not sensitive to this range in s. For example, fitting $\eta(s) = \eta(0) + bs$ does not lead to new information; it merely changes the point in "Q^2" that η refers to from the data's average value of approximately 10(GeV/c^2)^2 to some arbitrary Q_0^2.

V. INELASTIC RESULTS

The 1755 ± 51 ψ event inelastic sample is subdivided into two regions, based on elasticity, as described in Section III.4.3. Throughout this chapter, results will be presented separately for each region. Events with $z < 0.7$ should form a clean sample which can be interpreted in terms of hard QCD processes, while those with $z > 0.7$ may be partly due to elastic production of higher mass $c\bar{c}$ bound states that then decay.

V.1 The Muoproduction Cross Section

The number of ψ events with $z < 0.7$ ($z > 0.7$) is 559.3 ± 26.9 (1196.1 ± 42.9). To convert these numbers to cross sections we use the average detection and analysis efficiencies quoted in Sec.III.4.3,

$$\langle\epsilon\rangle_{z<0.7} = 0.120 \pm 0.008 \quad \text{and} \quad \langle\epsilon\rangle_{z>0.7} = 0.185 \pm 0.007.$$

Two corrections are applied. First, we compensate for the different fractions of data and MC that are lost by applying analysis cuts (Sec.III.5) by increasing the cross section by a factor of $c_1 = 1.132$. Assuming that all inelastic production is incoherent, and using the same luminosity, $\mu^+\mu^-$ branching ratio, and average nuclear shadowing factor as we did for the elastic cross section, we find that, including c_1,

$$\sigma(z < 0.7)_{\text{uncorrected}} = 0.140 \pm 0.007 \text{ nb/nucleon},$$

and

$$\sigma(z > 0.7)_{\text{uncorrected}} = 0.194 \pm 0.007 \text{ nb/nucleon}.$$

The second correction is needed to compensate for the factor of $c_3 = 1.14$ increase in the elastic cross section that accounted for elastic events lost to the inelastic sample by electromagnetic processes, such as radiative corrections and dE/dx fluctuations. The total size of this correction is

$$\sigma_{corr} = \left(1 - \frac{1}{1.14}\right)\frac{0.40}{0.85} \text{ nb/ Fe nucleon} = 0.057 \text{ nb/ Fe nucleon},$$

assuming that the inelastic cross section has no coherent component and that both coherent and incoherent parts of the elastic signal can contribute to the feed-down. These events are expected to predominately affect the region $z > 0.7$. To estimate their z distribution we examine the quantity $1 - \text{"}E_{cal}\text{"}/\nu$ for those events which lead to the $8.0^{+4.0}_{-2.5}\%$ dE/dx fluctuation correction used in Section IV.1. We assume the z distribution of the 6% radiatiative correction is similar in shape. "E_{cal}" is the energy typically deposited in an equivalent number of calorimeter counters in a region away from the vertex. We list "$efdc$", the elastic feed-down correction, as a function of z in Table V.1. The cross section correction for any bin, σ^i_{corr}, is given by $(1 - efdc_i)\sigma_{corr}$. Note in particular the large value of σ^i_{corr} for the 0.9 – 1.0 bin. The size and uncertainty of the calculation are sufficient to make the plotting of such a point meaningless. Therefore, in all results to follow we quote results only for the $z < 0.7$, $0.7 < z < 0.9$, or the combined $z < 0.9$ regions.

Reducing the uncorrected results by 4.5% (95.5%) of the 0.057 nb correction for elastic feed-down in the $z < 0.7$ ($z > 0.7$) regions we have

$$\sigma(z < 0.7)_{inelastic} = 0.14 \pm 0.01(stat.) \pm 0.02(syst.) \text{ nb},$$

and

$$\sigma(z > 0.7)_{inelastic} = 0.14 \pm 0.01(stat.) \pm 0.03(syst.) \text{ nb}.$$

This leads to a total inelastic cross section of

$$\sigma_{inelastic}(\mu N \to \psi X) = 0.28 \pm 0.03(stat.) \pm 0.05(syst.) \text{ nb}.$$

Including the elastic contribution we find that that the total muoproduction cross section for ψ production is

$$\sigma_{tot}(\mu N \rightarrow \psi X) = 0.64 \pm 0.03(stat.) \pm 0.10(syst.) \text{ nb}.$$

The systematic error for the inelastic cross section arises predominately from uncertainities in the measurement of the average ψ detection efficiency and in the calculation of σ_{corr}. The most critical parameters in determining the detection efficiency are the energies of the final state muons. These are controlled by the ν distribution assumed in the MC simulation. Our own inelastic data lie at $\nu > 40$ GeV; since there are no other inelastic ψ experiments which determine the cross section in the low ν region, $\langle\epsilon\rangle$ is sensitive to our assumptions concerning the threshold behavior of the production. To study this effect we parameterized the ν dependence of the simulation in the form $\log \nu/\nu_{th}$ and examined the average trigger efficiency as a function of ν_{th}. For $\nu_{th} \simeq 10$ GeV, the sensitivity of $\langle E\rangle$ to ν_{th} is given by $\Delta\epsilon/\epsilon = 0.03\Delta\nu_{th}$(GeV), implying that a 5 GeV change in ν_{th} can result in a 15% change in ϵ. We have used a value of $\nu_{th} = 9.7$ GeV in the measurement of $\langle\epsilon\rangle$, as we did for the elastic case, where lower energy photoproduction measurements fix the low ν behavior of the cross section.

The size of the overall correction factor c_1 is another estimate of the level at which the MC simulation reflects the data. It is larger than the corresponding elastic value partly because of insufficiently modeled wire chamber hit populations, which cause data, but not MC, events to be removed from the sample. Also, as in the elastic case, σ is sensitive to uncertainties in $(A_{eff}/A)_{Fe}$. We estimate the combined magnitude of all these effects to be approximately 15% and assign this as the systematic error on the cross section when uncertainties in σ_{corr} can be ignored, as for either the total cross section or $\sigma_{inelastic}(z < 0.7)$. The estimated error in the 1.14 elastic feed-down correction is ± 0.07. When quoting errors on $\sigma_{elastic}$, $\sigma_{inelastic}$, and $\sigma_{inelastic}(z > 0.7)$ this 6% contribution is added linearly to 15% quoted above.

V.2 The Elasticity Distribution

After dividing the data in bins of measured $z \equiv E_\psi/E_\gamma$ and finding the raw number of ψ events per bin, the MC simulation described in Sec. III.4.3 is used to unfold acceptance and resolution effects to obtain the corrected ψ yield as a function of z. Displayed in Figure V.1(b) are the values of $d^2\sigma(\gamma_V N \rightarrow \psi X)/dz dp_\perp^2$ in arbitrary units as a function of z; the points plotted are listed in Table V.1. The data have been corrected for feed-down from the elastic sample as described in the previous section. The values of the corrections applied, labeled $efdc$, are also indicated in Table V.1. The errors indicated for $z < 0.7$ are statistical only. Those for $z > 0.7$ have had the estimated error in $efdc$ added in quadrature to the statistical error, whose contribution is indicated separately by the horizontal marks on the error flag. No point is plotted for $0.9 < z < 1.0$ because of the large size and uncertainty of the correction and the proximity of the elastic boundary, which can introduce errors in the efficiency measurement.

A measurement[92] of inelastic ψ production has been made by the European Muon Collaboration (EMC). In order to compare our own data with their result in z, we present the absolutely normalized cross section, $d\sigma_{eff}(\mu N \rightarrow \psi X)/dz$ vs. z in Figure V.1(a). The same remarks on corrections and errors that were made in the preceding paragraph apply in this case also. The $\Delta\sigma$ of each bin of measured z is the experimental measured quantity; their sum yields the muoproduction cross sections discussed in the previous section. Bin edge resolution effects (Sec.III.4.4) which enter in the conversion of $\Delta\sigma$ to $d\sigma/dz$ are handled only approximately by finding, via the MC simulation, the average values of true z for each bin and calculating a Δz using the midpoints of the series of $(z_i)_{true}$ thus obtained. The values of $d\sigma/dz$, Δz, statistical errors in $\Delta\sigma/\Delta z$, and the applied corrections are listed in Table V.1. The EMC data, which were presented in arbitrary units, have been normalized in Figure V.1(a) so as to minimize any discrepancy with our own result for $z < 0.9$.

In Figure V.1 the solid line labeled $(\gamma g \rightarrow \psi g)$ represents the result of the inelastic ψ photoproduction calculation of E. Berger and D. Jones[55]. In part (a) the photoproduction prediction for $d\sigma/dz$, evaluated using $E_\gamma = 106$ GeV and normalized to maximally agree with the BFP data, is plotted

against the muoproduction result. The χ^2 for the curve is 42 for 6 degrees of freedom. In part (b) we have evaluated $d^2\sigma/dzdp_\perp^2$ using $E_\gamma = 106$ GeV and $\langle p_\perp^2 \rangle = 1.26(\mathrm{GeV}/c)^2$ and plotted it in like manner agains $d^2\sigma_{eff}/dzdp_\perp^2$. The χ^2 for this plot is 25 for 6 degrees of freedom.

There is no substantial difference between the shape of the data in $d\sigma(\mu N \to \psi X)/dz$ and that of $d^2\sigma_{eff}(\gamma_V N \to \psi X)/dzdp_\perp^2$. Furthermore, there is good agreement between the EMC result and our own measurement of $d\sigma/dz$. We see that the $\gamma g \to \psi g$ calculation qualitatively agrees in both forms plotted. The level of agreement observed in the $z > 0.7$ region is surprising. If $\psi' \to \psi X$ events were being produced at the rate $\sigma(\psi')/\sigma(\psi) = 0.38$, expected from simple VMD arguments (Sec. III.4.2), we would expect the data points to fall above the $\gamma g \to \psi g$ curve by an amount equal to the size of the $\psi' \to \psi X$ simulation plotted in Figure V.1. This does not appear to be the case. Lastly, we note the phenomenological form of $d^2\sigma/dzdp_\perp^2$ used to describe the data, before correction for elastic feed-down, in the MC simulation:

$$d^2\sigma/dzdp_\perp^2 \propto z(1 - \exp(-z^2/0.54)).$$

V.3 The Angular Distribution of $\psi \to \mu^+\mu^-$

The angular analysis of the inelastic ψ sample is carried out in terms of the same angles, θ and ϕ, used in the description of elastic ψ production. While we intuitively expect less evidence of $\gamma_V - \psi$ helicity conservation when the production process is non-diffractive, there are no quantitative predictions for the dependence of the effective cross section on θ and ϕ.

The data were separated into the two regions of elasticity, $0 < z < 0.7$ and $0.7 < z < 0.9$, and the acceptance corrected ψ yield evaluated for each as a function of $|\cos\theta|$ and of ϕ_F. The values of the effective differential cross section for the reaction $\gamma_V \mathrm{Fe} \to \psi X$ ($E_X > 4.5$ GeV), differential in $\cos\theta$ (ϕ), are presented in Figure V.2 (Figure V.3). The $|\cos\theta|$ result is shown separately for data summed over Q^2 and for data lying below and above a Q^2 cut at 0.4 $(\mathrm{GeV}/c)^2$. To avoid diluting

any ϕ dependence of σ_{eff} with data having poor ϕ resolution, that plot contains only events from the high Q^2 region. Note that, contrary to the procedure followed in the elastic angular analysis, the $\cos\theta$ and ϕ results displayed here have been found using an acceptance whose calculation assumed the dependence of σ_{eff} on undisplayed variables listed in Eqns. III.1 and III.2. Each plot is arbitrarily normalized to unity at either $|\cos\theta| = 0$ or $\theta_F = \pi/4$ ($\cos 2\phi = 0$). Tables V.2 and V.3 list the points plotted in Figures V.2 and V.3, respectively.

Also listed in Tables V.2 and V.3 are the best parameters of simple phenomenological fits to the differential cross section measurements. The $|\cos\theta|$ data are fit to the form $1 + \eta_C \cos^2\theta$, while the data binned in ϕ_F are fit to $1 + \eta_A \cos 2\phi$. The purely inelastic, $z < 0.7$, data are consistent with flat distributions in either variable, independent of Q^2. The results in the $0.7 < z < 0.9$ region suggest the prescence of elastic processes through non-flat angular distributions. The most striking cases are $\eta_C = 1.3 \pm 0.7$ value in the $\cos\theta$ dependence of the $Q^2 < 0.4$ data and the $\eta_A = -0.41 \pm 0.12$ result in the shape of the ϕ_F distribution. Conclusions drawn from the possible discrepancy between the z regions must be labeled as speculative.

V.4 The $p_\perp^2$ distribution

The variable in inelastic ψ production that is analagous to t in elastic scattering is the $p_\perp^2$ of the ψ, measured with respect to the γ_V momentum. Since $t \equiv (p_\gamma - p_\psi)^2$, differences in the longitudinal momentum components, implied by non-unit elasticity, make it spuriously large for inelastic events and therefore inappropriate for use. Even for elastic production, finite momentum resolution forces the experimentally measured t to be evaluated as $t_{min} + (p_\perp^2)_\psi$, rather than calculated through the above formula. Since t_{min} is very low ($\simeq 10^{-3}$(GeV/c)^2) at the average ν of these data, there is essentially no difference between t and $p_\perp^2$.

We find the $p_\perp^2$ dependence of the effective cross section for the reaction $\gamma_V \mathrm{Fe} \rightarrow \psi X(E_X >$ 4.5 GeV) in the standard manner previously described. Figure V.4(a) and (b) show $d^2\sigma_{eff}/dz dp_\perp^2$

with statistical errors in arbitrary units vs. $p_\perp^2$ for events with $0 < z < 0.7$ and $0.7 < z < 0.9$. Table V.4 lists the information plotted in the figure. The curves drawn in Figure V.4 are the results of Berger and Jones' $\gamma g \to \psi g$ QCD calculation for inelastic ψ photoproduction. We have evaluated their result for $d^2\sigma/dzdp_\perp^2$ vs. $p_\perp^2$ using the average values $\langle\nu\rangle = 123$ GeV and $\langle z\rangle = 0.58$ of the $z < 0.7$ data (or $\langle\nu\rangle = 100$ GeV, $\langle z\rangle = 0.81$ for the high z data).

The $p_\perp^2$ dependence of the inelastic data can be parameterized by the same functional form used for the elastic incoherent cross section. We have,

$$d\sigma/dt \propto 0.72e^{1.69p_\perp^2} + 0.28e^{0.52p_\perp^2} \qquad 0 < z < 0.7,$$

and

$$d\sigma/dt \propto 0.86e^{2.42p_\perp^2} + 0.14e^{0.45p_\perp^2} \qquad 0.7 < z < 0.9.$$

The average $p_\perp^2$ slopes in each case are much lower than is seen in the elastic data. We have $(b_I)_{eff} = 1.02 \pm 0.25(\mathrm{GeV}/c)^{-2}$ and $1.54 \pm 0.11(\mathrm{GeV}/c)^{-2}$, respectively, for the low and high z regions, compared to the value $2.56^{+0.35}_{-0.32}(\mathrm{GeV}/c)^{-2}$ found for elastic production. In evaluating the inelastic muoproduction cross section, we assumed that there is no contribution from coherent production off the iron nuclei; these results support that hypothesis.

The $\gamma g \to \psi g$ calculation is in good agreement with the data. It successfully describes the changing slope of $d^2\sigma/dzdp_\perp^2$ with respect to $p_\perp^2$, not only in the $z < 0.7$ region, but also in the $0.7 < z < 0.9$ region where discrepancies might be expected due to ψ' cascade or elastic feed-down processes.

V.5 The Q^2 Distribution

The Q^2 dependence of σ_{eff} for inelastic events has been evaluated by unfolding apparatus acceptance and resolution from the raw ψ yield with the inelastic MC simulation. The sensitivity of the result to assumptions concerning nuclear shadowing, the Q^2 dependence of σ_L/σ_T, or the form of the $\psi \rightarrow \mu^+\mu^-$ angular distribution has not been explicitly investigated, as it was for elastic production. The results presented here assume $R = \sigma_L/\sigma_T = 0$ and no Q^2 dependence in nuclear shadowing; the angular distributions used were those that best describe the data for all Q^2 in each of the two z regions (Tables V.2 and V.3). The effect of changing these assumptions is small and can be estimated by considering the elastic results (Table IV.4). The above choices imply that the appropriate elastic production propagator mass to compare the following results with is $\Lambda_{el} = 2.40 \pm 0.14$ GeV/c^2 (Table IV.4, fit 4).

The effective cross section for the reaction γ_VFe $\rightarrow \psi X$ ($E_X > 4.5$ GeV), normalized to unity at $Q^2 = 0$, is presented *vs.* Q^2 in Figure V.5. The errors shown are statistical only. Table V.5 lists the plotted information. The two upper data sets plotted refer to events with $0 < z < 0.7$ (open circles) and $0.7 < z < 0.9$ (filled squares). Each set is well fit by a Q^2 dependence of the propagator form $P(\Lambda)$. We find $\Lambda = 3.10 \pm 0.37(stat.)$ GeV/c^2 ($\chi^2 = 2.6$ for 7 df) for the low z data and $\Lambda = 2.61 \pm 0.20(stat.)$ GeV/c^2 ($\chi^2 = 8.6$ for 7 df) for the data in the high z region. In the lower part of the figure we combine data from both z regions and compare the result (filled circles) with that previously obtained[92] by the EMC (open squares). Note that while our own data satisfy $z < 0.9$, those of EMC span all z. The result of a propagator fit to the BFP data is $\Lambda = 2.98 \pm 0.21$ GeV/c^2 ($\chi^2 = 7.2$ for 7 df). This measurement of Λ might be considered as rather large, given the values and statistical errors of Λ for each of the two subsets. It results from the non-linear nature of $P(\Lambda)$ and the importance of the highest Q^2 data points in determining Λ. The propagator mass quoted by the EMC is 1.8 ± 0.2 GeV/c^2.

While the difference in fit Λ for the low and high z regions is not significant, the BFP($z < 0.9$) and EMC results reflect a discrepancy of 4.2 statistical standard deviations. Ascribing this to the

$0.9 < z < 1.0$ data left out of the BFP sample[93] would require a very steep decline of σ_{eff} with Q^2 for that sample. As Q^2 is kinematically unrelated to z, it is unrealistic to expect such a behavior. No mechanism is known at this time that can resolve the discrepancy.

We find that the fit elastic propagator A_{el} is also lower than that measured in the $z < 0.9$ region, by 2.3 statistical standard deviations. The systematic effects we have discussed would not change this result, as they affect both elastic and inelastic events in the same manner. Assigning the value $z = 1$ to the elastic result only moderately increases the significance of the apparent systematic increase of A with decreasing elasticity.

The particular $\gamma g \rightarrow \psi g$ calculation to which we have compared our results in other variables has not yet been extended to the case of leptoproduction. However, other authors have calculated predictions for inelastic ψ production by virtual photons based on similar perturbative QCD ideas. W.Y. Keung graphically presents[56] the Q^2 dependence of $Q^2 d\sigma/dQ^2$ for $\gamma_V g \rightarrow \psi g$, where the calculation is based on the same six Feynman diagrams (Figure I.4 (a)-(c)) considered by Berger and Jones. The result is essentially a propagator shape $P(A)$ with $A = 3.1$ GeV/c^2, arising because of the canonical (zero binding energy) choice of charmed quark mass, $m_c = m_\psi/2$. This prediction is essentially unchanged from that for elastic ψ production through the photon-gluon fusion mechanism. However, in this case, the data for inelastic production support the calculation. D.W. Duke and J.F. Owens have also performed a calculation[58] for inelastic ψ leptoproduction based on the $\gamma g \rightarrow \psi g$ subprocesses. They also include the contributions of both diffractive and non-diffractive $\gamma q \rightarrow \psi q$ diagrams, where q represents a light valence quark from the nucleon target. While their text claims that the Q^2 dependence observed by the EMC is well described by the calculations, examination of the accompanying figure shows clearly that their Q^2 dependence is also essentially that of a propagator $P(A)$ with $A = 3.1$ GeV/c^2.

The only theoretical support for a Q^2 dependence which falls faster than that which we have observed comes from J.P. Leveille and T. Weiler who have separately considered[53] only those $\gamma q \rightarrow \psi q$ subprocceses that are non-diffractive (Figure I.4 (g)-(h)). Their conclusion is that the ratio of non-diffractive to diffractive ψ production should fall rapidly as Q^2 increases from zero (the ratio

$(m_\psi/m_\rho)^4(m_\rho^2+Q^2/m_\psi^2+Q^2)^2$ is suggested), arriving at a constant value when $Q^2 \geq\sim 6(\mathrm{GeV}/c)^2$. Our data imply that these processes alone cannot account for the majority of the inelastic ψ signal.

V.6 The E_γ Distribution

The effective cross section for inelastic ψ production by muons is presented as a function of incident virtual photon energy in Figure V.6. The data are absolutely normalized and plotted with statistical errors for the elasticity regions $z < 0.7$ (part (b)), $0.7 < z < 0.9$ (part (c)), and $z < 0.9$ (part (a)). The same correction factors affecting the normalization of the inelastic muoproduction cross section, with their associated systematic uncertainties, as discussed in Sec. V.1, have been included here. The data have been extrapolated to $Q^2 = 0$ by using the observed propagator dependence $P(Q^2;\Lambda)$, with the value of Λ appropriate to each z region. Table V.6 provides a list of plotted data. The overall similarity in the shape of the data for $z < 0.7$ and $0.7 < z < 0.9$ shows that, at least for $z < 0.9$, the ν dependence of the cross section is essentially independent of elasticity. When the data are fit to the simple phenomenological form $\sigma(\nu) = A\nu^p$ the results listed in Table V.7 are obtained.

In each part of Figure V.6 we have shown the E_γ dependence of the Berger–Jones $\gamma g \to \psi g$ QCD calculation for $\sigma(\gamma N \to \psi X)$ (solid line) and the result of the phenomenological fit, $\sigma_{el} = (20.5\ \mathrm{nb})\log_{10}\nu/(11.5\ \mathrm{GeV})$ (essentially identical to the γGF form), to the effective cross section data for elastic ψ production plotted in Figure IV.6(a). The curves have been multiplied by the constant factors listed in the figure in order to maximize their agreement with the data. The shapes of the $\gamma g \to \psi g$ and elastic fit curves are similar in nature, due to the fact that each is dominated by the behavior of the gluon's fractional momentum distribution $G(x)$. Either curve provides an adequate description of the cross section, although both tend to rise more slowly with ν than do the data at the highest values of ν reported. The constants normalizing the elastic fit curve are consistent with the division of total cross section into elastic and inelastic parts reported earlier; to

wit, roughly half the ψ's produced are associated with the presence of additional hadronic energy.

Note that in Figure V.6 we have assumed that the E_γ dependence of the $\gamma g \to \psi g$ prediction is uncorrelated with z. The curve drawn in each part of the figure is that found by integrating $d^2\sigma/dzdp_\perp^2$ over *all* z and $p_\perp^2$. The absolute normalization assumed for each curve is that presented by Berger and Jones for all z, but scaled by the fraction of events predicted to lie in the appropriate z region. These fractions have been calculated to be 0.33, 0.37, and 0.70, for the $z < 0.7$, $0.7 < z < 0.9$, and $z < 0.9$ regions, respectively, by evaluating $d\sigma/dz$ at the average energy ($E_\gamma = 104.4$ GeV) of the $z < 0.9$ data. The changing value of the constant needed to bring the $\gamma g \to \psi g$ prediction into agreement with the data reflects the relatively minor discrepancies between these fractions and those observed in the data.

The fact that each of these numbers is ~ 5.5 indicates a fundamental flaw in the theory as a description of inelastic ψ production. This cannot be explained away by the existence of higher mass $c\bar{c}$ cascade events, as the discrepancy is independently observed in the $z < 0.7$ data, which are free of this process. Nor is the systematic uncertainity in the normalization large enough to account for such a number. The factors which influence the theoretical normalization are the values chosen for m_c and α_S, the specification of the subprocesses to be considered, and the decision to treat the ψ as a wavefunction normalized through the its leptonic decay width. These results provide support for a theory whose energy dependence is dominated by gluon exchange, with $xG(x) \propto (1-x)^5$, but which is not necessarily limited to the fundamental subprocess $\gamma g \to \psi g$. If m_c could somehow be lowered from the value $m_\psi/2$ chosen, without spoiling the Q^2 agreement seen in similar[56,58] leptoproduction calculations which use 1.5 GeV (Sec. V.5), or α_S raised, or the wavefunction normalization freed from its constraint of providing the correct value of $\Gamma(\psi \to \mu^+\mu^-)$, the Berger–Jones calculation would provide an adequate description of the data.

In Figure V.6(a) we have also plotted the result for $\sigma_{eff}(\gamma N \to \psi X)$ found by the EMC. Their absolutely normalized measurement encompasses all events with $E_X > 5$ GeV, independent of the questions of calorimeter resolution or electromagnetically produced elastic feed-down processes. To

compare their data with our $z < 0.9$ result we have multiplied their published[92] inelastic cross sections by 0.726, that fraction which they observed below z of 0.9. While the BFP results agree in the value of σ_{eff} observed at $E_\gamma = 120$ GeV, the mean photon energy of the samples, the EMC data rise more steeply with photon energy and exhibit an effective threshold at $E_\gamma > 50$ GeV.

Unlike the situation in Q^2, it may be possible that this discrepancy is attributable to the difference in z regions of the samples, as there is a direct relationship between z and ν: $z = E_\psi/\nu = 1 - E_{cal}/\nu$. For a given $\langle E_{cal}\rangle$, events at high z should correspond to high ν. Were these $z > 0.9$ events to be included in the BFP sample, we might see the cross section increase sufficiently at high ν to resolve the discrepancy[93].

The $\gamma_V g \to \psi g$ calculation of W.Y. Keung in Reference 56 yields results similar to those plotted in Figure V.6. The normalization of that prediction is such that $\sigma_{\gamma N \to \psi N}(\nu = 100 \text{ GeV}) = 6.4$ nb, as compared to 4.3 nb for the $\gamma g \to \psi g$ curve plotted. The increase is insufficient to resolve the discrepancy with the data.

In Reference 58, discussed earlier in regard to the Q^2 dependence of inelastic ψ production, Duke and Owens have also predicted the E_γ dependence of $\sigma_{eff}(\gamma_V N \to \psi X, E_X > 5 \text{ GeV})$ and compared their results with the EMC data. As their calculation is basically an extension of the γGF model it incorporates the SLD hypothesis to specialize from inclusive $c\bar{c}$ results to ψ production, with the corresponding normalization uncertainty induced by $f_{c\bar{c}\to\psi}$. If they fix $f_{c\bar{c}\to\psi}$ with the EMC elastic data sample, they find excellent agreement with the EMC inelastic data in both shape and normalization. Thus, their calculation will apparently[94] conflict with the E_γ dependence of the BFP data, while accurately fitting the relative normalization of the elastic and inelastic samples.

VI. SUMMARY and CONCLUSIONS

The study of ψ production by muons can provide information valuable to the understanding of the dynamics of heavy quark interactions. A qualitative description of the photon-nucleon interaction that results in diffractive ψ production is provided by the vector dominance model. The physical picture it supplies has been recently quantified in many respects by first order QCD perturbation theory calculations (generically termed γGF calculations), which justify their significance by the small value of the strong coupling constant in heavy quark production. By extending these calculations to include second order processes, quantitative predictions for inelastic and non-diffractive ψ production are obtained. These data test the validity of the fundamental assumptions underlying the perturbative approach, determine the values of adjustable parameters present in the models, and discriminate between particular forms of the calculations.

In order to allow comparisons with models that limit their applicability to solely elastic or inelastic processes, the data are divided into two groups, based on the amount of hadronic energy seen in the event. Furthermore, for the purposes of isolating a clear data sample whose interpretation in terms of hard QCD processes would be unaffected by either elastic-inelastic sample mixing due to electromagnetic, ψ' to ψ decay, or calorimeter resolution effects, we consider separately inelastic events with $z < 0.7$.

We have found that the total cross section for muoproducing $\psi(3097)$ at 209 GeV is 0.64 ± 0.10 nb. The portions ascribed to elastic and inelastic production processes are 0.36 ± 0.07 nb and 0.28 ± 0.06 nb, respectively. The muoproduction cross section for inelastic events with $z < 0.7$ is 0.14 ± 0.02 nb and that for events with $z > 0.7$ is 0.14 ± 0.03 nb.

In the γGF model the elastic result can be used to fix the fraction of $c\bar{c}$ states with $m_{c\bar{c}} < 2m_D$ that appear as $\psi(3097)$. When α_S is chosen as $\alpha_S(Q^2 = m_\psi^2, \Lambda = 0.5/GeV) = 0.41$, $f(c\bar{c} \rightarrow \psi) =$

1/8 leads to $\sigma_{elastic}(\gamma\mathrm{GF}) = 0.35$ nb.

While the γGF calculation which leads to the above prediction makes no estimate of the size of "true" inelastic cross section, it does imply a certain contribution to $\sigma_{inelastic}(z > 0.7)$ due to ψ' and χ production. By itself, the "semi-local duality" assumption in the model leads us to expect that all $c\bar{c}$ bound states with $m_{c\bar{c}} < 2m_D$ will be produced with equal probabilities independent of particle spin-parity considerations. Were this true, the measured cross section would satisfy

$$\sigma_{inelastic}(z > 0.7) + \sigma_{elastic} \geq \sigma_{\gamma\mathrm{GF}} = \sum_{i=\psi,\psi',\chi} \sigma_i B_{i\to\psi X} \simeq 0.70 \text{ nb},$$

since the sum of ψ' and χ branching ratios to ψ is 1.03. The measured number is 0.50 ± 0.08 nb, 2.5 sigma from the expectation. This fact must call into question the duality concept, and therefore the entire γGF ψ production normalization procedure.

The photon cross section corresponding to the the $z < 0.7$ region is approximately 6 times that expected from second order perturbation theory calculations that limit themselves to $\gamma g \to \psi g$ subprocesses and require the $c\bar{c}$ system to form a color singlet. Similar calculations that include $\gamma q \to \psi q$ contributions and, more importantly (in terms of overall normalization), allow for $c\bar{c}$ quantum number rearrangement through (uncalculated) soft gluon emission, are in much better agreement with the magnitude of the measured cross section, if the same fraction $f(c\bar{c} \to \psi)$ set by the elastic data is also applied to resolve the inherent normalization uncertainty of this method.

The poor resolution of the spectrometer for $|t|<0.5$ (GeV/c)^2 limits our independent measurement of the size of the coherent production component to $24^{+29}_{-16}\%$ and completely prevents us from measuring the coherent t slope, b_C. Our value is consistent with optical model expectations, assuming A_{eff}/A=0.85 and $b_C = 150$ (GeV/c)$^{-2}$. When fits to the data are constrained to this optical model we find that $30 \pm 3(stat.) \pm 2(syst.)\%$ of the observed signal is due to coherent production, which, once acceptance effects are removed, translates into a 22% coherent contribution to the total elastic cross section.

Once the coherent part has been subtracted from the data, the remaining incoherent data are

well fit by the sum of two exponentials,

$$(d\sigma/dt)_{inc} = 49.5 \text{ nb}/(\text{ GeV}/c)^2[0.82e^{4.25t} + 0.18e^{0.93t}].$$

The average incoherent slope parameter is $(b_I)_{eff} = 2.56^{+0.35}_{-0.32}(stat.)^{+0.21}_{-0.17}(syst.)$. There is a 20% normalization uncertainity associated with $d\sigma/dt\,|_{t=0}$.

These results are consistent with ψ photoproduction data[28–31] and with another ψ muoproduction experiment[95]. Table VI.1 summarizes these results. By way of comparison, we note that the average incoherent slope parameter for ρ muoproduction[35] is $b = 6.4 \pm 0.8$ ($E_\mu = 147$ GeV) and for φ electroproduction[36] ($E_{\gamma v} = 2$ GeV) is $b = 3.4 \pm 0.2$ (GeV/c)$^{-2}$. This experiment does not attempt to measure changes in the t distribution as a function of Q^2, a measure of photon "shrinkage", a common practice in the light meson production experiments. For reference, the average value of Q^2 and ν for these elastic data are 0.71 (GeV/c)^2 and 93.2 GeV, respectively.

Vector dominance makes no definitive statement on the shape of the t distribution for a given vector meson, although the concept of diffractive production is implicitly assumed in the model. However, the relationship between the forward scattering amplitudes for $\gamma_V N \to \psi N$and $\psi N \to \psi N$ prescribed by VMD is used with the optical theorem to generate a relation (Eq. I.4) between $\sigma_{tot}(\psi N)$ and $d\sigma/dt(\gamma N \to \psi N)\,|_{t=t_{min}}$. Approximating $\beta = 0$, $bt_{min} = 0$, and $\Gamma(\psi \to \mu^+\mu^-) =$ 4.3 keV we can use $d\sigma/dt\,|_{t=0}$ and Eq. I.4 to find $\sigma_{tot}(\psi N) = 1.30 \pm 0.26$ mb. This excercise was commonly performed in the first ψ photoproduction experiments with similar results, to provide evidence of the hadronic nature of the ψ.

Finally, the VMD model can be used to make a statement[96] about the expected ratio of elastic to inelastic charm production. Eq. I.5, the value of $(b_I)_{eff}$, and the above result for σ_{tot} can be used to calculate

$$\frac{\sigma_{el}}{\sigma_{tot}}(\psi N) = \frac{\sigma_{tot}}{16\pi b_I} = 0.0260 = \frac{1}{38.5},$$

thus suggesting that inelastic channels comprise a significant fraction of ψN collisions. Vector-

dominance ideas would then imply

$$\sigma(\gamma N \to c\bar{c} + anything) \simeq \frac{\sigma_{tot}(\psi N)}{\sigma_{el}(\psi N)} \sigma_{el}(\gamma N \to \psi N),$$

where c and $\bar{c}$ are here used as generic names for particles carrying the charm quantum number. Thus, in VMD, we expect the ratio of the inelastic charm photoproduction cross section to the cross section for elastically producing ψ's to be $\approx$ 40. We have previously reported[97] the cross section for diffractively producing open charm as $\sigma_{diff}(\mu N \to c\bar{c}X) = 6.9^{+1.9}_{-1.4}$nb (or $\sigma_{diff}(\gamma N \to c\bar{c}X) = 560^{+200}_{-120}$nb at $\nu = 100$ GeV and 750^{+180}_{-130}nb at $\nu = 178$ GeV). The cross section is labeled diffractive because the data are insensitive to charm production mechanisms where the $c\bar{c}$ pair does not carry off most of the laboratory energy of the virtual photon. Augmenting this number by the cross section for inelastic ψ production, $\sigma_{inel}(\mu N \to \psi X) = 0.28$ nb, we find the ratio

$$\left(\frac{\sigma_{inelastic}}{\sigma_{elastic}}\right)_{diff} = \frac{6.9 + 0.28}{0.36} = \frac{7.2}{0.36} = 20,$$

approximately a factor of 2 smaller than the vector dominance prediction if, as suggested by VMD itself, all charm photoproduction is diffractive. The above result might suggest that non-diffractive processes account for a significant fraction of the total charm photoproduction cross section.

In the simplest γGF models $t = p^2_{gluon} \equiv 0$. Arguments[39] involving the color bleaching of the $c\bar{c}$ system by the second soft gluon and the breakdown of the parton model approximation at vanishingly small Q^2 lead to an expectation that the t distribution will be smeared, but will remain sharply peaked toward $t = 0$. In a more general version[98] of γGF an intrinsic transverse momentum distribution $f(k_\perp)$ of gluons in the nucleon is allowed. This momentum allows for the definition of a $\gamma_V \psi$ scattering plane and leads to the prediction of an azimuthal (with respect to the beam muon scattering plane) dependence in ψ production. In this case, $f(k_\perp)$ is measured by the t distribution of diffractive ψ production. This analysis has not been carried out.

The polar and azimuthal angle distributions of muoproduced $\psi \to \mu^+\mu^-$ demonstrate that in the reaction $\gamma_V N \to \psi N$ the ψ's helicity is related to that of the incident γ_V in a manner consistent

with s-channel helicity conservation (SCHC) and natural parity exchange. This same behavior is seen in the leptoproduction of the lower mass vector meons. When we assume $R = \xi^2 Q^2/m_\psi^2$, ξ^2 has a fit value of $4.0^{+4.8}_{-3.4}$. This can be compared with the value of $\xi^2 = 0.5$ observed[35] in ρ muoproduction. When R is fit to a constant value we find $R = 0.37^{+0.27}_{-0.22}$, a 1.5 σ deviation from $R = 0$.

The azimuthal angle data clearly rule out a flat angular distribution. In the standard γGF model for ψ production there is no obvious correlation between virtual photon helicity and ψ helicity[49], due to the required exchange of a second color-conserving gluon that is ignored in the calculations. The longititudinal and transverse cross sections, σ_L and σ_T, are, however, calculated for different assignments of gluon J^P. For $J^P = 1^-$ $(1^+, 0^-)$ these yield $R \simeq 0.02$ (0.4,0.2) at values of $Q^2 \approx 1$ $(\mathrm{GeV}/c)^2$ typical of our data. Our results are not precise enough to decide among these possibilities.

The question of helicity conservation in ψ photoproduction for the general case of two-gluon exchange has been addressed[99] independently of γGF by B. Humpert and A.C.D. Wright. Their conclusion is that, for s sufficiently above ψ threshold, as in this experiment, any choice of gluon mass and spin-parity results in a prediction of SCHC. (i.e.$\rho^0_{00} = 0$, see Appendix A). Furthermore, for vector gluon exchange, helicity is conserved almost exactly even in the ψ-threshold region. In general SCHC is violated in the ψ-threshold region at various levels, depending on the phenomenological model chosen. This experiment clearly adds support to these ideas.

The Q^2 dependence of the effective cross section for elastic ψ photoproduction is well described by a propagator shape, $P(\Lambda) = (1 + Q^2/\Lambda^2)^{-2}$. When one chooses to parameterize the $\psi \to \mu^+\mu^-$ angular distribution in the form prescribed by the SCHC and NPE assumptions, choosing $R = \sigma_L/\sigma_T \propto Q^2$ and ignoring any Q^2 dependence in the nuclear shadowing factor $S(x')$ yields $\Lambda = 2.18^{+0.18}_{-0.13}$ GeV/c^2. If instead we assume R= constant, we find $\Lambda = 2.43 \pm 0.15$ GeV/c^2. Including a shadowing factor which rises from 0.7 to unity with increasing Q^2, in the manner described in Sec. III.6.2, causes the fit value of Λ to drop by 0.2 GeV/c^2.

The highest value of Λ found remains 4 statistical standard deviations from $\Lambda = 3.1$, the VMD

expectation which has adequately described the Q^2 dependence of the lighter mass vector mesons. Since m_ψ^2 is on the order of 10 times that of the mesons for which the VMD model was originally postulated, this may not be too surprising. However the γGF model also predicts that the Q^2 dependence of the effective cross section will be approximately propagator-like, with Λ essentially determined by the mass of the charmed quark used in the calculation. Fits of the model to the data with m_c as an adjustable parameter indicate that the best fit m_c is typically equal to half the best fit value of Λ. For example, we find $m_c = 1.10 \pm 0.08$ GeV/c^2 when we fit the data which yields $\Lambda =$ 2.18 GeV/c^2. The increased phase space available with low m_c causes the γGF calculation for the muoproduction cross section to rise dramatically. Using $m_c = 1.10$ GeV/c^2 results in a prediction for σ that is 9 times the observed value, if $f_{c\bar{c}\to\psi}$ and α_s are kept at 1/8 and 0.41, respectively. Introducing additional Q^2 dependence by evaluating α_S at $m_{c\bar{c}}^2 + Q^2$, rather than at $m_{c\bar{c}}^2$, has no effect on these conclusions. Neither can the form of the gluon fractional momentum distribution $G(x)$, through the power of $1 - x$ in its parameterization, alleviate the discrepancy.

Examination of $\sigma_{eff}(\nu)$ in different Q^2 regions indicates that the two variables are essentially uncoupled in the kinematic range covered by these data. The elastic cross section is still slowly rising with E_γ at $E_\gamma = 170$ GeV and can be parameterized by the form $\sigma_{eff}(\nu) = 20.5-$ nb $\log_{10}(\nu/11.5-$ GeV). The form of $G(x)$ determines the ν dependence of the γGF calculation. Fits of the model to $\sigma_{eff}(\nu, Q^2 = 0)$ indicate that when $xG(x) = 0.5(\eta+1)(1-x)^\eta$, excellent agreement results; we find $\eta = 5.3 \pm 0.4$, consistent with the value $\eta = 5$ arrived at through dimensional arguments. If γGF can resolve the Q^2 discrepancy, $\sigma_{eff}(\nu)$ measured in this experiment provides a model dependent determination of $G(x)$ at $Q^2 \simeq 10($ GeV/$c)^2$.

Results for the inelastic ψ sample, as determined by a cut in the energy observed in the calorimeter, have been presented separately for data in the elasticity regions $z < 0.7$ and $0.7 < z <$ 0.9, in order to lessen possible ambiguity in subsequent interpretations. The elasticity distribution itself, $d^2\sigma_{eff}/dz dp_\perp^2$ rises approximately linearly with $z = E_\psi/E_\gamma$ and is adequately described in $z < 0.9$ by the result of a QCD calculation[55] of the second order process $\gamma g \to \psi g$. It is surprising

that the data do not lie above this prediction when $z > 0.7$, where both simple VMD and γGF predictions for elastic ψ' production indicate that ψ events coming from ψ' decay should augment the signal from purely inelastic processes.

In fact it is generally true that the measured differential cross section in any variable does not vary dramatically for events in the two elasticity regions. Both the overall dependence and what little variation is observed is adequately described by the $\gamma g \rightarrow \psi g$ calculation. For example, the variation of $d^2\sigma_{eff}/dzdp_\perp^2$ with $p_\perp^2$ can be parameterized by the sum of two exponential terms in $p_\perp^2$, with average slope parameters of $1.02 \pm 0.25(\text{ GeV}/c)^{-2}$ and $1.54 \pm 0.11(\text{ GeV}/c)^{-2}$ for the low and high z regions, respectively. The $\gamma g \rightarrow \psi g$ calculation predicts both the changing slope of the differential cross section and the correct average slope in each z region.

The observed Q^2 dependence of the effective cross section for the inelastic $\gamma_V N \rightarrow \psi X$ process is also described by the propagator form $P(\text{A})$. Parameterizing the $\psi \rightarrow \mu^+\mu^-$ angular distribution in the SCHC, NPE form with $R = 0$, and ignoring nuclear shadowing, we find that $\text{A} = 3.10 \pm 0.37$ GeV/c^2 for events with $z < 0.7$, and $\text{A} = 2.61 \pm 0.20$ GeV/c^2 for events with $0.7 < z < 0.9$. When data from these two z regions are combined we measure $\text{A} = 2.98 \pm 0.21$ GeV/c^2. This last result is 4σ larger than the propagator mass found by the European Muon Collaboration (EMC), $\text{A} = 1.8 \pm 0.2$ GeV/c^2, whose inelastic ψ data span all z and are defined by a 5 GeV calorimeter energy cut. Since Q^2 is largely kinematically uncoupled from elasticity, it is unlikely that the Q^2 dependence for $z < 0.9$ can resolve the discrepancy between the two experiments. The data from this experiment are consistent with both the $\gamma_V g \rightarrow \psi g$ prediction[56] and with a calculation[58] which includes the contributions from $\gamma q \rightarrow \psi q$ diagrams. The inelastic events cannot arise from purely non-diffractive processes, for which a propagator mass $\text{A} \sim m_\rho$ is expected[53].

The variation of $\sigma_{eff}(\gamma_V N \rightarrow \psi X(\text{inelastic}))$ with E_γ is found to be consistent with that of elastic ψ production, similar in the two elasticity regions examined, and described adequately by the $\gamma g \rightarrow \psi g$ calculation. This may be attributed to the dominance of γg diagrams in both elastic and inelastic processes, with $\sigma(\nu)$ determined for each by the form of $G(x)$. The E_γ dependence of the

combined $z < 0.9$ data has been compared to that measured by the EMC (all z), and are found to rise less steeply with photon energy. This, however, is a discrepancy which may be caused by the different z regions considered. When the models which include $\gamma q \rightarrow \psi q$ diagrams incorporate the $E_{had} > 5$ GeV cut of the EMC, the calculations agree well with the EMC result.

In conclusion , we find that the first order QCD perturbation calculation, photon-gluon fusion, describes elastic ψ production in all respects except for its Q^2 dependence. Inelastic ψ production is adequately handled by expanding the calculations to second order where final state gluons provide the observed energy. Limiting the $c\bar{c}$ pairs thus produced to those in color singlet, $J^P = 1^-$ states, however, results in predictions for the cross section far below the measured value.

APPENDIX A

The Angular Distribution of Di-leptons in the Decay of Leptoproduced Vector Mesons

A formalism, now in standard use, in which to analyze the photoproduction and leptoproduction of vector mesons has been presented in References 33 and 32, respectively. In these works the spin dependence of the production is described in terms of the spin space density matrix of the vector meson. By expressing the decay angular distribution, W, of the vector meson in terms of these matrix elements, measurements of W can be used to study the production amplitudes. However, since these papers were written before the discovery of charm, the specific decay mode considered was $V \rightarrow$ two pseudoscalar mesons, as in $\rho \rightarrow \pi^+\pi^-$. More recently, Humpert and Wright have considered [99,100] the analagous problem for ψ *photo*production through the $\psi \rightarrow e^+e^-, \mu^+\mu^-$ decay modes. This section fills the currently existing gap by using the results of these authors to find the angular distribution of $\psi \rightarrow \mu^+\mu^-$ in terms of the density matrix elements for leptoproduced ψ's.

A.1 Kinematics

The kinematics are those depicted in Figure I.1, where the 4-momenta of the incoming and outgoing leptons, the initial and final state nucleons, and the exchanged virtual photon and produced vector meson are l_1, l_2, n_1, n_2, q, and v, respectively. The vector meson production is analyzed in the hadronic center of mass system defined by

$$\mathbf{Z} = \frac{\mathbf{q}^*}{|\mathbf{q}^*|}, \qquad \mathbf{Y} = \frac{\mathbf{q}^* \times \mathbf{v}^*}{|\mathbf{q}^* \times \mathbf{v}^*|}, \quad \mathbf{X} = \mathbf{Y} \times \mathbf{Z}.$$

The angle Φ is defined as the angle between the normals to the lepton scattering plane,

$$\mathbf{e}_l = \frac{\mathbf{l}_1^* \times \mathbf{l}_2^*}{|\mathbf{l}_1^* \times \mathbf{l}_2^*|},$$

and the hadron production plane Y:

$$\cos\Phi = \mathbf{e}_l \cdot \mathbf{Y}, \qquad sign(\sin\Phi) = \frac{(\mathbf{Y} \times \mathbf{e}_l) \cdot \mathbf{Z}}{|\mathbf{Y} \times \mathbf{e}_l|}.$$

The decay distribution of the vector meson is described in the vector meson rest frame with the z axis as the direction of flight of the vector meson in the hadronic c.m.s.

$$\mathbf{z} = -\frac{\mathbf{n}_2^*}{|\mathbf{n}_2^*|}, \qquad \mathbf{y} = \mathbf{Y}, \qquad \mathbf{x} = \mathbf{y} \times \mathbf{z}.$$

If $\mathbf{u}$ is the unit vector of the μ^+ in the ψ rest frame, the decay angles are

$$\cos\theta = \mathbf{u} \cdot \mathbf{z}, \qquad \cos\phi = \frac{\mathbf{y} \cdot (\mathbf{z} \times \mathbf{u})}{|\mathbf{z} \times \mathbf{u}|}, \qquad \sin\phi = -\frac{\mathbf{x} \cdot (\mathbf{z} \times \mathbf{u})}{|\mathbf{z} \times \mathbf{u}|}.$$

See Figure I.3 for a graphical representation of these angles. Note that in this figure, and in the main text, we use the variable names $\phi \equiv \phi_2 - \phi_1$, while in this appendix, after the notation of Reference 32, we identify, $\psi = \phi - \Phi$.

A.2 General decay angular distribution of $\psi \to \mu^+\mu^-, e^+e^-$

The polarization states of the photon and the ψ are represented by their hermitian spin space density matrices, $\rho(\gamma)$ and $\rho(\psi)$. These are related by the production amplitudes T

$$\rho(\psi) = \frac{1}{2}T\rho(\gamma)T^\dagger.$$

In the helicity coordinate system described above, the angular distribution of the decay is given by

$$\begin{aligned}\frac{dN}{d\cos\theta d\phi} \equiv W(\cos\theta,\phi) &= M\rho(\psi)M^\dagger \\ &= \sum_{\lambda_V\lambda_{V'}}\sum_{\lambda_+\lambda_-}\langle\lambda_+\lambda_-|M|\lambda_V\rangle\rho_{\lambda_V\lambda_{V'}}\langle\lambda_{V'}|M^\dagger|\lambda_+\lambda_-\rangle,\end{aligned}$$

where M is the decay amplitude, $\lambda_{+,-} = (\pm\frac{1}{2})$ represent lepton helicities, and $\lambda_{V,V'} =(-1,0,1)$ represent ψ helicities. The decay matrix elements are given by

$$\langle\lambda_+,\lambda_-,\theta,\phi|M|\lambda_V\rangle = c_\alpha D^1_{\lambda_V\alpha}(\phi,\theta,-\phi),$$

where $\alpha = \lambda_+ - \lambda_-$. The Wigner rotation functions[101] $D(\phi,\theta,-\phi)$ and the hermiticity of $\rho(\psi)$ can then be used to show

$$\begin{aligned}W(\theta,\phi) = \frac{3}{4\pi}|c_1|^2\Big(&\frac{1}{2}(1+\cos^2\theta) + 2\alpha\sin^2\theta(\rho_{11}+\rho_{-1-1}) + \frac{1}{2}(2\sin^2\theta + 4\alpha\cos^2\theta)\rho_{00} \\ &+ \frac{1}{\sqrt{2}}(Re\rho_{10} - Re\rho_{-10})\sin 2\theta\cos\phi(1-2\alpha) \\ &- \frac{1}{\sqrt{2}}(Im\rho_{10} - Im\rho_{-10})\sin 2\theta\sin\phi(1-2\alpha) \\ &+ Re\rho_{1-1}\sin^2\theta\cos 2\phi(1-2\alpha) - Im\rho_{1-1}\sin^2\theta\sin 2\phi(1-2\alpha)\Big),\end{aligned}$$

where $|c_1|^2 = |c_{-1}|^2$ by rotation invariance and $\alpha \equiv |c_0|^2/|c_1|^2$. If $\psi \to l^+l^-$ proceeds through a photon, $\alpha = 0$; we assume this to be the case and henceforth drop these terms. Note that the sum of all terms that appear above multiplied by 2α are just those constituting the decay angular distribution for $V \to 2$ pseudoscalar mesons.

In order to make the spin content of $\rho(\psi)$ explicit, it is decomposed into a basis spanned by an othoganal set of hermitian 3x3 matrices, Σ^α (Ref. 32, Eq.64) related to the photon's polarization.

$$\rho(V) = \sum_{\alpha=0}^{8} \Pi_\alpha \rho^\alpha,$$

where,

$$\rho^\alpha_{\lambda_V \lambda_{V'}} = \frac{1}{2N_\alpha} \sum_{\lambda_N \lambda_\gamma \lambda_{N'} \lambda_{\gamma'}} T_{\lambda_V \lambda_{N'}, \lambda_\gamma \lambda_N} \Sigma^\alpha_{\lambda_\gamma \lambda_{\gamma'}} T^*_{\lambda_{V'} \lambda_N, \lambda_{\gamma'} \lambda_{N'}}.$$

Here the λ's denote the helicities of the respective particles in the reaction $\gamma_V N \to \psi N'$ and N_α is a normalization factor. The matrices Σ^0 and $\Sigma^{1,2,3}$ describe transverse photons and correspond to the unit matrix and the three Pauli spin matrices σ in the photoproduction case: Σ^0 gives the unpolarized part, Σ^1 and Σ^2 represent linear polarization, and Σ^3 represents circular polarization. The matrix Σ^4 describes longitudinal photons and $\Sigma^5 - \Sigma^8$ represent transverse/longitudinal interference terms.

The components of Π measure the degree of polarization of the virtual photon in terms of these basis states. We have

$$\begin{aligned}\Pi = \frac{1}{1+(\epsilon+\delta)R}\Big(&1, \quad -\epsilon\cos 2\Phi, \quad -\epsilon\sin 2\Phi, \quad \frac{2m}{Q}(1-\epsilon)P_0, \quad (\epsilon+\delta)R, \\ &\sqrt{2\epsilon R(1+\epsilon+2\delta)}\cos\Phi, \quad \sqrt{2\epsilon R(1+\epsilon+2\delta)}\sin\Phi, \\ &\frac{2m}{Q}(1-\epsilon)\sqrt{R}(P_1\cos\Phi + P_2\sin\Phi), \\ &\frac{2m}{Q}(1-\epsilon)\sqrt{R}(P_1\sin\Phi - P_2\cos\Phi)\Big),\end{aligned}$$

where

$$R = \sigma_L/\sigma_T, \qquad \epsilon+\delta = \Gamma_L/\Gamma_T, \qquad \delta = \frac{2m_\mu^2}{Q^2}(1-\epsilon),$$

$$\epsilon = \left(1 + 2\frac{(Q^2+\nu^2)\tan^2\theta_V/2}{Q^2(1-Q^2_{min}/Q^2)^2}\right)^{-1},$$

and the P_i are the components of the incident lepton's polarization in the Breit system.

Symmetry properties of the ρ^α, along with their hermiticity, reduce the number of independent matrix elements in ρ^α and divide the ρ^α into two groups: α=0, 1, 4, 5, 8 and α= 2, 3, 6, 7. These

are listed in Reference 32, Table B, where we note, however, an error in the signs of the imaginary parts of the elements lying below the diagonal of the upper matrix.

The angular distribution is then written as

$$W(\theta,\phi) = \sum_{\alpha=0}^{8} \Pi_\alpha W^\alpha(\theta,\phi),$$

where the W^α are obtained from W by replacing the ρ_{ij} with ρ^α_{ij}. Using the simplified ρ^α and the trace condition $Tr\rho^0 = Tr\rho^4 = 1$ (arising from the identification of $\Pi_0\Sigma^0$ and $\Pi_4\Sigma^4$ with σ_T and σ_L, respectfully) we find, for $\alpha = 0, 4$:

$$W^\alpha(\theta,\phi) = \frac{3}{4\pi}|c_1|^2\left(\frac{1}{2}(1+\rho^\alpha_{00}) + \frac{1}{2}(1-3\rho^\alpha_{00})\cos^2\theta + \sqrt{2}Re\rho^\alpha_{10}\sin 2\theta\cos\phi + \rho^\alpha_{1-1}\sin\theta\cos 2\phi\right);$$

for $\alpha = 1, 5, 8$:

$$W^\alpha(\theta,\phi) = \frac{3}{4\pi}|c_1|^2\left(\rho^\alpha_{11}(1+\cos^2\theta) + \rho^\alpha_{00}\sin^2\theta + \sqrt{2}Re\rho^\alpha_{10}\sin 2\theta\cos\phi + \rho^\alpha_{1-1}\sin^2\theta\cos 2\phi\right);$$

and for $\alpha = 2, 3, 6$, and 7:

$$W^\alpha(\theta,\phi) = \frac{3}{4\pi}|c_1|^2\left(-\sqrt{2}Im\rho^\alpha_{10}\sin 2\theta\sin\phi - Im\rho^\alpha_{1-1}\sin^2\theta\sin 2\phi\right).$$

A.3 General result for unpolarised incident leptons

In this case $P_0 = P_1 = P_2 = 0$ and therefore $\Pi_3 = \Pi_7 = \Pi_8 = 0$. We are left with

$$W^{unpol}(\theta,\phi,\Phi) = \sum_{0,1,2,4,5,6} \Pi_\alpha W^\alpha(\theta,\phi),$$

which leads to

$$
\begin{aligned}
W(\theta,\phi,\Phi) = \frac{1}{1+(\epsilon+\delta)R}\frac{3}{4\pi}|c_1|^2 \times \\
\Bigg(& [\tfrac{1}{2}(1+\rho^0_{00}) + \tfrac{1}{2}(1-3\rho^0_{00})\cos^2\theta + \sqrt{2}Re\rho^0_{10}\sin 2\theta\cos\phi + \rho^0_{1-1}\sin^2\theta\cos 2\phi] \\
& - \epsilon\cos 2\Phi[\rho^1_{11}(1+\cos^2\theta) + \rho^1_{00}\sin^2\theta + \sqrt{2}Re\rho^1_{10}\sin 2\theta\cos\phi + \rho^1_{1-1}\sin^2\theta\cos 2\phi] \\
& - \epsilon\sin 2\Phi[-\sqrt{2}Im\rho^2_{10}\sin 2\theta\sin\phi - Im\rho^2_{1-1}\sin^2\theta\sin 2\phi] \\
& + (\epsilon+\delta)R[\tfrac{1}{2}(1+\rho^4_{00}) + \tfrac{1}{2}(1-3\rho^4_{00}\cos^2\theta + \sqrt{2}Re\rho^4_{00}\sin 2\theta\cos\phi + \rho^4_{1-1}\sin^2\theta\cos 2\phi] \\
& + \sqrt{2\epsilon R(1+\epsilon+2\delta)}\cos\Phi[\rho^5_{11}(1+\cos^2\theta) + \rho^5_{00}\sin^2\theta \\
& \qquad + \sqrt{2}Re\rho^5_{10}\sin 2\theta\cos\phi + \rho^5_{1-1}\sin^2\theta\cos 2\phi] \\
& + \sqrt{2\epsilon R(1+\epsilon+2\delta)}\sin\Phi[-\sqrt{2}Im\rho^6_{10}\sin 2\theta\sin\phi - Im\rho^6_{1-1}\sin^2\theta\sin 2\phi]\Bigg)
\end{aligned}
$$

Note that there are 20 independent quantities affecting the distribution: σ_T, σ_L and 18 ρ^{α}_{ij}'s.

A.4 General result for longitudinally polarized incident leptons

For longitudinally polarized leptons moving in the z direction, the rest frame polarization is

$$P^0_\mu = P(0,0,\pm 1,0),$$

which transforms to the Breit system (BS) as

$$P^{BS}_\mu = (P_1,P_2,P_3,P_0) = P\left(\frac{Q}{2m}\sqrt{\frac{2\epsilon(1+\epsilon+2\delta)}{1-\epsilon^2}},\quad 0,\quad \frac{Q}{2m}\sqrt{\frac{1+\epsilon+2\delta}{1+\epsilon}},\quad \frac{Q}{2m}\sqrt{\frac{1+\epsilon}{1-\epsilon}}\right).$$

This can be used to evaluate $\Pi_{3,7,8}$ to give,

$$W^{\text{long. pol.}}(\theta,\phi,\Phi) = \frac{\pm P}{1+(\epsilon+\delta)R}\frac{3}{4\pi} \times$$
$$\Bigg(\sqrt{1-\epsilon^2}(-\sqrt{2}Im\rho^3_{10}\sin 2\theta \sin\phi - Im\rho^3_{1-1}\sin^2\theta\sin 2\phi)$$
$$+\sqrt{2\epsilon(1-\epsilon)(1+\frac{2\delta}{1+\epsilon})R}\cos\Phi(-\sqrt{2}Im\rho^7_{10}\sin 2\theta\sin\phi - Im\rho^7_{1-1}\sin^2\theta\sin 2\phi)$$
$$+\sqrt{2\epsilon(1-\epsilon)(1+\frac{2\delta}{1+\epsilon})R}\sin\Phi(\rho^8_{11}(1+\cos^2\theta)+\rho^8_{00}\sin^2\theta$$
$$+\sqrt{2}Re\rho^8_{10}\sin 2\theta\cos\phi + \rho^8_{1-1}\sin^2\theta\cos 2\phi)\Bigg).$$

This term introduces 8 additional independent quantities.

A.5 The decay angular distribution in the case of natural parity exchange and s-channel helicity conservation

If $\gamma_V N \to VN$ via t −channel exchange of a particle system with natural ($P = (-1)^J$) or unnatural ($P = -(-1)^J$) parity, there exists a further symmetry property of the helicity amplitudes T under interchange of V and γ helicites indices. These are such that if

$$T \equiv T^N + T^U,$$

we can define

$$\rho^\alpha = \rho^{\alpha N} + \rho^{\alpha U},$$

where,

$$\rho^{\alpha\binom{N}{U}} = \frac{1}{2N_\alpha}T^{\binom{N}{U}}\Sigma^\alpha T^{\binom{N}{U}^*},$$

with no interference terms between T^N and T^U. The above equation, the symmetry property of $T^{\binom{N}{U}}$ refered to above, the parity symmetry of the helicity amplitudes, and a further property of the Σ^α matrices that relates different Σ^α and Σ^β can be used to express $\rho^{\alpha\binom{N}{U}}$ in terms of ρ^α and ρ^β ($\alpha \neq \beta$), thereby reducing the number of independent matrix elements once N or U exchange is specified.

If helicities are conserved in the hadronic c.m.s. (SCHC),

$$T_{\lambda_V\lambda_{N'},\lambda_\gamma\lambda_N} = T_{\lambda_V\lambda_{N'},\lambda_\gamma\lambda_N}\delta_{\lambda_V\lambda_\gamma}\delta_{\lambda_{N'}\lambda_N},$$

the $3\times 2\times 3\times 2 = 36$ original complex amplitudes are reduced in number to six. Parity conservation symmetry reduces these by an additional factor of two, leaving 3 independent amplitudes. The assumption of natural parity exchange leaves us with only two, which are chosen to be $T_{1\frac{1}{2}1\frac{1}{2}}$ and $T_{0\frac{1}{2}0\frac{1}{2}}$. Their relative phase is defined as δ,

$$T_{0\frac{1}{2}0\frac{1}{2}}T^*_{1\frac{1}{2}1\frac{1}{2}} \equiv |T_{0\frac{1}{2}0\frac{1}{2}}||T_{1\frac{1}{2}1\frac{1}{2}}|e^{-i\delta}.$$

These conditions can be used to find that

$$\rho^\alpha = \frac{1}{2}\Sigma^\alpha \qquad (\alpha = 0,1,2,3,4) \qquad \text{and}$$
$$\rho^\alpha = \frac{1}{2}e^{i\delta}\Sigma^\alpha \qquad (\alpha = 5-8).$$

Evaluating the angular distribution then results in

$$W^{\text{unpol}}(\theta,\phi,\Phi) = \frac{1}{1+(\epsilon+\delta)R}\frac{3}{8\pi}|c_1|^2\Big((1+\cos^2\theta) - \epsilon\sin^2\theta(\cos 2\Phi\cos 2\phi + \sin 2\Phi\sin 2\phi)$$
$$+ 2(\epsilon+\delta)R\sin^2\theta + \sqrt{2\epsilon R(1+\epsilon+2\delta)}\sin 2\theta\cos\delta(\cos\Phi\cos\phi + \sin\Phi\sin\phi)\Big),$$

or finally,

$$W^{\text{unpol}}(\theta,\phi,\Phi) = \frac{1}{1+(\epsilon+\delta)R}\frac{3}{8\pi}|c_1|^2\Big((1+\cos^2\theta) - \epsilon\sin^2\theta\cos 2\psi + 2(\epsilon+\delta)R\sin^2\theta$$
$$+ \sqrt{2\epsilon R(1+\epsilon+2\delta)}\sin 2\theta\cos\delta\cos\psi\Big),$$

where $\psi \equiv \phi - \Phi$.

By comparison we can write down the polarization dependent term

$$W^{\text{pol}}(\theta,\phi,\Phi) = \frac{\pm P}{1+(\epsilon+\delta)R}\frac{3}{8\pi}|c_1|^2\sqrt{2\epsilon R(1-\epsilon)(1+\frac{2\delta}{1+\epsilon})}\sin\delta\sin 2\theta\sin\psi.$$

In the limit $Q^2 \gg m_\mu^2$, we have ($|c_1|^2 = \frac{1}{2}$ for normalization) the final result:

$$W(\theta,\phi,\Phi) = \frac{1}{1+\epsilon R}\frac{3}{16\pi}\Big((1+\cos^2\theta) - \epsilon\sin^2\theta\cos 2\psi + 2\epsilon R\sin^2\theta$$
$$+ \sqrt{2\epsilon R(1+\epsilon)}\sin 2\theta\cos\delta\cos\psi - P\sqrt{2\epsilon R(1-\epsilon)}\sin 2\theta\sin\delta\sin\psi\Big).$$

The $(1+\cos^2\theta)$ term is related to transverse ψ production, while the $2\epsilon R\sin^2\theta$ is related to longitudinal ψ production. The $\cos 2\psi$ term arises from linearly polarized transverse photons while the $\sin 2\theta$ terms result from interference between transverse and longitudinal helicity amplitudes.

We note here what form W takes when the SCHC assumption is *not* made and W averaged over azimuthal angles:

$$W(\theta) = \frac{1}{1+\epsilon R}\frac{3}{16\pi}\Big((1+\cos^2\theta)(1-\rho^0_{00}) + 2\sin^2\theta\rho^0_{00} + \epsilon R[(1+\cos^2\theta)(1-\rho^4_{00}) + 2\sin^2\theta\rho^4_{00}]\Big).$$

NPE only affects the terms which have averaged to zero. SCHC implies $\rho^0_{00} = 0$ and $\rho^4_{00} = 1$. Clearly, any test of SCHC with virtual photons requires R to be known. Tests of this assumption are therefore best made using real photons by ascribing differences in measured W from $1+\cos^2\theta$ to deviations of ρ^0_{00} from zero.

REFERENCES

1. J.E. Augustin, *et al.*, Phys. Rev. Lett. 33, 1406 (1974).

2. J.J. Aubert, *et al.*, Phys. Rev. Lett. 33, 1404 (1974).

3. S.L. Glashow, J. Iliopoulos, and L. Maiani, Phys. Rev. D 2, 1285 (1970).

4. B.J. Bjorken and S.L. Glashow, Phys. Lett. 11, 255 (1964).

5. M. Gell-Mann, Phys. Rev. 125, 1067 (1962); Phys. Lett. 8, 214 (1964).

6. S.H. Aronsen, *et al.*, Phys. Rev. Lett. 25, 1057 (1970).

7. W.A. Carithers, *et al.*, Phys. Rev. Lett. 31, 1025 (1973).

8. S. Weinberg, Phys. Rev. Lett. 19, 1264 (1967); A. Salam in Elementary Particle Theory, ed. by N. Svartholm (Almquist and Wiksell, Stockholm, 1969), p.367.

9. F.J. Hassert, *et al.*, Phys. Lett. 46*B*, 121 (1973).

10. A. DeRujula and S.L. Glashow, Phys. Rev. Lett. 34, 46 (1975).

11. G. Goldhaber, *et al.*, Phys. Rev. Lett. 37, 255 (1976).

12. I. Peruzzi, *et al.*, Phys. Rev. Lett. 37, 569 (1976).

13. M.K. Gaillard, B.W. Lee, and J.L. Rosner, Rev. Mod. Phys. 47, 277 (1975).

14. A.R. Clark, *et al.*, Phys. Rev. Lett. 43, 187 (1979).

15. P.G.O. Freund, Nuovo Cimento 44*A*, 411 (1966); 48*A*, 541 (1967).

16. J.J. Sakurai, Phys. Rev. Lett. 22, 981 (1969).

17. J.J. Sakurai, in *Proceedings of the Fourth International Symposium on Electron and Photon Interactions at High Energies*, Liverpool, 1969; eds. D.W. Braben and R.E. Rand, pg. 91.

18. T. Appelquist, R.M. Barnett, K. Lane, Ann. Rev. Nucl. Part. Sci. 28, 387 (1978).

19. H.D. Politzer, Phys. Lett. C14, 129 (1974).

20. D. Gross and F. Wilczek, Phys. Rev. D 9, 980 (1974); 9, 3633 (1975).

21. H. Georgi and H.D. Politzer, Phys. Rev. D 9, 416 (1974).

22. D. Balin, A. Love, and D. Nanopoulos, Nuovo Cim. Lett. 9, 501 (1974).

23. T.H Bauer, R.D. Spital, D.R. Yennie, and F.M. Pipkin, Rev. Mod. Phys. 50, 261 (1978).

24. J.J. Sakurai, Ann. Phys. (N.Y.) 11, 1 (1960).

25. M. Gell-Mann and F. Zachariansen, Phys. Rev. D 124, 953 (1961).

26. L.N. Hand, Phys. Rev. 129, 1834 (1963).

27. M. Perl, in *High Energy Hadron Physics*, pub. by John Wiley and Sons, Inc., 1974, p. 24–39.

28. B. Knapp, *et al.*, Phys. Rev. Lett. 34, 1040 (1975); L. Cormell, Ph.D. Thesis, U. of Illinois (1975), unpublished.

29. U. Camerini, *et al.*, Phys. Rev. Lett. 35, 483 (1975).

30. B. Gittelman, *et al.*, Phys. Rev. Lett. 35, 1616 (1975).

31. T. Nash, *et al.*, Phys. Rev. Lett. 36, 1233 (1976).

32. K. Schilling and G. Wolf, Nuc. Phys. B61, 381 (1973).

33. K. Schilling, P. Seyboth, and G. Wolf, Nuc. Phys. B15, 397 (1970).

34. J.T. Dakin, *et al.*, Phys. Rev. Lett. 30, 142 (1973).

35. W.R. Francis, *et al.*, Phys. Rev. Lett. 38, 633 (1977).

36. R. Dixon, *et al.*, Phys. Rev. Lett. 39, 516 (1977).

37. Figure L3 is a modified version of Figure 2 in B. Dieterle, Nuovo Cimento 11*A*, 523 (1972).

38. H. Fritzsch, Phys. Lett. 67*B*, 217 (1977).

39. J.P. Leveille, *Photon-Gluon Fusion: A Review*, based on a talk presented at the Topical Workshop on the Production of New Particles in Super High Energy Collisions, $\sqrt{s} = 10^2 - 10^5$ GeV, Madison, Wisconsin, October 22-24, 1979; Preprint COO-881-120; Published in Madison Workshop, 1979.

40. H. Fritzsch and K.-H. Streng Phys. Lett. 72*B*, 385 (1978).

41. F. Halzen and D.M. Scott, Phys. Lett. 72*B*, 404 (1978).

42. M. Glück and E. Reya, Phys. Lett. 79*B*, 453 (1978); 83*B*, 98 (1979).

43. L.M. Jones and H.W. Wyld, Phys. Rev. D 17, 759 (1978); 17, 1782 (1978); 17, 2332 (1978).

44. J. Babcock, D. Sivers, and S. Wolfram, Phys. Rev. D 18, 162 (1978).

45. C.E. Carlson and R. Suaya, Phys. Rev. D 18, 760 (1978).

46. J.P. Leveille and T. Weiler, Nuc. Phys. *B*147, 147 (1979).

47. V. Barger, W.Y. Keung, and R.J.N. Phillips, Phys. Rev. D 20, 630 (1979).

48. S.J. Brodsky and G.R. Farrar, Phys. Rev. Lett. 31, 1153 (1973).

49. T. Weiler, Phys. Rev. Lett. 44, 304 (1980).

50. V. Barger, W.Y. Keung, and R.J.N. Phillips, Phys. Lett. 91*B*, 253 (1980).

51. D.W. Duke and J.F. Jones, Phys. Rev. Lett. 44, 1173 (1980).

52. R.J.N. Phillips, *Charmed Quark Production as a Gluon Probe*, Invited review talk at Hadron Structure '80, Smolenice, Czechoslavakia, September 22-26, 1980. Preprint RL-80-062.

53. J.P. Leveille and T. Weiler, Phys. Lett. 86*B*, 377 (1979).

54. K.T. Mahanthappa and J. Randa, Phys. Rev. D 23, 696 (1981).

55. E.L. Berger and D. Jones, Phys. Rev. D 23, 1521 (1981).

56. W.Y. Keung, *Inclusive Quarkonium Production*, Talk delivered at the "Z^0 Physics Workshop" at Cornell University, February 1981, BNL-29297-mc (microfiche).

57. D.W. Duke and J.F. Owens, Phys. Lett. 96*B*, 184 (1980).

58. D.W. Duke and J.F. Owens, Phys. Rev. D 23, 1671 (1981).

59. D.W. Duke and J.F. Jones, Phys. Rev. D 24, 1403 (1981).

60. Figure I.4 is from Reference 57, Figure 1.

61. B.A. Gordon, *et al.*,, Phys. Rev. D 20, 2654 (1979).

62. Danby Steel Mills, Chigago, Illinois.

63. D.B. Evans and L.T. Kerth, L.B.L. Kerth Group Internal Notes 65 and 79.

64. See, for example, *Proceedings of the Calorimeter Workshop*, Fermilab, May, 1975, and references therein.

65. G.D. Gollin, *et al.*, Phys. Rev. D 24, 559 (1981), and G.D. Gollin, Ph.D. Thesis, Princeton University, 1980.

66. P.D. Meyers, Ph.D. Thesis, University of California, Berkeley, 1982.

67. W.H. Smith, Ph.D. Thesis, University of California, Berkeley, 1981.

68. G. Gollin, *et al.*,, IEEE Trans. Nuc. Sci. *NS*-26, 59 (1979).

69. A. Bodek, *et al.*,, in Reference 64.

70. J.D. Jackson, *Classical Electrodynamics*, pub. by John Wiley and Sons, 1975, p. 649.

71. L.S. Brown and R.N. Cahn, Phys. Rev. Lett. 35, 1 (1975).

72. L.W. Mo and Y.S. Tsai, Rev. Mod. Phys. 41, 205 (1969).

73. See, for example, A. Silverman, in *Proceedings of the 1975 International Symposium on Lepton and Photon Interactions at High Energies*, p. 355–412, and references therein.

74. W.R. Ditzler, *et al.*, Phys. Lett. 57*B*, 201 (1975).

75. S. Stein, *et al.*, Phys. Rev. D 12, 1884 (1975).

76. J. Eickmeyer, *et al.*, Phys. Rev. Lett. 36, 289 (1976).

77. S. Michalowski, *et al.*, Phys. Rev. Lett. 39, 737 (1977).

78. W.A. Loomis, representing M.S. Goodman, *et al.*, in *Proceedings of the 1980 International Conference on High Energy Physics*, Madison, Wisconsin, July 17–23, 1980, p. 230–232.

79. M.S. Goodman, *et al.*, Phys. Rev. Lett. 47, 293 (1981).

80. F. Bulos, *et al.*, Phys. Rev. Lett. 22, 490 (1969).

81. H.-J. Behrend, *et al.*, Phys. Rev. Lett. 24, 1246 (1970).

82. D.L. Nease, Ph.D. Thesis, Cornell University (1975), unpublished.

83. J.S. Sarracino, Ph.D. Thesis, U. of Illinois (1976), unpublished.

84. M. Binkley, private communication.

85. This section is an expanded version of the results presented in A.R. Clark, *et al.*, Phys.

Rev. Lett. 45, 2092 (1980).

86. Mac Donald Mestayer, Ph.D. Thesis, Stanford U. (1978), SLAC Report No. 214.

87. J.J. Sakurai and D. Schildknecht, Phys. Lett. 40B, 121 (1972).

88. A.R. Clark, *et al.*, Phys. Rev. Lett. 45, 1465 (1980).

89. J.P. Leveille and T. Weiler, in *Proceedings of the 1980 International Conference on High Energy Physics*, Madison, Wisconsin, July 17–23, 1980, p. 263–267.

90. G. Altarelli and G. Parisi, Nuc. Phys. B126, 1977 (298).

91. A.J. Buras and K.J.F. Gaemers, Nuc. Phys. B132, 249 (1978).

92. J.J. Aubert, *et al.*, CERN Preprint EP/80–84 (unpublished); R.P. Mount, representing the European Muon Collaboration, in *Proceedings of the 1980 International Conference on High Energy Physics*, Madison, Wisconsin, July 17–23, 1980, p. 205–211.

93. If the BFP efficiency correction for each ν bin based on the $z < 0.9$ sample is blindly applied to the total inelastic data set, $z < 1.0$, a steeper E_γ dependence is in fact observed. As this is not proper analysis procedure, the fact is only suggestive. Note that if the same test is applied to Q^2, no change from the $z < 0.9$ value of A is observed.

94. In their comparison, they have directly incorporated the cut $E_{cal} > 5$ GeV defining the EMC inelastic sample by demanding that $z < 1 - 5/\nu$. It is claimed that this requirement is partly responsible for the steep rise of $\sigma(\nu)$.

95. J.J. Aubert, *et al.*, Phys. Lett. 89B, 267 (1980).

96. D. Sivers, J. Townsend, and G. West, Phys. Rev. D 13, 1234 (1976).

97. A.R. Clark, *et al.*, Phys. Rev. Lett. 45, 682 (1980).

98. J.P. Leveille and T. Weiler, Azimuthal Dependence of Diffractive ψ and $D\bar{D}$ Electroproduction

and a Test of Gluon Spin, Parity, and $k_{\perp}$, Preprint NUB-2479 and UM HE 80-40.

99. B. Humpert and A.C.D. Wright, Phys. Lett. 65*B*, 463 (1976).

100. B. Humpert and A.C.D. Wright, Ann. Phys. (N.Y.) 110, 1 (1978).

101. See, for example, M.E. Rose, Elementary Theory of Angular Momentum, pub. by John Wiley and Sons, 1957.

Table II.I Average values and rms deviations of parameters specifying MWPC chamber efficiency ϵ. The dependence on radial distance r from the beam centroid is taken as $\epsilon = a - be^{-r/r_0}$, and the average is over chamber number. Results are shown for anode (x) and cathode (y) planes for both μ^+ (flux=2×10^6 muons/sec) and μ^- (flux=0.6×10^6 muons/sec) running.

		MWPC EFFICIENCY			
		μ^+		μ^-	
		mean	σ	mean	σ
x	$a(\%)$	93.4	4.7	94.9	3.5
	$b(\%)$	10.8	5.6	10.7	6.5
	$r_0(cm)$	17.2	11.6	12.2	8.3
y	$a(\%)$	92.0	4.5	94.3	4.2
	$b(\%)$	33.1	13.3	30.5	17.9
	$r_0(cm)$	18.2	11.1	15.6	9.0

Table IV.1. Results of fits to the t dependence of the effective cross section σ_{eff} for the reaction $\gamma_V \mathrm{Fe} \rightarrow \psi X$ (energy (X) < 4.5 GeV). The fit parameters N', a, f, b_1 and b_2 are described in the text. The five reported fits differ in which, if any, of these parameters are constrained. In Fit 1 all parameters are free; a then measures deviations of the data from the optical model or changes in the coherent slope parameter from that used in the Monte Carlo simulation. Fit 2 fixes $N' = 1$, testing sensitivity of the measured parameters to the validity of the analysis procedure. In Fits 3, 4, and 5 a is constrained to values corresponding to various nuclear shadowing factors, A_{eff}/A, within an optical model parametization of $d\sigma/dt$, with $b_C = 150\ (\mathrm{GeV}/c)^{-2}$. Fit 3 is the best estimate of the data; Fits 4 and 5 provide an estimate of the systematic errors in Fit 3 under variation of A_{eff}/A. Also presented for Fits 1 and 3 are the values of the average incoherent slope parameter, $(b_I)_{eff}$, and the fraction of coherent events in the observed data sample, f_C.

	Fit 1	Fit 2	Fit 3	Fit 4	Fit 5
χ^2/DF	0.4/4	1.7/5	0.5/5	0.4/5	0.7/5
N'	$1.10^{+0.14}_{-0.09}$	$\equiv 1.00$	1.06 ± 0.05	1.08 ± 0.05	1.05 ± 0.05
a	$0.62^{+0.98}_{-0.56}$	$1.40^{+0.76}_{-0.51}$	$\equiv 1.00$	$\equiv 0.82$	$\equiv 1.18$
f	$0.85^{+0.07}_{-0.10}$	$0.79^{+0.06}_{-0.09}$	0.82 ± 0.04	0.83 ± 0.04	0.80 ± 0.05
b_1	5.03 ± 1.80	3.46 ± 0.86	$4.25^{+0.76}_{-0.60}$	$4.59^{+0.77}_{-0.62}$	$3.97^{+0.75}_{-0.58}$
b_2	0.96 ± 0.12	0.90 ± 0.13	0.93 ± 0.11	0.94 ± 0.11	0.92 ± 0.11
f_C	$0.24^{+0.29}_{-0.16}$	NA	$0.30 \pm 0.03(stat.) \pm 0.02(syst.)$	NA	NA
$(b_I)_{eff}$	$3.08^{+0.87}_{-1.03}$	NA	$2.56^{+0.35}_{-0.32}(stat.)^{+0.21}_{-0.17}(syst.)$	NA	NA

Table IV.2 The total, coherent, and incoherent cross sections, differential in t, for the reaction $\gamma_V \mathrm{Fe} \rightarrow \psi X$ (energy (X)<4.5 GeV), in nb/(GeV/c)^2. Each entry corresponds to a bin in measured t. The total cross section is corrected point by point by the assumed coherent contribution, as described in the text, to yield the incoherent cross section. The tabulated t is the resolution corrected (true) value corresponding to the incoherent contribution only; for coherent events true $t \simeq 0.01$ (GeV/c)^2, for all bins in measured t. The errors on $(d\sigma/dt)_{coh}$ and $(d\sigma/dt)_{tot}$ are statistical only. Errors in $(d\sigma/dt)_{inc}$ are calculated from those of the total and the coherent cross sections. The incoherent contribution is plotted in Figure IV.1(b); note that the first two data points have been combined in the plot.

t(GeV/c)^2	$d\sigma/dt$ [nb/(GeV/c)^2]		
	TOTAL	COHERENT	INCOHERENT
0.128	73.4 ± 6.4	45.9 ± 2.3	27.5 ± 6.8
0.159	63.7 ± 5.5	33.6 ± 1.9	30.1 ± 5.8
0.199	44.8 ± 2.5	19.4 ± 0.9	25.4 ± 2.7
0.281	29.3 ± 1.9	9.72 ± 0.67	19.5 ± 2.1
0.383	18.3 ± 1.3	4.05 ± 0.45	14.3 ± 1.3
0.546	10.2 ± 0.8	0.92 ± 0.27	9.31 ± 0.80
0.965	4.54 ± 0.32	0.13 ± 0.13	4.41 ± 0.34
1.85	1.67 ± 0.18	0.01 ± 0.09	1.66 ± 0.20
3.74	0.286 ± 0.051	0.002 ± 0.035	0.284 ± 0.062

Table IV.3. Part (a) displays the effective cross section, differential in $\cos\theta$ and ϕ for the reaction $\gamma_V Fe \rightarrow \phi X$ (energy (X) <4.5 GeV), in arbitrary units. Data and statistical errors are given in 60 bins, defined by average Q^2 (top row), average $\cos^2\theta$ (left column), and one of three ϕ bins (second-left column). In parts (b), (c), (d), (e), and (f) the average values of Q^2, $\cos^2\theta$, $\cos 2\phi$, ϵ, and the nuclear shadowing factor $S(x')$ are tabulated in an identical manner.

Table IV.3(a)

$\langle Q^2 \rangle$ (GeV/c)^2		0.10	0.53	1.60	6.34
$\overline{cos^2\theta}$	ϕ bin	$d^2\sigma(eff)/d\phi d cos\theta$ (arbitrary units)			
0.02	1	0.52(07)	0.37(09)	0.30(10)	0.05(07)
	2	0.55(07)	0.61(11)	0.36(11)	0.10(05)
	3	0.59(06)	0.64(13)	0.44(09)	0.35(11)
0.06	1	0.51(06)	0.24(07)	0.36(13)	0.05(04)
	2	0.61(07)	0.68(13)	0.35(10)	0.27(10)
	3	0.50(06)	0.76(14)	0.54(11)	0.22(06)
0.16	1	0.54(07)	0.25(11)	0.22(10)	0.04(05)
	2	0.64(08)	0.52(12)	0.36(11)	0.09(04)
	3	0.52(07)	0.56(11)	0.49(11)	0.11(05)
0.32	1	0.58(08)	0.32(12)	0.36(13)	0.04(06)
	2	0.46(08)	0.47(16)	0.27(09)	0.12(07)
	3	0.62(09)	0.66(14)	0.39(10)	0.11(06)
0.54	1	0.55(28)	0.91(34)	0.31(25)	0.12(10)
	2	0.67(20)	0.15(28)	0.48(22)	0.05(10)
	3	1.09(29)	1.21(48)	0.35(28)	0.12(10)

Table IV.3(b)

$\langle Q^2 \rangle$ (GeV/c)^2		0.10	0.53	1.60	6.34
$\overline{\cos^2\theta}$	ϕ bin	$\langle Q^2 \rangle$ (GeV/c)^2			
	1	0.081	0.511	1.610	6.490
0.02	2	0.097	0.509	1.734	5.480
	3	0.111	0.525	1.528	4.956
	1	0.092	0.567	1.406	7.141
0.06	2	0.105	0.492	1.564	5.327
	3	0.104	0.486	1.489	7.218
	1	0.085	0.487	1.743	5.930
0.16	2	0.102	0.529	1.617	7.893
	3	0.105	0.562	1.717	7.277
	1	0.087	0.556	1.539	5.246
0.32	2	0.122	0.607	1.578	6.183
	3	0.117	0.517	1.601	6.059
	1	0.116	0.494	1.611	7.763
0.54	2	0.123	0.597	1.450	6.867
	3	0.123	0.601	1.829	6.691

Table IV.3(c)

$\langle Q^2 \rangle$ (GeV/c)^2		0.10	0.53	1.60	6.34
$\overline{\cos^2\theta}$	ϕ bin		$\langle \cos^2\theta \rangle$		
0.02	1	0.017	0.014	0.014	0.015
	2	0.015	0.013	0.017	0.012
	3	0.014	0.014	0.014	0.019
0.06	1	0.067	0.067	0.071	0.067
	2	0.065	0.066	0.061	0.061
	3	0.062	0.062	0.058	0.070
0.16	1	0.158	0.158	0.154	0.147
	2	0.152	0.164	0.155	0.152
	3	0.162	0.154	0.152	0.153
0.32	1	0.318	0.332	0.323	0.313
	2	0.319	0.317	0.318	0.326
	3	0.313	0.320	0.335	0.286
0.54	1	0.533	0.524	0.559	0.518
	2	0.525	0.555	0.545	0.561
	3	0.522	0.555	0.554	0.548

Table IV.3(d)

$\langle Q^2 \rangle$ (GeV/c)^2		0.10	0.53	1.60	6.34
$\overline{\cos^2\theta}$	ϕ bin		$\langle \cos 2\phi \rangle$		
	1	-0.191	0.488	0.660	0.801
0.02	2	-0.328	-0.154	-0.106	-0.082
	3	-0.503	-0.704	-0.756	-0.807
	1	-0.110	0.550	0.707	0.810
0.06	2	-0.307	-0.165	-0.084	-0.064
	3	-0.495	-0.724	-0.754	-0.790
	1	-0.073	0.600	0.726	0.784
0.16	2	-0.249	-0.111	-0.117	0.009
	3	-0.422	-0.743	-0.766	-0.823
	1	-0.009	0.547	0.728	0.778
0.32	2	-0.187	-0.094	-0.077	0.022
	3	-0.422	-0.721	-0.716	-0.830
	1	0.129	0.502	0.746	0.786
0.54	2	-0.101	-0.130	-0.094	-0.196
	3	-0.409	-0.692	-0.648	-0.733

Table IV.2(e)

$\langle Q^2 \rangle$ (GeV/c)^2		0.10	0.53	1.60	6.34
$\overline{\cos^2\theta}$	ϕ bin		$\langle\varepsilon\rangle$		
0.02	1	0.820	0.799	0.795	0.851
	2	0.816	0.818	0.830	0.799
	3	0.836	0.801	0.800	0.800
0.06	1	0.825	0.811	0.766	0.789
	2	0.829	0.799	0.774	0.814
	3	0.813	0.804	0.789	0.788
0.16	1	0.792	0.808	0.794	0.781
	2	0.801	0.794	0.790	0.825
	3	0.798	0.795	0.807	0.775
0.32	1	0.774	0.729	0.769	0.701
	2	0.751	0.746	0.778	0.710
	3	0.771	0.748	0.733	0.739
0.54	1	0.614	0.642	0.662	0.587
	2	0.691	0.630	0.618	0.614
	3	0.659	0.666	0.664	0.548

Table IV.3(f)

$\langle Q^2 \rangle$ (GeV/c)^2		0.10	0.53	1.60	6.34
$\overline{\cos^2\theta}$	ϕ bin	<nuclear screening>			
0.02	1	0.744	0.766	0.807	0.906
	2	0.744	0.764	0.810	0.877
	3	0.745	0.764	0.803	0.878
0.06	1	0.744	0.767	0.795	0.902
	2	0.745	0.763	0.803	0.888
	3	0.745	0.764	0.799	0.897
0.16	1	0.743	0.762	0.809	0.876
	2	0.744	0.764	0.803	0.904
	3	0.744	0.763	0.806	0.900
0.32	1	0.743	0.759	0.796	0.869
	2	0.744	0.763	0.797	0.877
	3	0.745	0.760	0.795	0.881
0.54	1	0.743	0.756	0.788	0.879
	2	0.744	0.758	0.781	0.870
	3	0.744	0.758	0.792	0.867

Table IV.A. Fits to the Q^2, ϕ, and θ-dependence of the effective cross section σ_{eff} for the reaction $\gamma_V Fe \rightarrow \psi X$ (energy (X) <4.5 GeV). The angular function $W(\eta,R)$, propagator $P(\Lambda)$, and nuclear shadowing factor $S(x')$ are defined in the text. Each of seven fits (numbered in the first column) is performed both with $S(x')$ included (multiplied "in") and ignored ("out") in the function fitted. Values of chi-squared and the degrees of freedom are given in the fourth column. Errors on the fit parameters A, η, and ξ^2 (fits 1 and 6) or R (fit 2) are statistical. Fit 6 is the same as fit 1 except W is multiplied by $(1+\epsilon R)$; A then parameterizes the Q^2 dependence of σ_T rather than σ_{eff}. Fit 7 compares the data integrated over ϕ and $\cos\theta$ with the Q^2-dependence predicted by γGF.

Fit No.	Function	$S(x')$	χ^2/DF	Λ(GeV/c^2)	η	ξ^2 or R
1	$W(\eta,R)\times P(\Lambda)$, $R=(\xi Q/m_\psi)^2$	in	45.4/56	$2.03^{+0.18}_{-0.12}$	$1.02^{+0.28}_{-0.23}$	$3.3^{+4.9}_{-3.0}$
		out	45.5/56	$2.18^{+0.18}_{-0.13}$	$1.04^{+0.28}_{-0.23}$	$4.0^{+4.8}_{-3.4}$
2	$W(\eta,R)\times P(\Lambda)$, R=constant	in	42.0/56	2.24±0.13	$1.09^{+0.31}_{-0.24}$	$.35^{+.26}_{-.18}$
		out	42.4/56	2.43±0.15	$1.10^{+0.31}_{-0.24}$	$.37^{+.27}_{-.22}$
3	$1\times P(\Lambda)$	in	73.3/58	2.06±0.11		
		out	73.3/58	2.22±0.13		
4	$W(1,0)\times P(\Lambda)$	in	48.6/58	2.21±0.12	≡1	≡0
		out	49.3/58	2.40±0.14		
5	$W(\eta,0)\times P(m_\psi)$	in	89.1/58	≡3.1	0.96±0.13	≡0
		out	68.5/58		0.93±0.14	
6	$(1+\epsilon R)\times$Fit 1	in	47.0/56	2.08±0.24	0.86±0.17	$.24^{+.61}_{-.39}$
		out	47.6/56	2.20±0.29	0.87±0.17	$.34^{+.75}_{-.43}$
7	γGF -- Q^2 projection	in	32.1/8	m_c≡1.5 GeV/c^2		
		out	14.6/8			

XBL 809-11763

Table IV.5 Part (a) tabulates the effective cross section σ_{eff} in nanobarns as a function of E_γ for the diffractive process $\gamma N \to \psi N$. The data for $E_\gamma < 25$ GeV were calculated using the results of a SLAC photoproduction experiment[29], as described in the text. The measurements listed for this experiment are attained by extrapolating σ_{eff} to $Q^2 = 0$ using $P(\Lambda) = (1 + Q^2/\Lambda^2)^{-2}$ with $\Lambda = 2.18$ GeV/c^2. In part (b) σ_{eff} is given in nanobarns for the process $\gamma_V N \to \psi N$ for 16 bins, each labeled by the average value of ν and Q^2 of the bin. The errors listed for both parts (a) and (b) are statistical only. The data are plotted in Figure IV.6 along with the fits summarized in Table IV.6.

(a) $\sigma_{eff}(\gamma N \to \psi N)$

SLAC		This Experiment	
ν(GeV)	σ(nb)	ν(GeV)	σ(nb)
13.0	1.31 ± 0.28	40.1	10.3 ± 0.8
16.0	2.83 ± 0.38	58.0	14.3 ± 0.9
17.0	3.72 ± 0.34	80.3	17.5 ± 0.9
19.0	4.14 ± 0.38	108.	20.7 ± 1.2
21.0	5.03 ± 0.41	140.	23.8 ± 1.6
		173.	24.0 ± 5.0

(b) $\sigma_{eff}(\gamma_V N \to \psi N)$

		Q_1^2	Q_2^2	Q_3^2	Q_4^2
	σ(nb)	11.1 ± 0.7	12.6 ± 1.6	8.17 ± 1.17	2.08 ± 0.61
ν_1	ν(GeV)	48.8	48.4	49.9	51.2
	Q^2(GeV/c)^2	0.076	0.47	1.63	6.12
	σ(nb)	16.5 ± 0.9	17.4 ± 1.8	10.9 ± 1.3	4.20 ± 0.73
ν_2	ν(GeV)	82.0	83.3	82.9	87.9
	Q^2(GeV/c)^2	0.099	0.55	1.66	6.30
	σ(nb)	20.8 ± 1.4	18.9 ± 2.2	9.98 ± 1.56	3.17 ± 0.76
ν_3	ν(GeV)	120.	121.	124.	126.
	Q^2(GeV/c)^2	0.12	0.49	1.64	6.84
	σ(nb)	22.8 ± 3.0	21.6 ± 4.0	20.0 ± 3.9	5.79 ± 1.96
ν_4	ν(GeV)	156.	159.	161.	163.
	Q^2(GeV/c)^2	0.16	0.52	1.54	5.58

Table IV.6 Results of fits to the Q^2 and ν dependence of the effective cross section σ_{eff} for the reaction $\gamma_V N \rightarrow \psi N$. All fits are of the form predicted by the γGF model of ψ muoproduction. They differ in which, if any, of the parameters $f_{c\bar{c}\rightarrow\psi}$, and η are constrained, in the form of α_S, the strong interaction coupling constant, assumed, and in the data included in the fit. Fits 1 and 2 use only data from this experiment from different Q^2 and ν bins (Table IV.5, part (b)). In fit 1 the nominal values of the parameters m_c, η, and α_S are assumed; in fit 2, m_c and η are allowed to vary. Fit 3 is of the same form as fit 2, but includes the $Q^2 = 0$ SLAC data and allows for a relative normalization constant k between the two data sets in the fit. Fit 4 investigates the changes introduced by using $m_{c\bar{c}}^2 + Q^2$ as the point at which α_S is evaluated. Fit 5 (fit 6) fits $\sigma_{eff}(\nu, Q^2 = 0)$ (Table IV.5, part (a)) by fixing m_c at its standard (best fit) value. Fit 5 thus shows the best value of η in the γGF model independent of the Q^2 dependence of the data, while fit 6 indicates how η can change in response to changes in m_c.

Fit	χ^2/DF	$8 \times f_{c\bar{c}\rightarrow\psi}$	m_c(GeV/c^2)	η	k	$arg(\alpha_S)$	DATA
1	40.3/15	0.92 ± 0.03	$\equiv 1.5$	$\equiv 5$	NA	$m_{c\bar{c}}^2$	BFP
2	16.6/13	$0.11^{+0.05}_{-0.03}$	1.10 ± 0.08	9.18 ± 1.23	NA	$m_{c\bar{c}}^2$	BFP
3	20.8/17	$0.11^{+0.04}_{-0.03}$	1.08 ± 0.07	8.58 ± 1.11	1.24 ± 0.16	$m_{c\bar{c}}^2$	BFP,SLAC
4	21.3/17	0.12 ± 0.03	1.10 ± 0.05	7.95 ± 0.94	1.21 ± 0.16	$m_{c\bar{c}}^2 + Q^2$	BFP,SLAC
5	9.7/8	1.01 ± 0.04	$\equiv 1.5$	5.25 ± 0.41	1.23 ± 0.16	$m_{c\bar{c}}^2$	BFP($Q^2 = 0$),SLAC
6	5.4/8	0.12 ± 0.04	$\equiv 1.1$	8.49 ± 0.68	1.27 ± 0.16	$m_{c\bar{c}}^2$	BFP($Q^2 = 0$),SLAC

Table V.1 The $z = E_\psi/E_\gamma$ dependence of inelastic ψ production. Measurements of $d\sigma/dz$ in pb. for the reaction $\mu N \to \mu\psi X$ ($E_X > 4.5$ GeV) are shown in column 4; the effective cross section, differential in z and $p_\perp^2$ for the reaction γ_VFe $\to \psi X$ $E_X > 4.5$ GeV) are shown in column 6 in arbitrary units. Both sets of results have been corrected for elastic event feed-down by the numbers in column 3, labeled $efdc$. The errors for $z < 0.7$ are statistical only; those for $z > 0.7$ have both statistical and systematic (through uncertainty in $efdc$) errors indicated, in that order. The values of Δz used in evaluating $d\sigma/dz$ are listed in column 2. Columns 5 and 7 present $d\sigma/dz$ in pb. and $d^2\sigma_{eff}/dzdp_\perp^2$ in arbitrary units for the MC simulation of ψ' production, with $\psi' \to \psi\pi\pi, \psi\eta$, assuming a ψ' to ψ production ratio of 0.38. These data are plotted in Figure V.1.

			$d\sigma/dz$(pb)		$d^2\sigma_{eff}/dzdp_\perp^2$ (arb. units)	
z	Δz	$efdc$	$\mu N \to \mu\psi X$	$\mu N \to \mu\psi' N$ $\psi' \to \psi X$	$\gamma_V N \to \psi X$	$\gamma_V N \to \psi' N$ $\psi' \to \psi X$
0.28	0.088	0.98	107 ± 56	—	117 ± 61	—
0.37	0.099	0.97	83 ± 21	—	115 ± 30	—
0.47	0.101	0.99	256 ± 36	—	304 ± 42	—
0.57	0.092	0.99	386 ± 37	—	424 ± 41	—
0.66	0.093	0.97	597 ± 44	12 ± 3	597 ± 44	12 ± 3
0.75	0.094	0.91 ± 0.06	$624 \pm 39 \pm 41$	171 ± 10	$641 \pm 40 \pm 42$	175 ± 10
0.85	0.098	0.79 ± 0.13	$644 \pm 40 \pm 107$	363 ± 14	$683 \pm 42 \pm 113$	386 ± 15
0.93	0.086	0.38 ± 0.35	$227 \pm 15 \pm 208$	113 ± 7	$258 \pm 18 \pm 235$	129 ± 8

Table V.2 The effective cross section, differential in $\cos\theta$, for the reaction $\gamma_V \mathrm{Fe} \rightarrow \psi X$ ($E_X >$ 4.5 GeV), in arbitrary units. Data and statistical errors are given in (a) for $0 < z < 0.7$ and (b) for $0.7 < z < 0.9$. Results are tabulated *vs.* ($|\cos\theta|$) for data summed over Q^2 and for data with Q^2 less than and greater than 0.4 (GeV/c)^2. Also presented are the values of η_C and chisquared for fits of each data set to the form $1 + \eta_C \cos^2\theta$.

z : (a)		$0 < z < 0.7$	
Q^2 :	all	< 0.4	> 0.4
$\langle Q^2 \rangle$(GeV/c)^2	1.3	0.12	2.8
$\langle\|\cos\theta\|\rangle$		$d\sigma_{eff}/d\cos\theta$(arbitrary units)	
0.14	1.07 ± 0.10	1.10 ± 0.13	1.10 ± 0.16
0.25	0.89 ± 0.09	0.80 ± 0.12	1.03 ± 0.14
0.39	1.03 ± 0.10	1.30 ± 0.16	0.74 ± 0.14
0.56	0.87 ± 0.12	0.80 ± 0.16	1.03 ± 0.19
0.71	0.98 ± 0.25	1.14 ± 0.45	0.91 ± 0.37
η_C	-0.25 ± 0.39	-0.18 ± 0.57	-0.34 ± 0.60
χ^2/DF	2.4/3	8.3/3	3.4/3
z : (b)		$0.7 < z < 0.9$	
Q^2 :	all	< 0.4	> 0.4
$\langle Q^2 \rangle$(GeV/c)^2	0.92	0.10	2.2
$\langle\|\cos\theta\|\rangle$		$d\sigma_{eff}/d\cos\theta$ (arbitrary units)	
0.13	1.04 ± 0.10	1.07 ± 0.12	1.01 ± 0.14
0.25	0.93 ± 0.09	0.95 ± 0.12	0.96 ± 0.13
0.40	1.31 ± 0.12	1.47 ± 0.17	1.10 ± 0.16
0.56	1.11 ± 0.12	1.31 ± 0.18	0.95 ± 0.16
0.73	1.30 ± 0.26	1.66 ± 0.49	1.03 ± 0.32
η_C	0.58 ± 0.41	1.28 ± 0.68	0.01 ± 0.51
χ^2/DF	5.1/3	4.5/3	0.5/3

Table V.3 The effective cross section, differential in ϕ, for the reaction $\gamma_V \mathrm{Fe} \rightarrow \psi X$ ($E_X >$ 4.5 GeV), in arbitrary units. Data and statistical errors are given vs. $\langle\phi_F\rangle$ for data with $Q^2 >$ 0.4(GeV/c)^2 in the z regions defined by $0 < z < 0.7$ and $0.7 < z < 0.9$. The bottom two rows present the values of η_A and chi-squared for fits of each data set to the form $1 + \eta_A \cos 2\phi$.

$Q^2 > 0.4\,(\mathrm{GeV}/c)^2$			
$0 < z < 0.7$		$0.7 < z < 0.9$	
$\langle\phi_F\rangle$	$d\sigma_{eff}/d\phi$ (arb. units)	$\langle\phi_F\rangle$	$d\sigma_{eff}/d\phi$ (arb. units)
0.31	1.22 ± 0.22	0.33	0.70 ± 0.16
0.46	0.78 ± 0.16	0.52	0.68 ± 0.15
0.69	0.84 ± 0.17	0.68	1.00 ± 0.19
0.91	1.25 ± 0.22	0.95	1.32 ± 0.20
1.12	1.15 ± 0.22	1.12	1.32 ± 0.18
1.25	1.00 ± 0.19	1.25	1.20 ± 0.17
η_A	-0.11 ± 0.14	-0.41 ± 0.12	
χ^2/DF	5.0/4	2.4/4	

Table V.4 The effective cross section, differential in z and $p_\perp^2$, for the reaction $\gamma_V \mathrm{Fe} \rightarrow \psi X$ ($E_X > 4.5$ GeV) in arbitrary units. Data and statistical errors are presented *vs.* $p_\perp^2$ for the elasticity regions $0 < z < 0.7$ and $0.7 < z < 0.9$. These data are plotted in Figure V.4.

$\gamma_V \mathrm{Fe} \rightarrow \psi X$ ($E_X > 4.5$ GeV)			
$0 < z < 0.7$		$0.7 < z < 0.9$	
$p_\perp^2$ (GeV/c)^2	$d^2\sigma_{eff}/dzdp_\perp^2$ (arbitrary units)	$p_\perp^2$ (GeV/c)^2	$d^2\sigma_{eff}/dzdp_\perp^2$ (arbitrary units)
0.16	8.48 ± 1.30	0.14	9.71 ± 1.01
0.39	6.80 ± 0.70	0.34	6.19 ± 0.56
0.89	3.91 ± 0.39	0.82	2.62 ± 0.25
1.49	2.05 ± 0.27	1.50	1.28 ± 0.18
2.47	0.90 ± 0.16	2.30	0.65 ± 0.13
3.19	0.86 ± 0.22	3.15	0.385 ± 0.074
4.44	0.42 ± 0.12	4.56	0.269 ± 0.061
5.83	0.134 ± 0.062	5.81	0.102 ± 0.033
8.56	0.037 ± 0.016	7.37	0.070 ± 0.019

Table V.5 The Q^2 dependence of the effective cross section for the reaction $\gamma_V \mathrm{Fe} \rightarrow \psi X$ ($E_X >$ 4.5 GeV), normalized to unity at $Q^2 = 0$. Data and statistical errors are presented with their corresponding Q^2 for the elasticity regions $z < 0.7$ (left columns), $0.7 < z < 0.9$ (center two columns), and $z < 0.9$ (right columns). These data are plotted in Figure V.5.

$\gamma_V \mathrm{Fe} \rightarrow \psi X$ ($E_X >$ 4.5 GeV)					
$z < 0.7$		$0.7 < z < 0.9$		$z < 0.9$	
Q^2 (GeV/c)^2	$\frac{\sigma_{eff}(Q^2)}{\sigma_{eff}(0)}$	Q^2 (GeV/c)^2	$\frac{\sigma_{eff}(Q^2)}{\sigma_{eff}(0)}$	Q^2 (GeV/c)^2	$\frac{\sigma_{eff}(Q^2)}{\sigma_{eff}(0)}$
0.074	0.954 ± 0.091	0.058	0.898 ± 0.078	0.058	0.905 ± 0.061
0.19	1.02 ± 0.11	0.16	0.933 ± 0.091	0.17	0.962 ± 0.070
0.42	0.90 ± 0.17	0.39	0.95 ± 0.16	0.42	1.03 ± 0.13
0.79	0.72 ± 0.15	0.67	1.17 ± 0.18	0.65	1.03 ± 0.12
1.18	0.92 ± 0.18	1.07	0.91 ± 0.17	1.11	0.93 ± 0.13
2.25	0.74 ± 0.12	2.10	0.69 ± 0.11	2.09	0.688 ± 0.084
4.68	0.41 ± 0.10	4.33	0.411 ± 0.089	4.50	0.489 ± 0.089
8.42	0.23 ± 0.12	8.42	0.136 ± 0.048	8.25	0.208 ± 0.058
24.6	0.094 ± 0.043	21.9	0.049 ± 0.043	20.3	0.082 ± 0.036

Table V.6 The E_γ dependence of the effective cross section $\gamma N \rightarrow \psi X$ (inelastic). Absolutely normalized data and statistical errors, corrected for elastic contamination of the $E_X > 4.5$ GeV sample and extrapolated to $Q^2 = 0$ as described in the text, are presented *vs.* E_γ for the elasticity regions $z < 0.7$ (left columns), $0.7 < z < 0.9$ (center two columns), and $z < 0.9$ (right columns). These data are plotted in Figure V.6.

γFe $\rightarrow \psi X$ (inelastic)					
$z < 0.7$		$0.7 < z < 0.9$		$z < 0.9$	
E_γ	σ_{eff}(nb)	E_γ	σ_{eff}(nb)	E_γ	σ_{eff}(nb)
42.2	4.9 ± 1.6	42.1	4.3 ± 0.9	42.1	7.6 ± 1.3
58.5	5.1 ± 0.8	58.2	6.6 ± 0.8	58.3	11.1 ± 1.0
80.7	6.1 ± 0.7	81.9	7.1 ± 0.8	81.0	12.7 ± 1.0
111.0	10.5 ± 1.0	111.0	7.8 ± 0.9	110.6	16.8 ± 1.3
146.7	13.1 ± 1.3	143.6	10.6 ± 1.4	144.1	22.1 ± 1.8
177.6	12.5 ± 2.1	180.2	14.0 ± 3.0	177.9	26.4 ± 3.5

Table V.7 Results of fits to the E_γ dependence of the inelastic ψ cross section, $\sigma_{eff}(\gamma N \to \psi X)$, of the form $A\nu^p$, where σ_{eff} is in nb. when ν is in GeV. A, p, and the resulting chisquared (for 4 degrees of freedom) are presented for the three elasticity regions $z < 0.7$, $0.7 < z < 0.9$, and $z < 0.9$ considered in Figure V.6 and Table IV.12.

$\sigma_{eff}(\nu, Q^2 = 0) = A\nu^p$			
$\gamma N \to \psi X$ (inelastic)			
	A	p	χ^2/DF
$z < 0.7$	0.11 ± 0.07	0.95 ± 0.14	4.2/4
$0.7 < z < 0.9$	0.45 ± 0.28	0.63 ± 0.14	2.9/4
$z < 0.9$	0.37 ± 0.16	0.82 ± 0.10	1.6/4

Table VI.1 Summary of the $d\sigma/dt$ behavior seen in various ψ photo- and muo-production experiments.

Experiment	$\langle E_\gamma \rangle$ (GeV)	A_{tgt}	$\lvert t \rvert$ range $(\mathrm{GeV}/c)^2$	$(b_I)_{eff}$ or f, b_1, b_2 $(\mathrm{GeV}/c)^{-2}$
Cornell[30]	11.0	9	0 — 2.8	1.25 ± 0.2
SLAC[29]	19	2	0 — 0.5	2.9 ± 0.3
Fermilab[31] (tagged γ)	55	2	0 — 2	1.8 ± 0.4
This experiment	93	56	0 — 5	$2.56 \pm 0.30(stat.) \pm 0.20(syst.)$ $0.82 \pm 0.4, 4.25^{+0.76}_{-0.60}, 0.93 \pm 0.11$
Fermilab[32] (broadband γ)	116	9	0 — 1.5	1.8 ± 0.6
Ref. 28	129	9	0 — 0.7	~ 3
Ref. 83	161	9	0 — 3.5	2.68 ± 0.36 $0.98 \pm 0.23, 3.48 \pm 0.80, 0.08 \pm 0.67$
Ref. 84	120	9	0 — 4	$0.875, 3.0, 1.0$
EMC[95]	120	56	0 — 3	2.31 ± 0.30

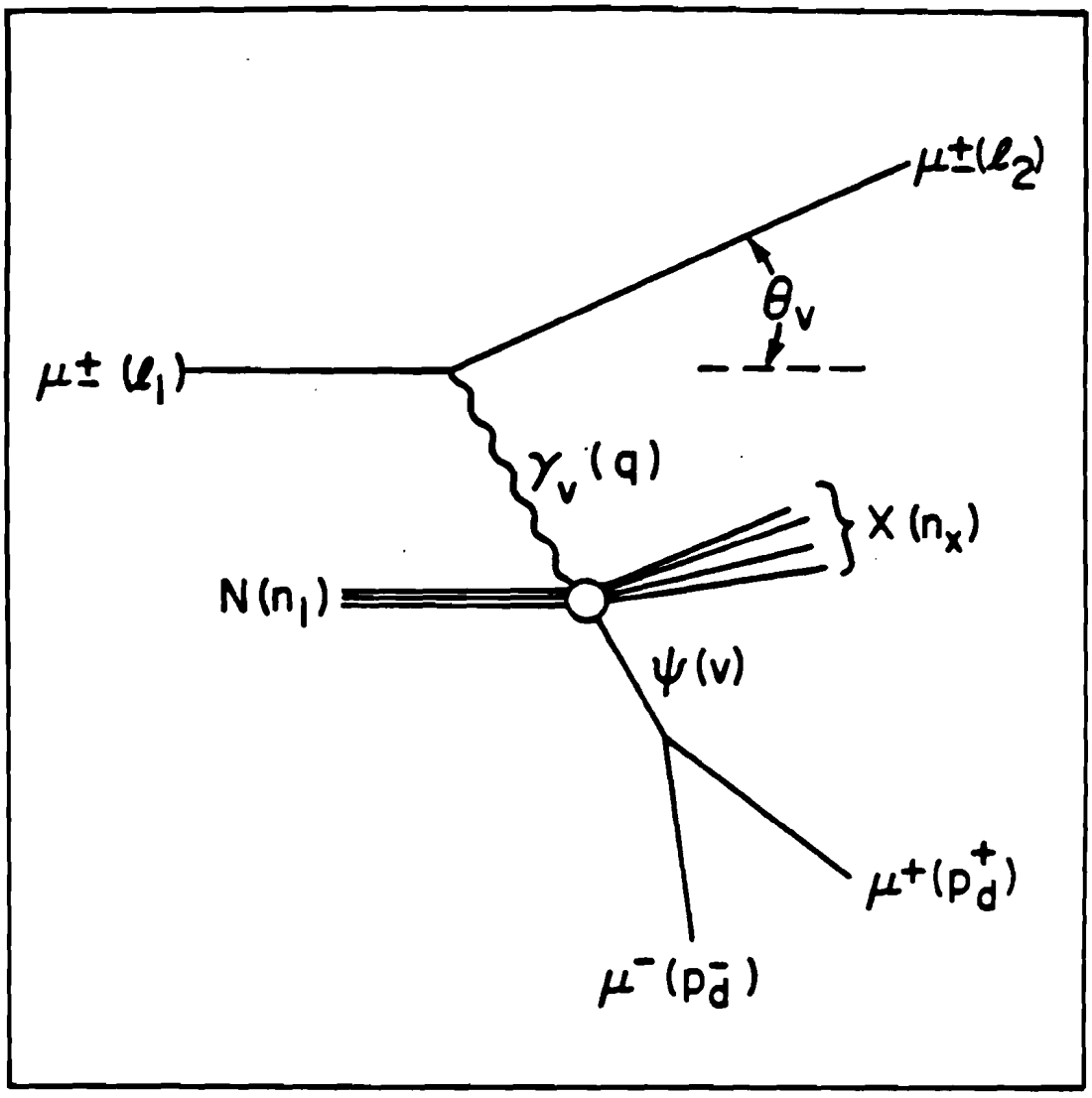

XBL 819-7316

Figure L1 The electomagnetic reaction $\mu N \to \mu\psi X$, where $\psi \to \mu^+\mu^-$, in the one photon approximation. The 4-momenta of the incoming and scattered muons, the exchanged virtual photon and produced ψ, and the initial state nucleon and final hadronic state recoiling against the ψ are l_1, l_2, q, v, n_1, and n_X, respectively. The laboratory system energies of these particles are defined as: $l_1^0 = E$, $l_2^0 = E'$, $q^0 = \nu$ (or E_γ), $v^0 = E_\psi$, $n_1^0 = m_n$, and $n_X^0 = E_X$ (or E_{had}). The ψ daughter muons' energies in the laboratory are E_d^+ and E_d^-. We define $Q^2 = -q^2$, $n_X^2 = m_X^2$, and $t = n_X - n_1 = q - v$. The laboratory angle between l_1 and l_2 is Θ_V. In addition to E_X, a measure of event elasticity is $z = E_\psi/\nu = 1 - E_{had}/\nu$.

Figure L.2 Models for elastic ψ muoproduction. Part (a) shows the vector-meson dominance picture, where the virtual photon couples directly to an off-shell ψ meson with a Q^2 independent coupling strength em_ψ^2/f_ψ. The ψ's are finally brought on-shell when, by an unspecified diffractive process, they exchange momentum with the target. Part (b) shows the photon-gluon-fusion picture. There, a pair of charmed quarks are formed through the interaction of the incident photon and a gluon from the target. The coupling strength is proportional to $\alpha\alpha_S$. The process by which a $c\bar{c}$ pair of arbitrary $m_{c\bar{c}}^2$ becomes a ψ is unspecified, but presumably involves the emission of at least one soft gluon, so that color can be conserved in the reaction.

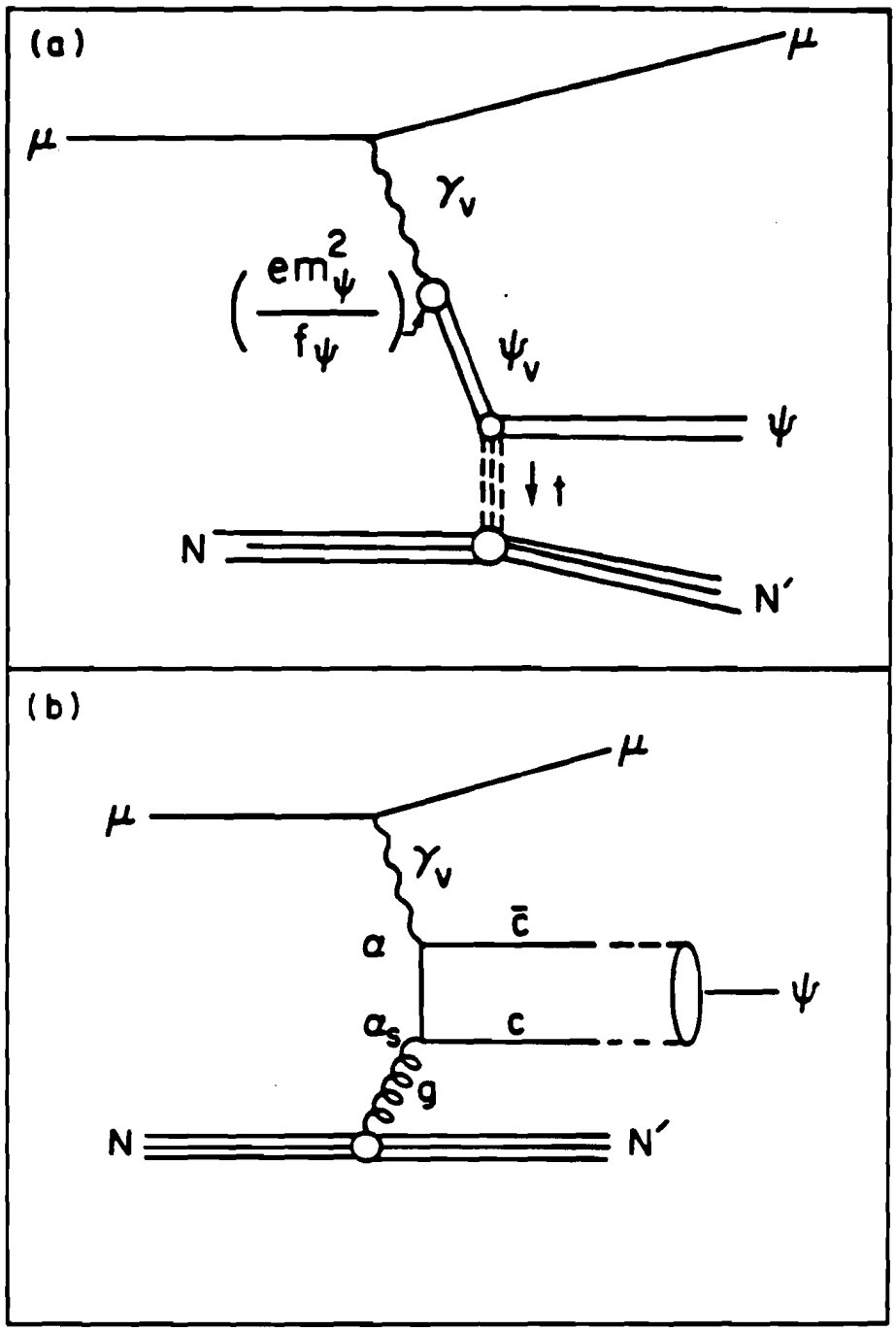

XBL 819-7315

Figure L2 Models for elastic ψ production.

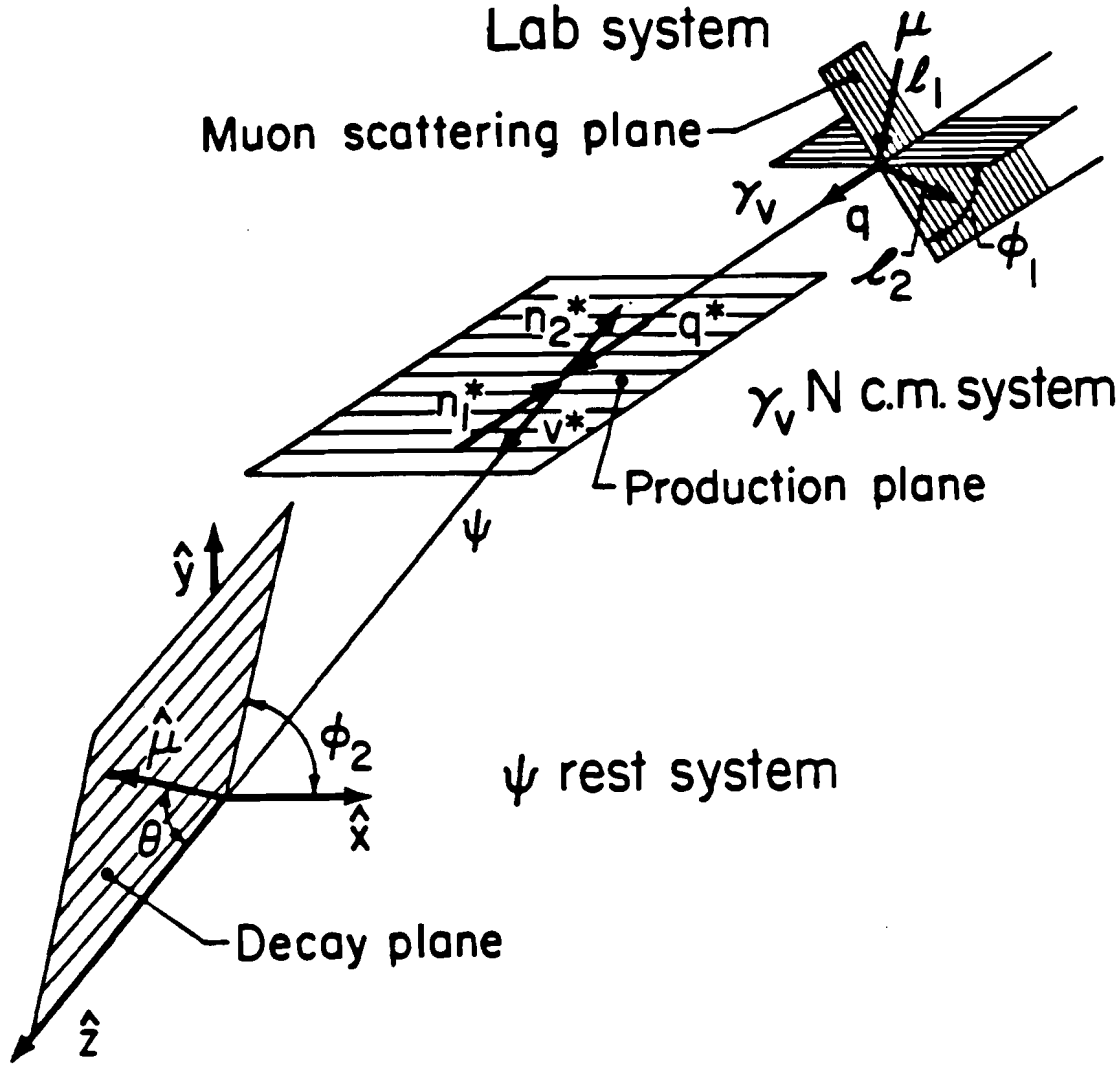

XBL819-7317

Figure L3 The coordinate systems used in the analysis of the angular distribution of the ψ's daughter muons. Here, θ is the polar angle of the beam-sign daughter muon in the ψ rest frame, where $\hat{z}$ is defined as $\mathbf{v}^*$, the ψ momentum in the $\gamma - N$ center of mass system. The azimuthal angle ϕ_2 is the angle of the ψ decay plane, measured with respect to the $\gamma \rightarrow \psi$ production plane. ϕ_1 is the azimuthal angle of the $\gamma \rightarrow \psi$ production plane measured relative to the beam muon scattering plane.

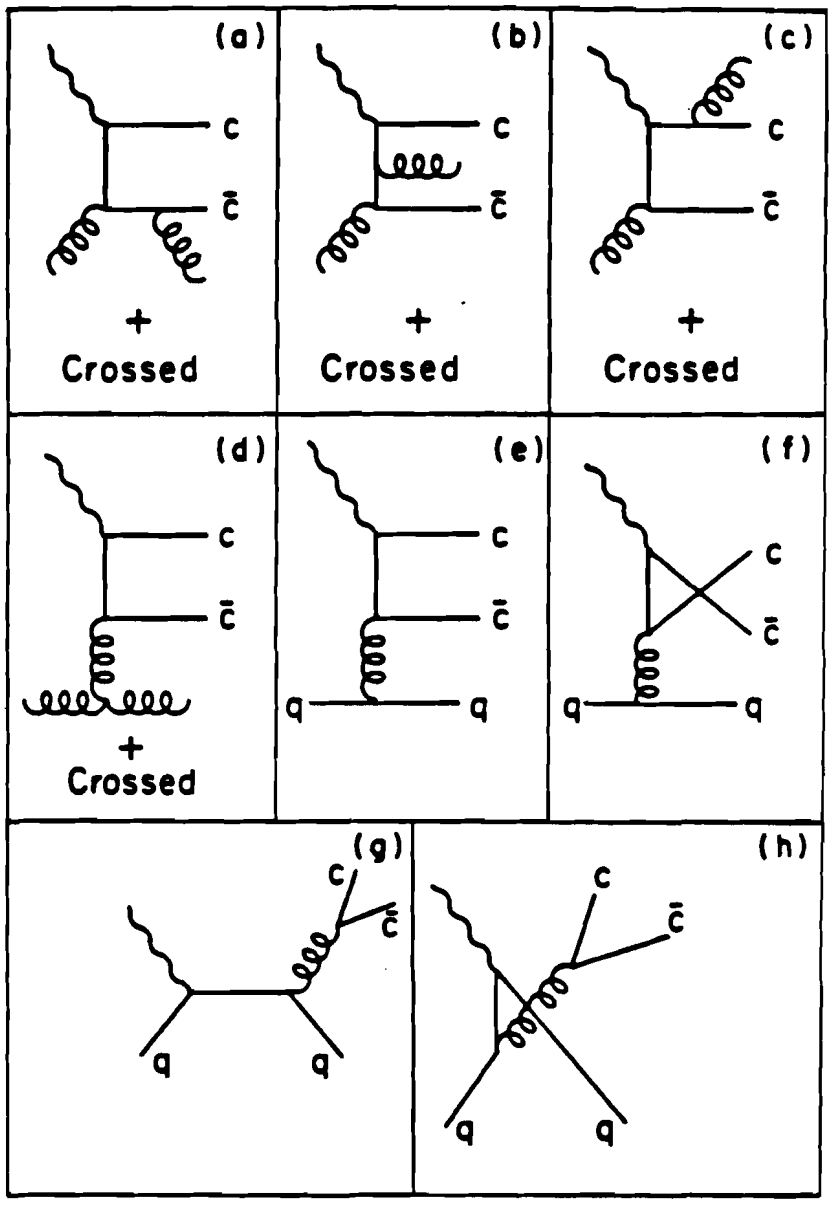

XBL819-7314

Figure L4 Feynman diagrams for the subprocesses which are second order in α_s that might contribute to ψ production. Here q is a light quark. Parts (a)–(f) correspond to diffractive production, and parts (g)–(h) to non-diffractive production.

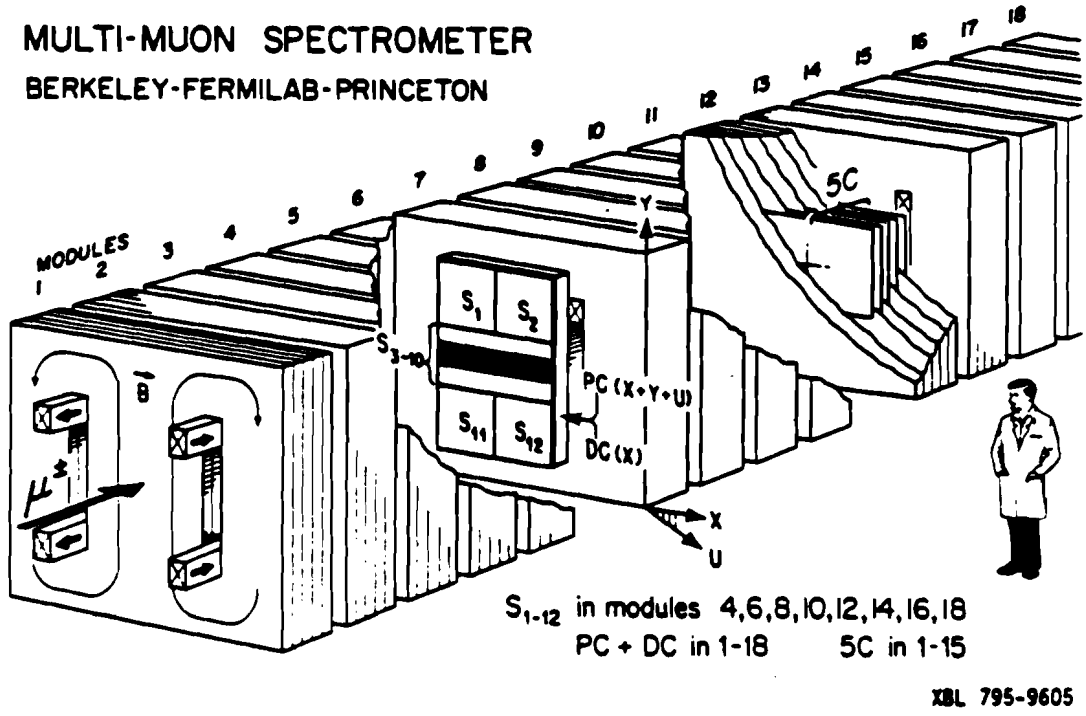

Figure II.1 Sketch of the multi-muon spectrometer. The spectrometer magnet, serving also as a target and hadron absorber, has a field which is 19.7 kG within a 1.8 × 1 × 16-m^3 fiducial volume. Over the central 1.4 × 16 m^3, the magnetic field is uniform to 3% and mapped to 0.2%. Eighteen pairs of proportional (PC) and drift chambers (DC), fully sensitive over 1.8 × 1 m^2, determine muon momenta to typically 8%. The PC's register coordinates at 30° (u) and 90° (y) to the bend direction (z) by means of 0.5-cm-wide cathode strips. Banks of trigger scintillators ($S_1 - S_{12}$) occupy eight of the eighteen magnet modules. Interleaved with the 1-cm-thick magnet plates in modules 1—15 are 75 calorimeter scintillators resolving hadron energy E_{had} with rms uncertainty $1.5\sqrt{E_{had}(\text{GeV})}$. Not shown upstream of module 1 are 1 PC and DC, 63 beam scintillators, 8 beam PC's, and 94 scintillators sensitive to accidental beam and halo muons.

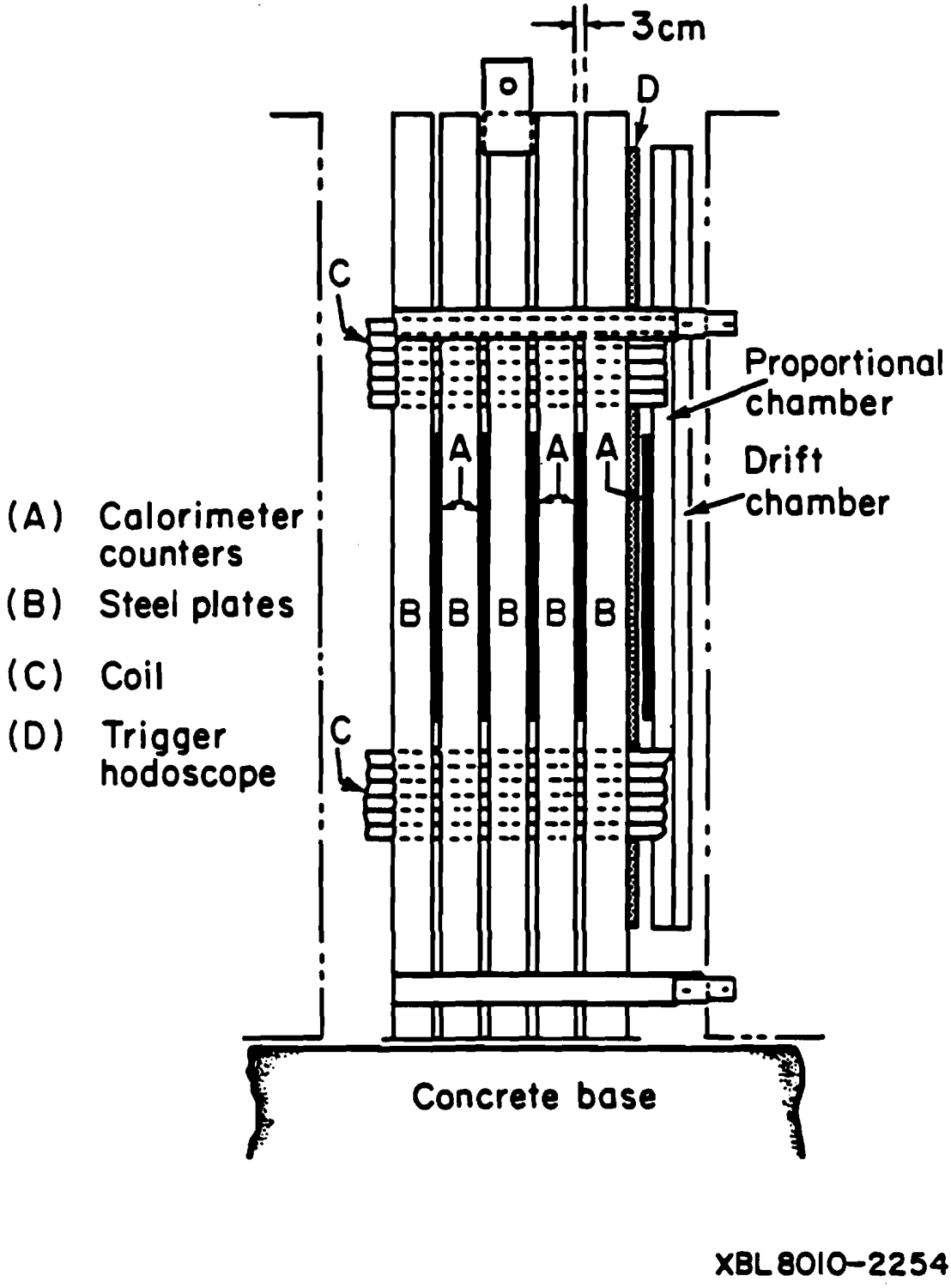

Figure II.2 One of eighteen modules comprising the Multimuon Spectrometer.

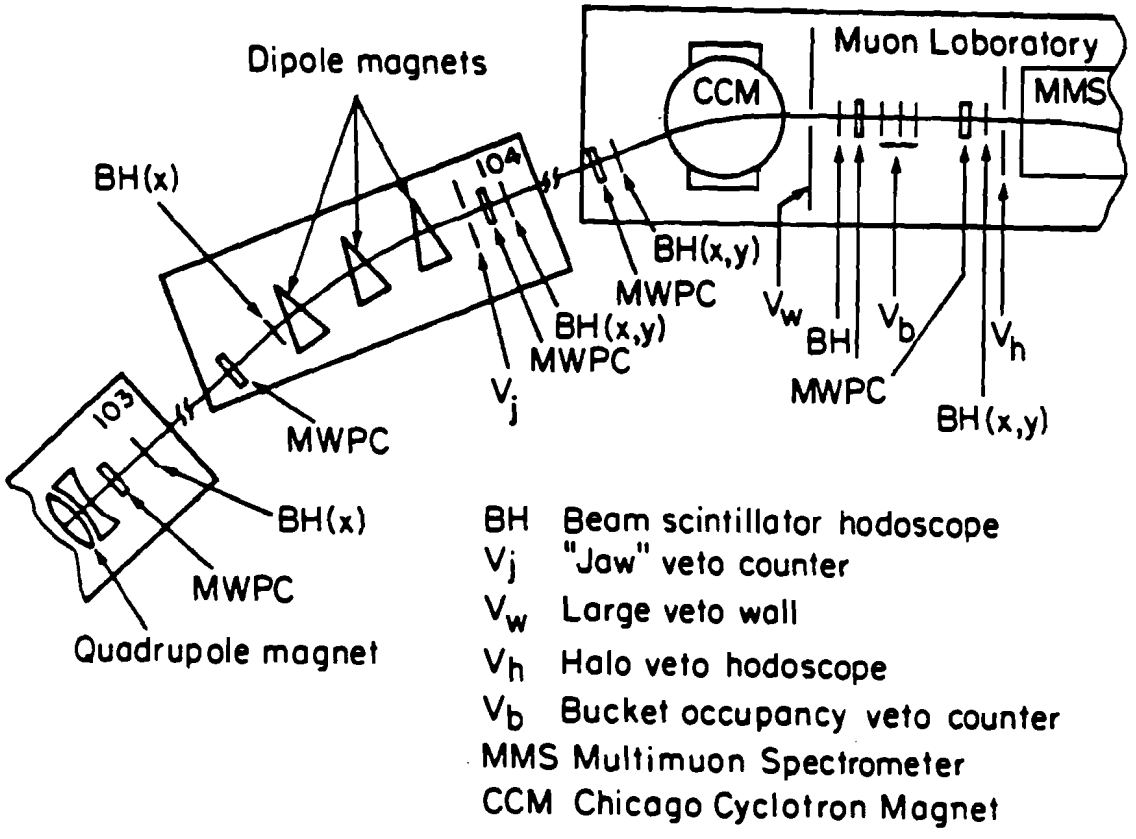

XBL 8010-2139

Figure II.3 Multiwire proportional chambers and scintillation counters used to define the beam and to measure its momentum.

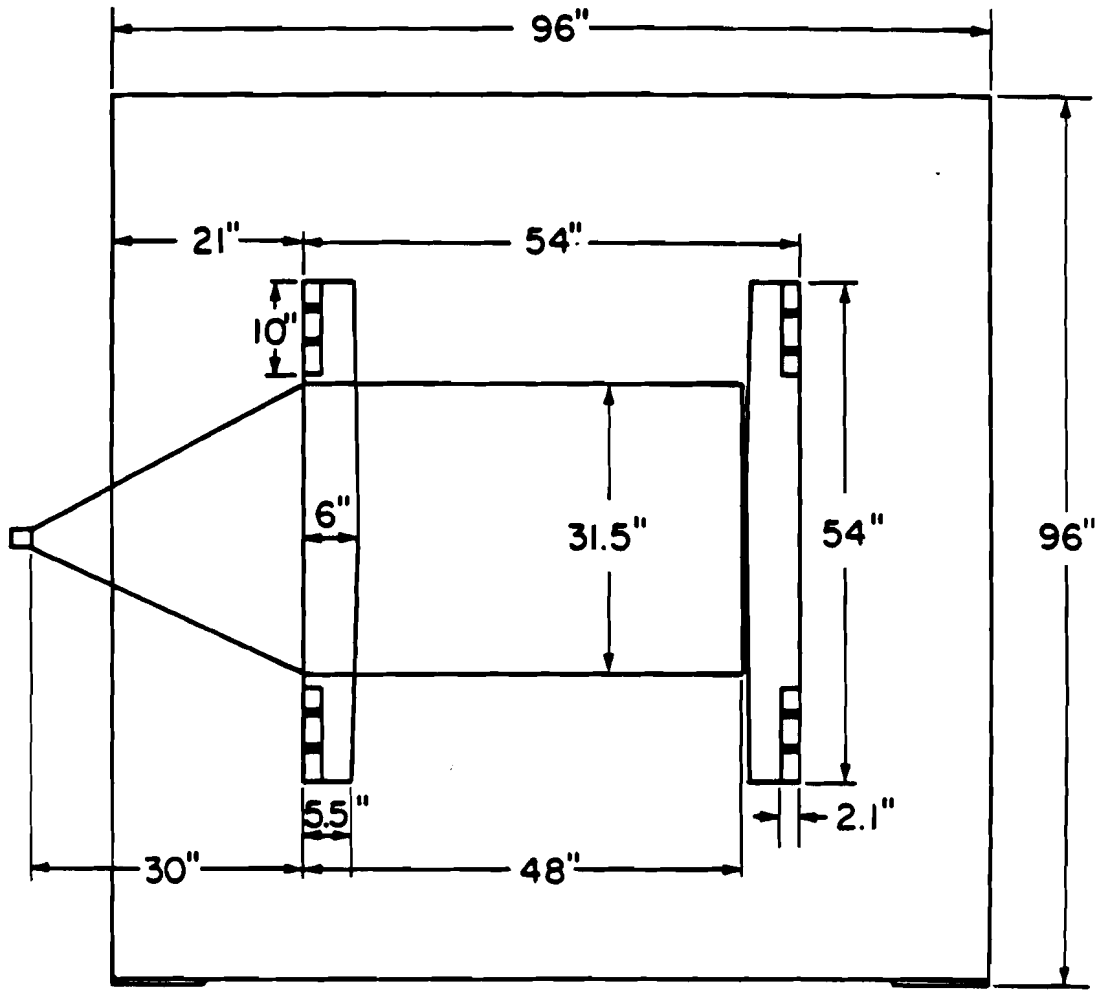

XBL819-7313

Figure II.4 Dimensions and coil slot configuration of one of the 91 steel plates in the Multimuon Spectrometer. The size and position of a calorimeter counter is also indicated.

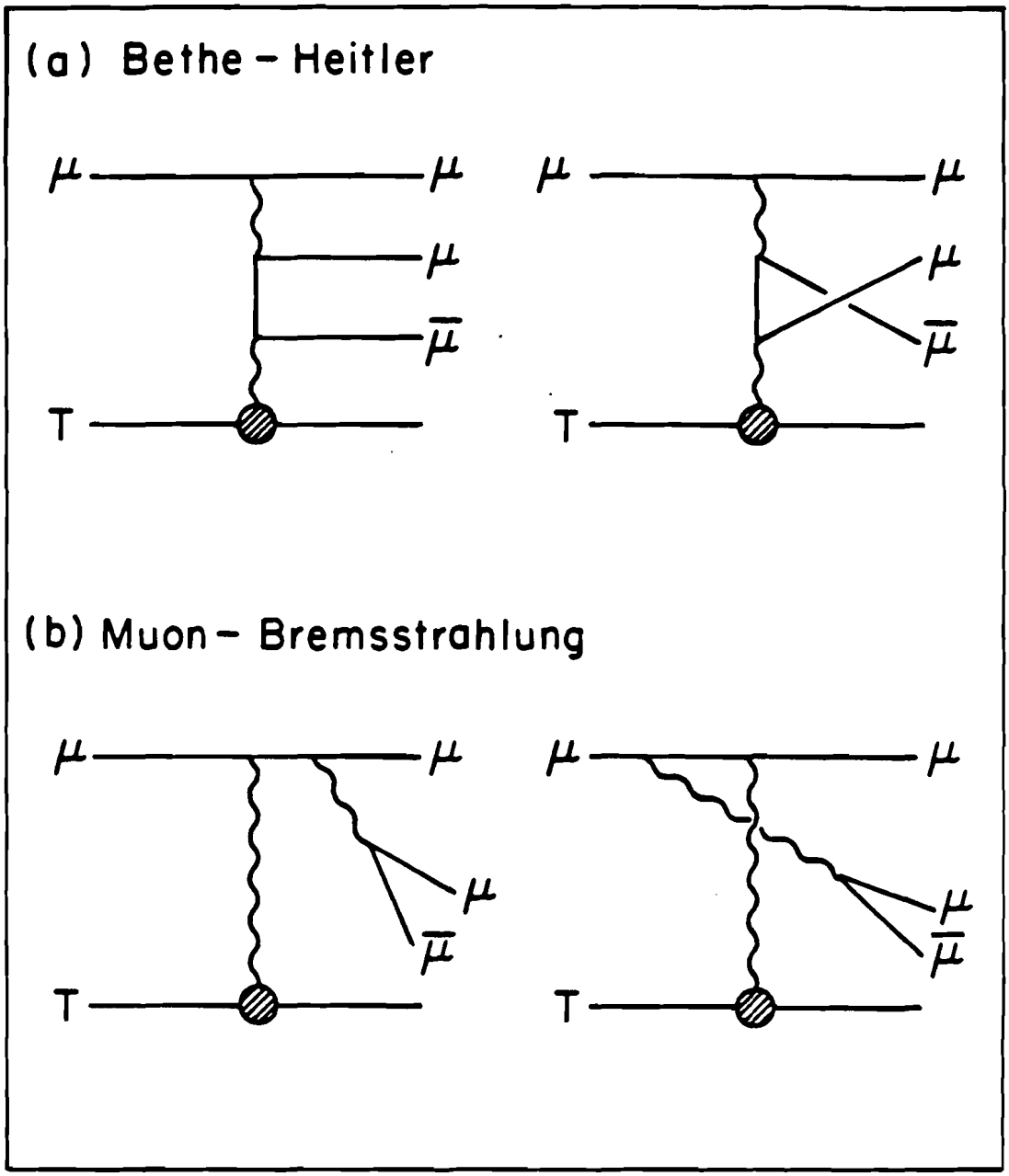

Figure II.5 Feynman diagrams for the electromagnetic production of muon pairs by the (a) Bethe-Heitler and (b) muon-bremsstrahlung processes. These muon tridents are responsible for the majority of valid trimuon triggers, and are the main backround process to ψ production.

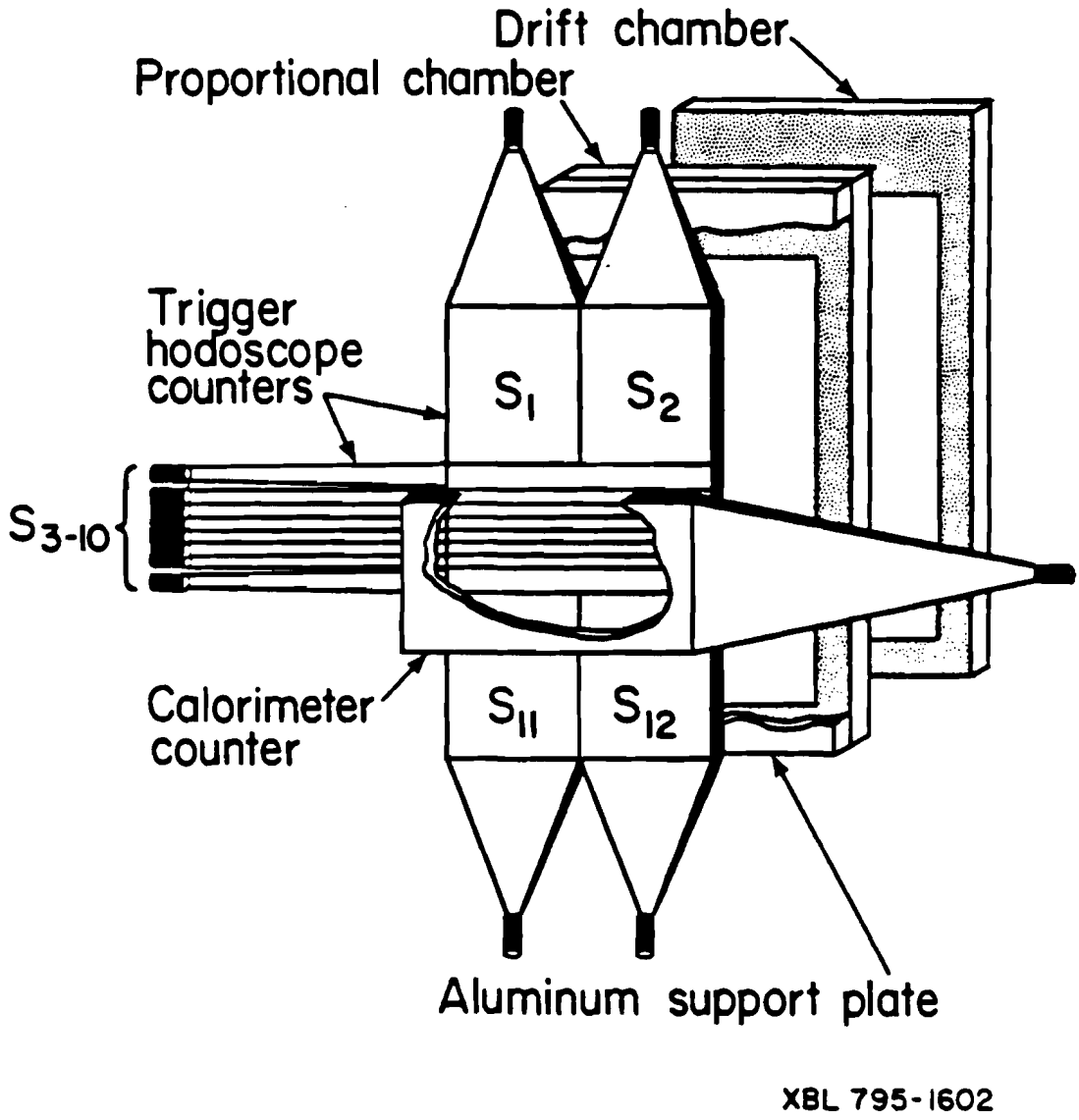

Figure II.6 An exploded view of one of the large spectrometer magnet gaps, which contains a trigger hodoscope, composed of counters $S_1 - S_{12}$, a calorimeter counter, and a multi-wire proportional chamber — drift chamber package.

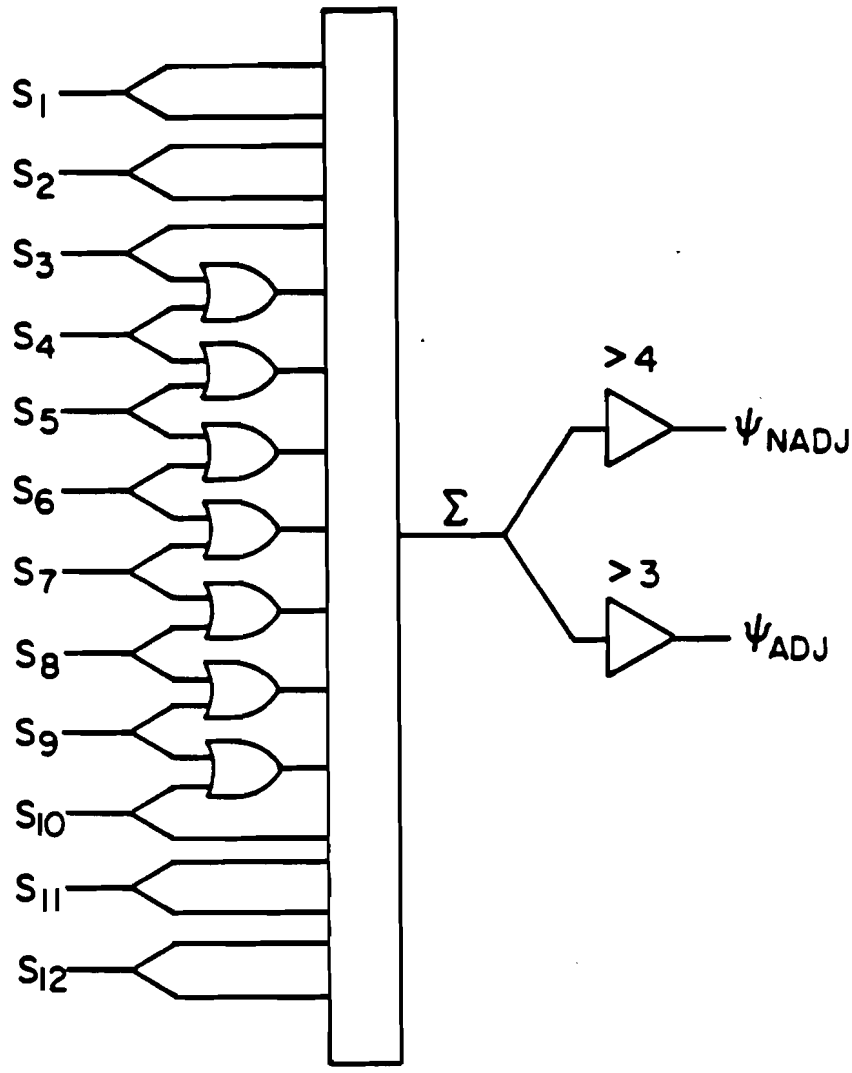

XBL 819-7310

Figure II.7 Logic for one of eight trigger hodoscopes. Signals from the stave counters S_{3-10} are split and or-ed together, so that when 3 adjacent scintillators fire, 4 counts are produced in the adder. For 3 muons to produce more than 4 counts, they must either seperate enough so that at least one fired counter is not adjacent to the others, or hit a paddle counter $S_{1,2}$ or $S_{11,12}$. The full trimuon trigger is occurs when one or more of the 6 possible subtriggers, $\psi^{i}_{adj} \bullet \psi^{i+1}_{nadj} \bullet \psi^{i+2}_{nadj}$, is satisfied.

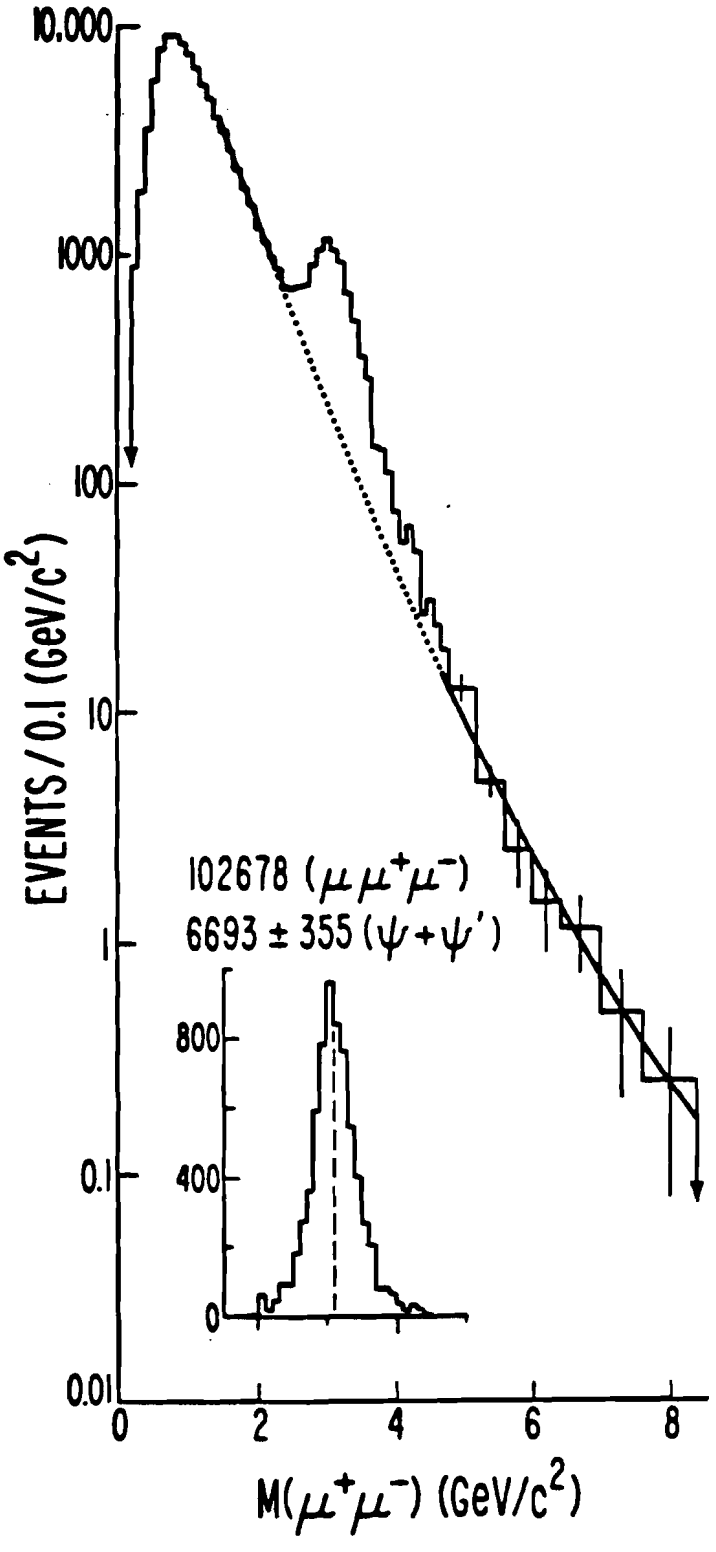

Figure II.8 Spectrum of muon pair masses for all data under slightly more general cuts than those used in this analysis. Note that the trigger succeeds in successfully turning over the rapidly climbing distribution as $m_{\mu^+\mu^-}$ goes to zero.

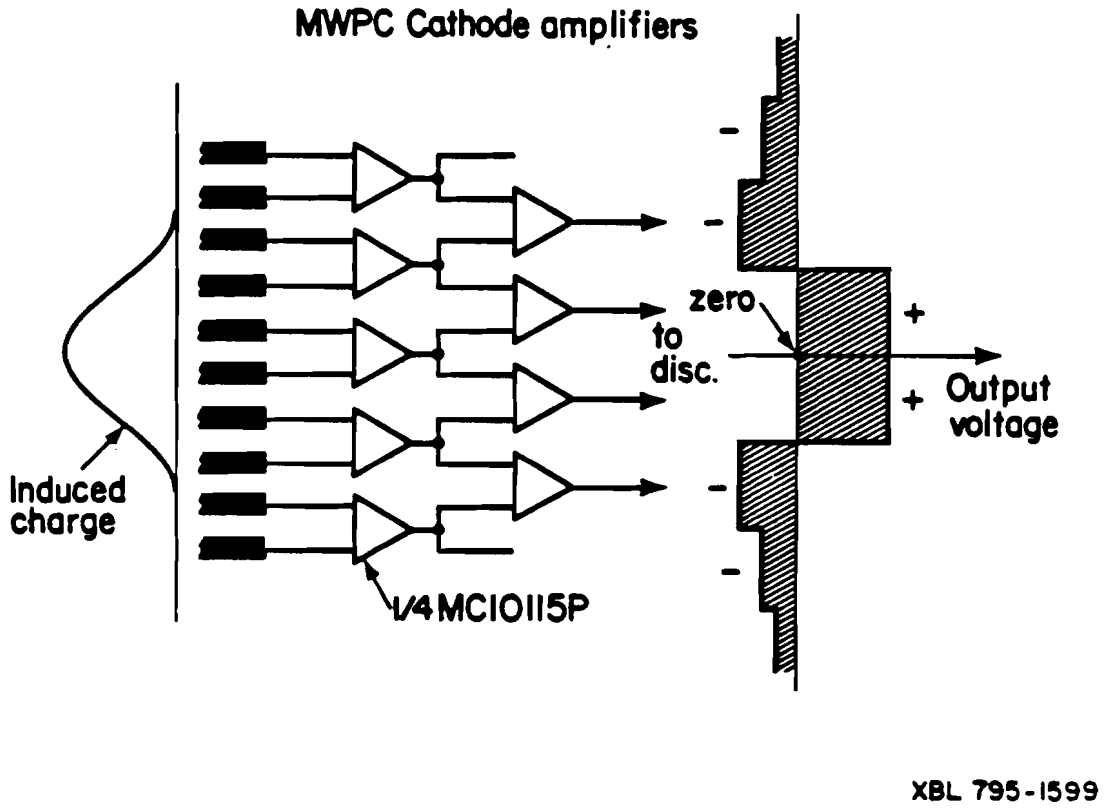

Figure II.9 Electronics scheme used on the induced planes of the multi-wire proportional chambers. By essentially taking the second derivative of the Lorentzian shaped induced charge distribution, standard charge sensitive comparators can be used for pulse center finding.

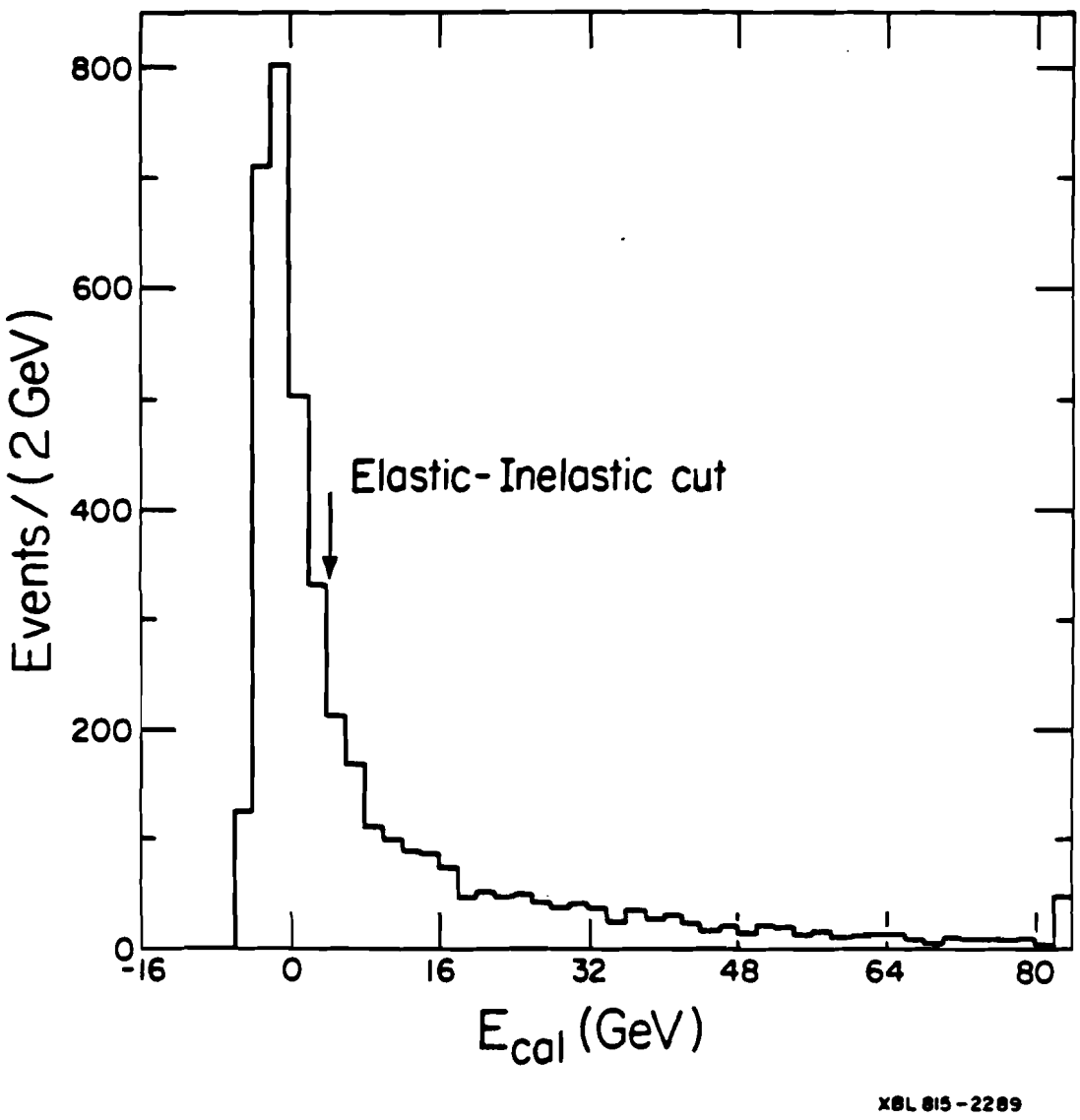

Figure III.1 The observed distribution in measured shower energy E_{had} for all trimuon events with $-0.052 < \log_{10}(m_{\mu^+\mu^-}/3.1) < 0.052$. The cut at 4.5 GeV is used to define the elastic and inelastic data samples.

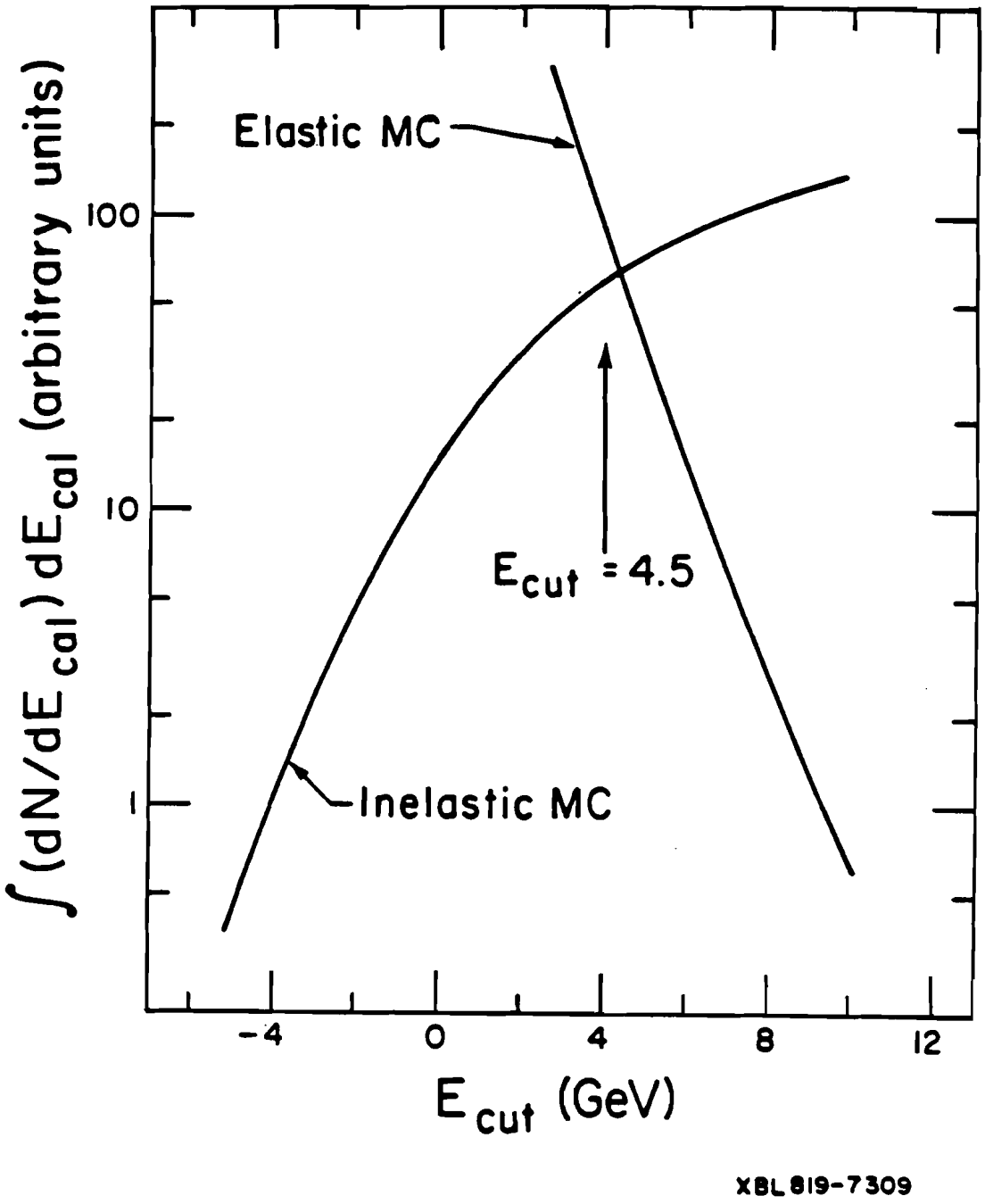

Figure III.2 The integral distributions $\int_{-\infty}^{E_{cut}} P_{inelastic}(E_{cal})dE_{cal}$ and $\int_{E_{cut}}^{\infty} P_{elastic}(E_{cal})dE_{cal}$ as a function of E_{cut}, based on the appropriately normalized MC simulations. By defining the elastic and inelastic data samples with a calorimeter energy cut at 4.5 GeV, we obviate the need for any normalization correction due to the effect of calorimeter resolution.

Figure III.3 The apparatus resolution in ν and Q^2, based on the MC simulation. Part (a) shows the quantity $\sigma(E_\gamma)/E_\gamma$ vs. E_γ both with and without the requirement that there be no (resolution induced) missing energy. In part (b) only one curve for $\sigma(Q^2)$ is shown, as no substantial change occurs when the missing energy constraint is applied.

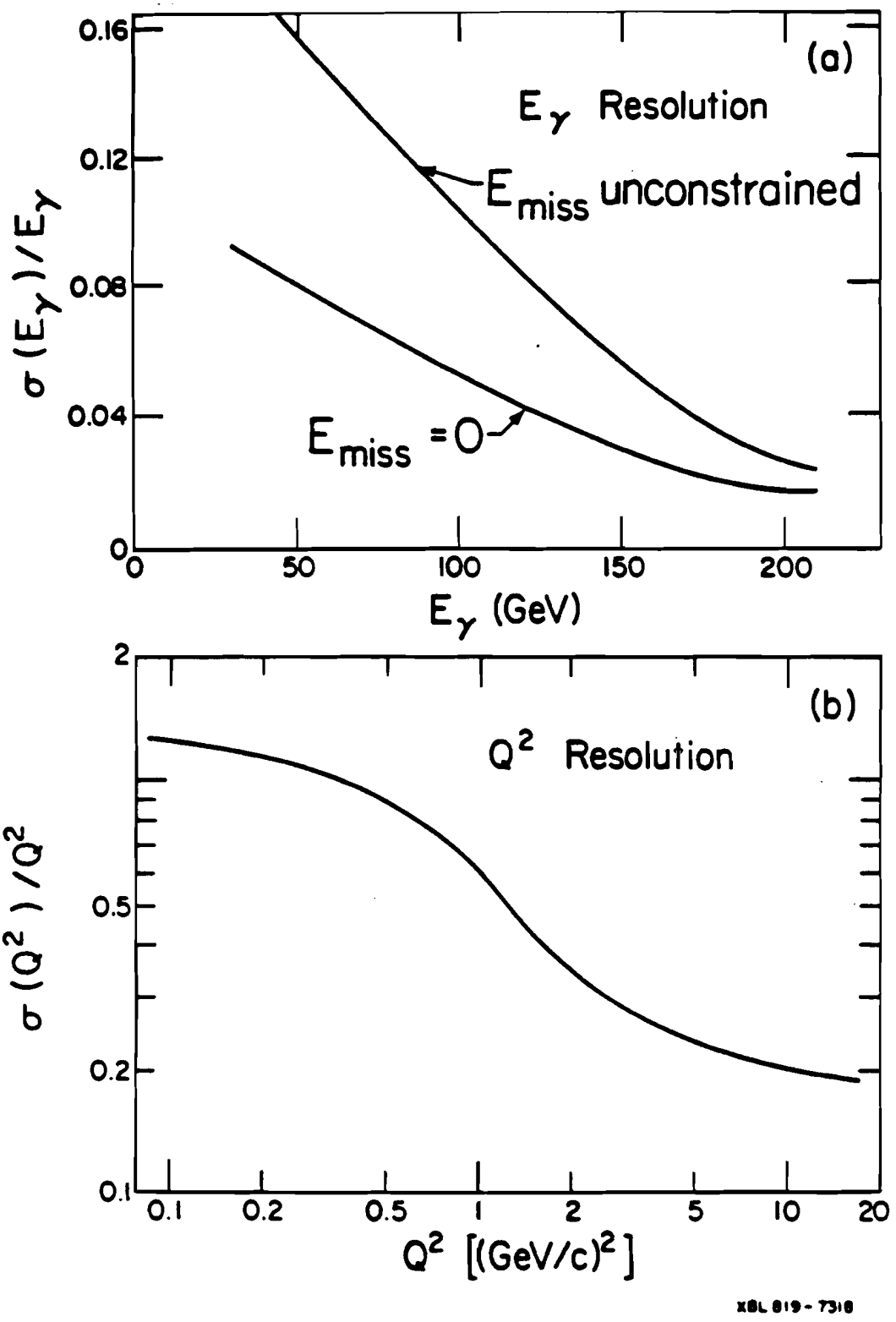

Figure III.3 Q^2 and ν resolution

Figure III.4 The muon pair mass distribution above 1.12 GeV/c^2 for the final sample of events $\mu\mathrm{Fe} \rightarrow \mu(\mu^+\mu^-)X$. Part(a) (part(b)) shows those events where E_X, as measured in the calorimeter, is less than (greater than) 4.5 GeV. The bins are of width $\Delta u = 0.026$, where $u \equiv \log_{10}(m_{\mu^+\mu^-}/3.1)$, so that each corresponds to a constant fraction ($\sim 2/3$) of the mass resolution, independent of mass. The quoted error on the number of ψ events includes the uncertainty in the amount of background subtracted, as described in the text. It is assumed that, for the elastic sample, the contribution of $\psi' \rightarrow \mu^+\mu^-$ events is 4.5% of the $\psi \rightarrow \mu^+\mu^-$ signal; this contribution is shown as a narrow shoulder on the ψ peak. No $\psi' \rightarrow \mu^+\mu^-$ events are assumed to contribute to the inelastic sample.

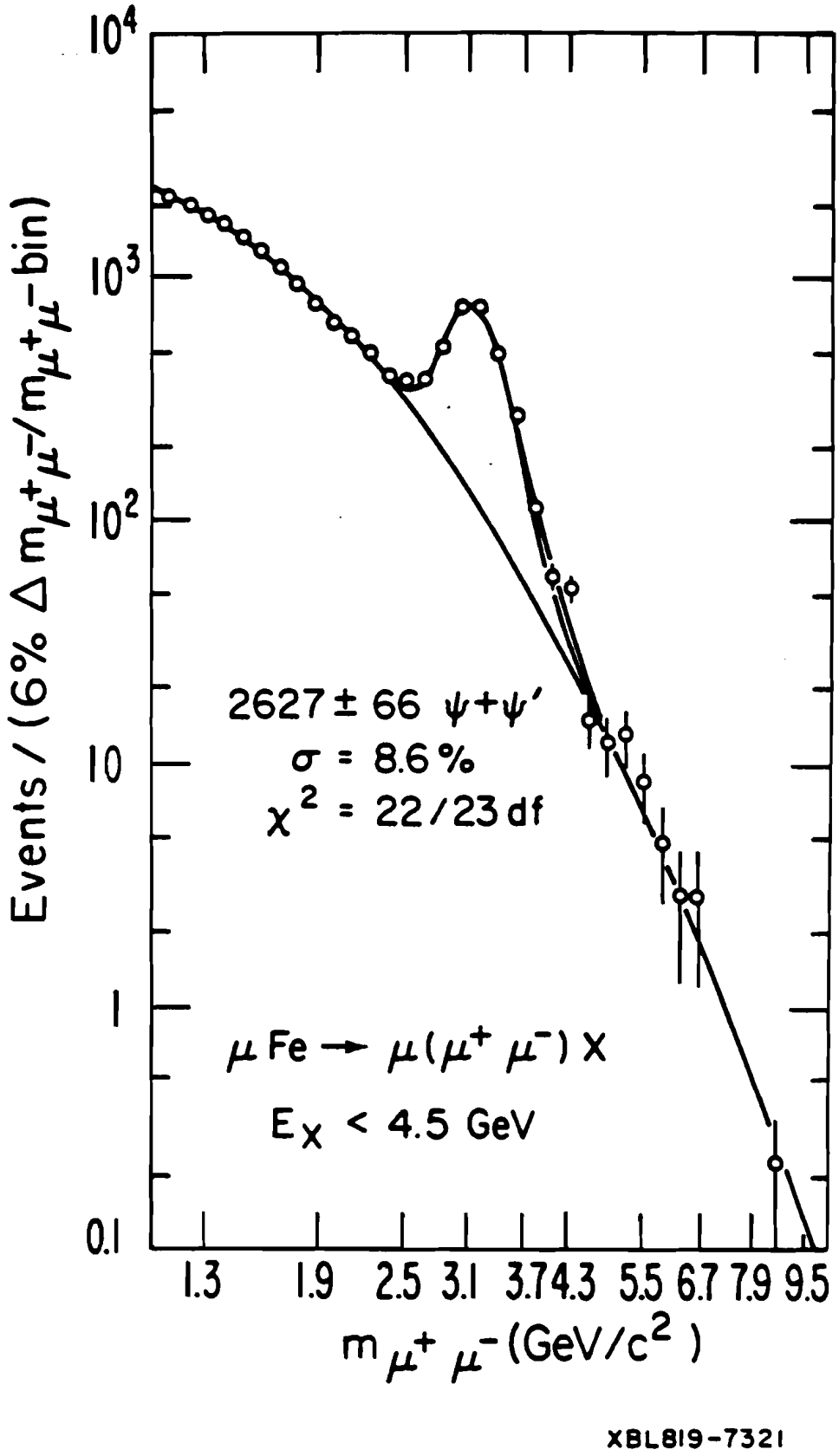

Figure III.4(a) Mass distribution for elastic trimuon events.

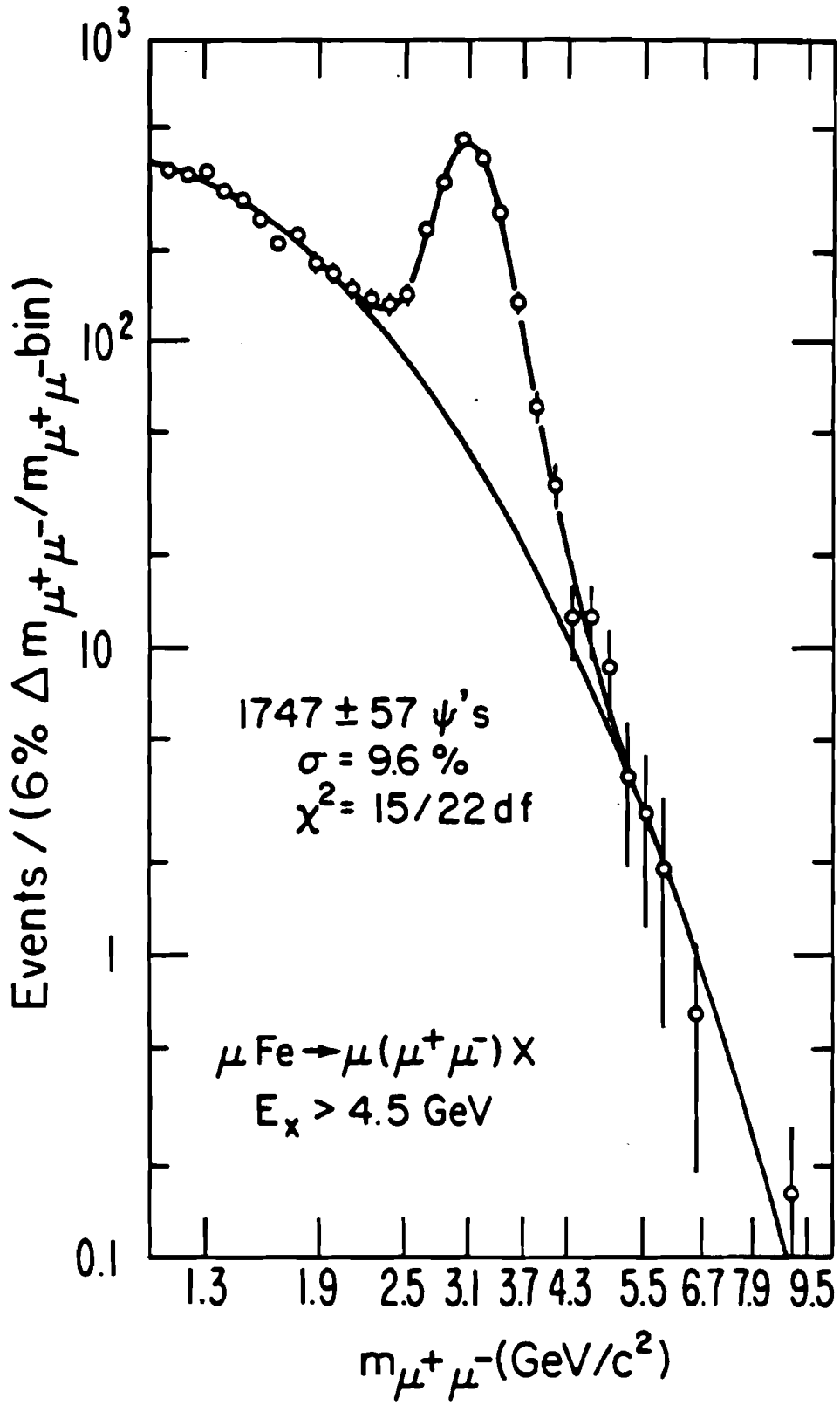

XBL 819-7319

Figure III.4(b) Mass distribution for inelastic trimuon events.

Figure III.5 The apparatus efficiency, measured with the elastic and inelastic Monte Carlo (MC) simulations, as a function of (a) Q^2, (b) $(E_d)_{min}$, (c) $p_\perp^2$, (d) $\cos\theta$, (e) $\phi = \phi_2 - \phi_1$, and (f) $z = E_\psi/\nu$. Inefficiencies induced by the reconstruction and analysis programs are not included in this measurement. Parts (a), (d), and (e) were found using the elastic MC, while parts (b), (c), and (f) were generated with the inelastic MC.

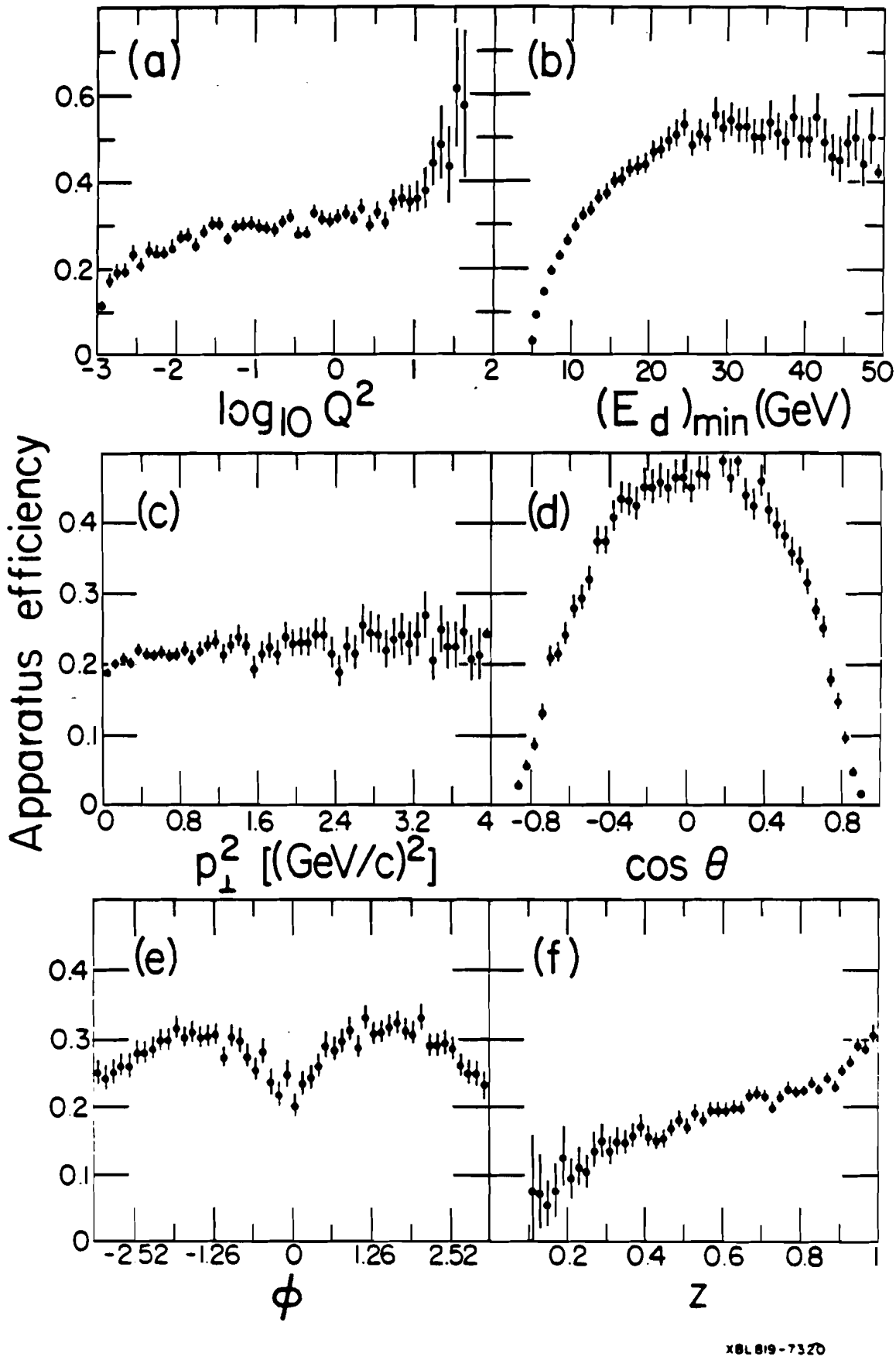

Figure III.5 Apparatus efficiency.

Figure III.6 Feynman diagrams for the radiative corrections to ψ muoproduction. Internal bremsstrahlung from the incident and scattered muons (part(a)) and from the ψ daughter muons (part(b)) contribute energy to the calorimeter and cause elastic events to fall in the inelastic sample. The corrections due to virtual photons (part(c)) have been ignored, as they only change the overall normalization and Q^2 dependence by undetectable amounts.

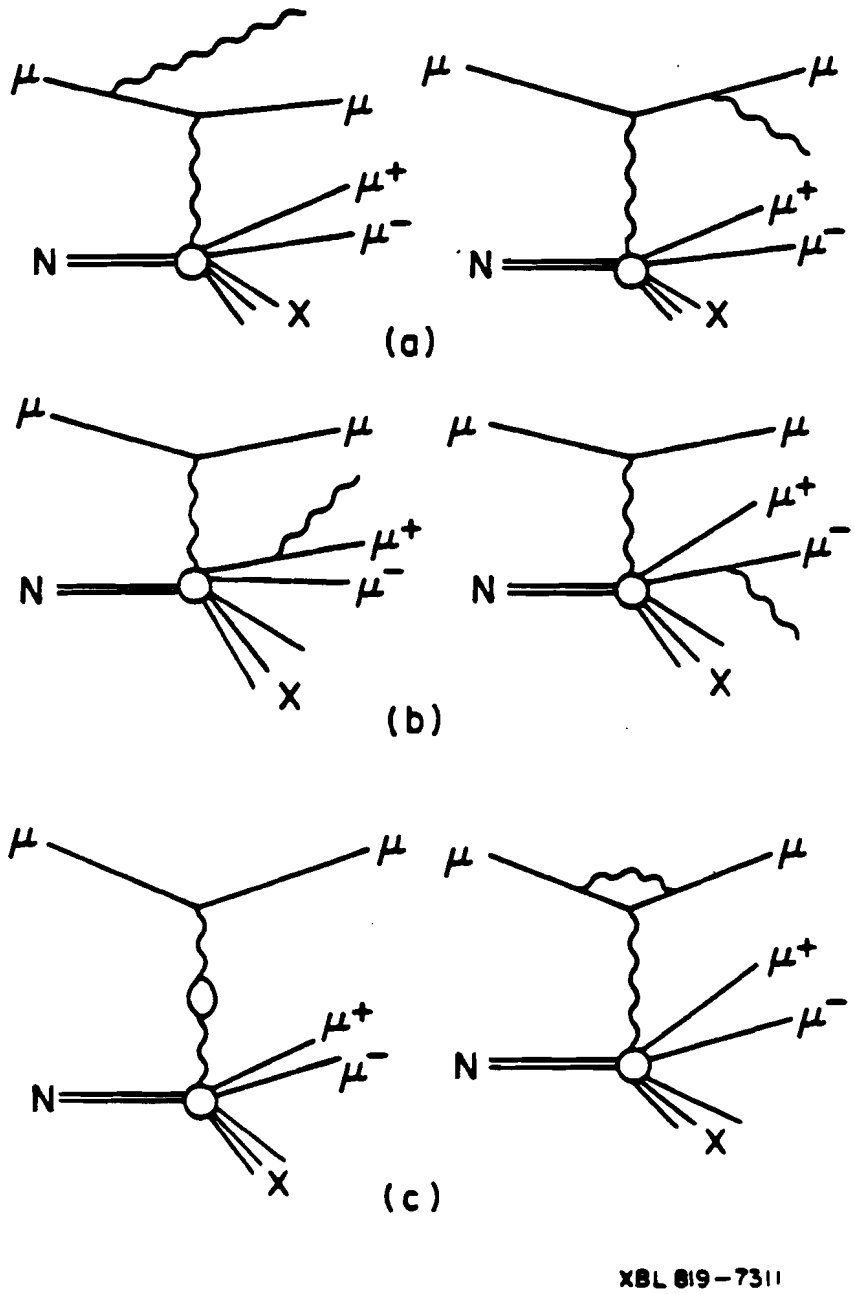

Figure III.6 Radiative corrections to ψ production.

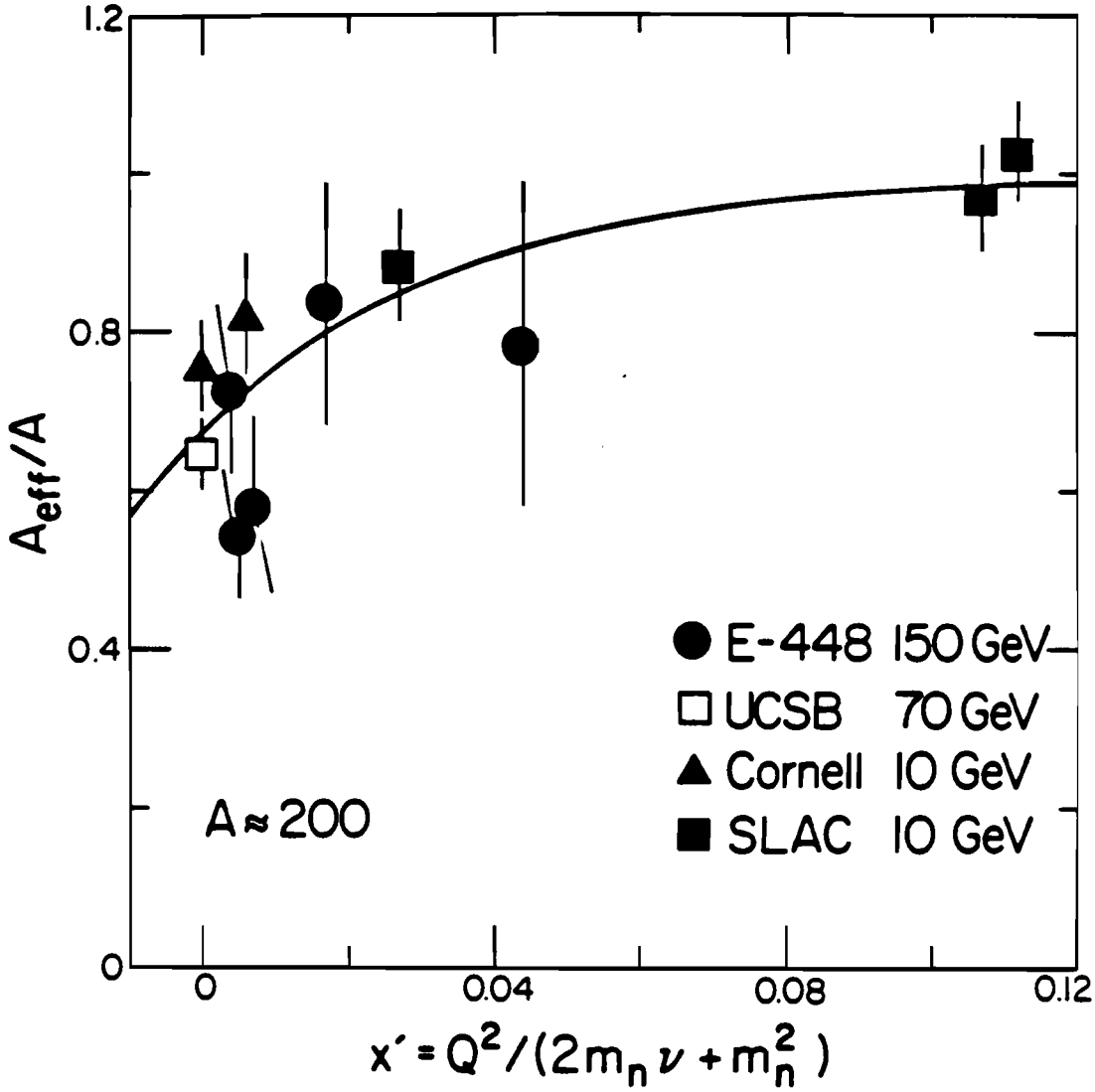

XBL815-2288

Figure III.7 Evidence for the possibility of a Q^2 dependence in nuclear shadowing. We plot the ratio of the effective number of nucleons to the actual number, A_{eff}/A, as a function of $x' \equiv Q^2/(2m_n\nu + m_n^2)$ for the experiments listed. The points labeled E-448 refer to the results of a muon scattering experiment that used the same beam as did this experiment. They provide the first measurement of nuclear shadowing at the higher values of photon energy typical of our data. The curve is a fit of the $A \approx 200$ data to the form $1.0 - a\exp(-bx')$; we find $a = 0.33 \pm 0.03$ and $b = 28 \pm 12$. When scaled to $A = 56$ the resulting expression is used to estimate the effect of nuclear shadowing on the observed Q^2 dependence of the effective photoproduction cross section for ψ production.

Figure IV.1 The t dependence of the effective cross for section the reaction $\gamma_V \mathrm{Fe} \rightarrow \psi X$ (energy (X) <4.5 GeV). In (a) we display the number of events with $-0.052 < \log_{10}(m_{\mu^+\mu^-}/3.1) < 0.052$ against measured t, defined as $t_{min} + (p_\perp^2)_\psi$. The upper histogram is all data; the lower is that portion of the data assumed due to incoherent production $\gamma_V N \rightarrow \psi N$. In (b) this incoherent contribution, corrected for all experimental effects, is plotted against the resolution unfolded values of t. The curve is the best fit of the data to the sum of two exponentials (Table IV.1, Fit 3). The data are in units of nb/(GeV/c)^2 and are normalized so that when Fit 3 is integrated over t, the result agrees with $\sigma_{\gamma_V N \rightarrow \psi N}(\langle\nu\rangle, Q^2 = 0)$. The errors are statistical only, but include the error introduced by subtracting the coherent component of the cross section. The data plotted are listed in Table IV.2.

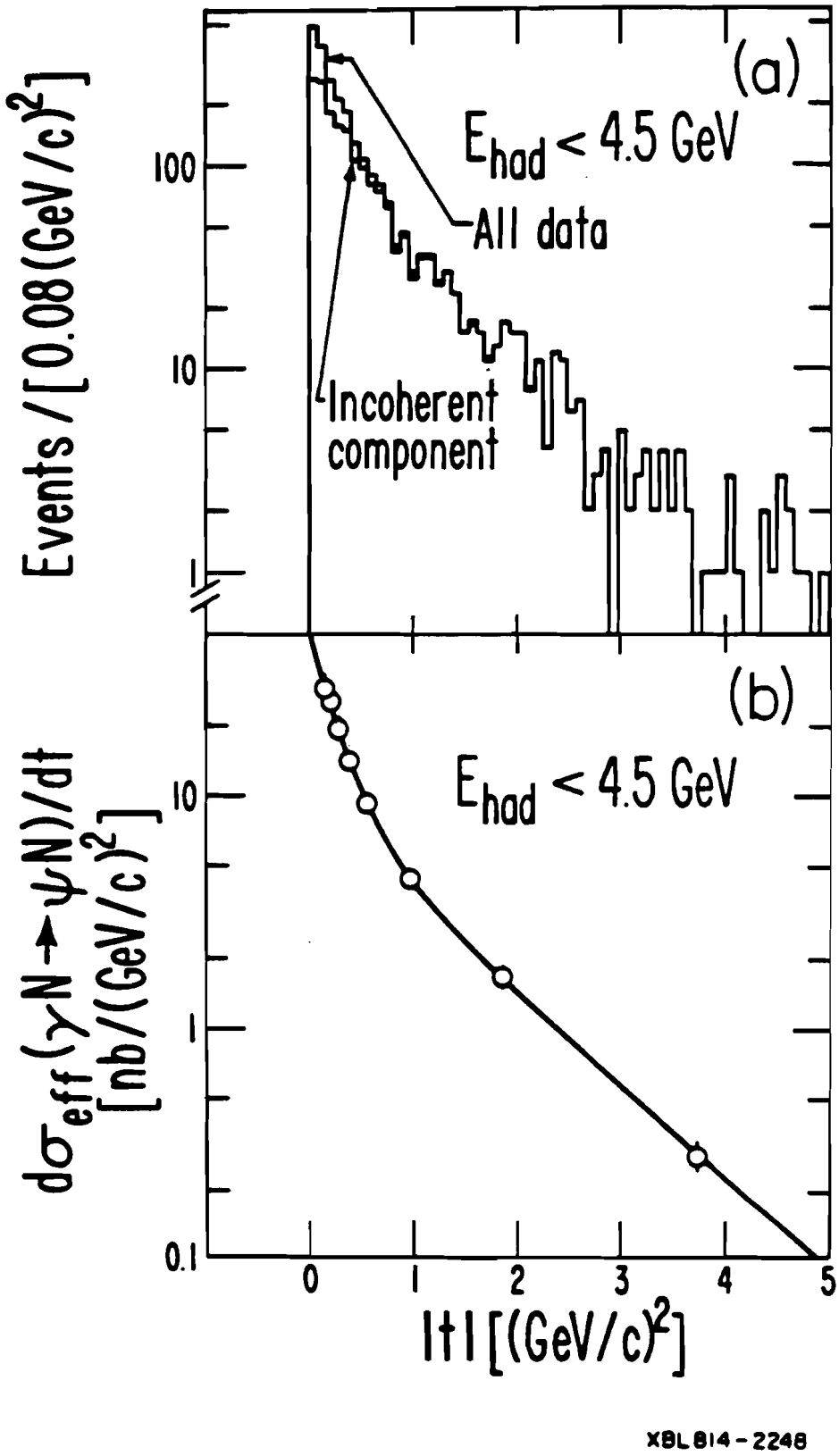

Figure IV.1 The t dependence of $\sigma_{eff}(\gamma_V \mathrm{Fe} \to \psi X)$ when $E_X < 4.5$ GeV.

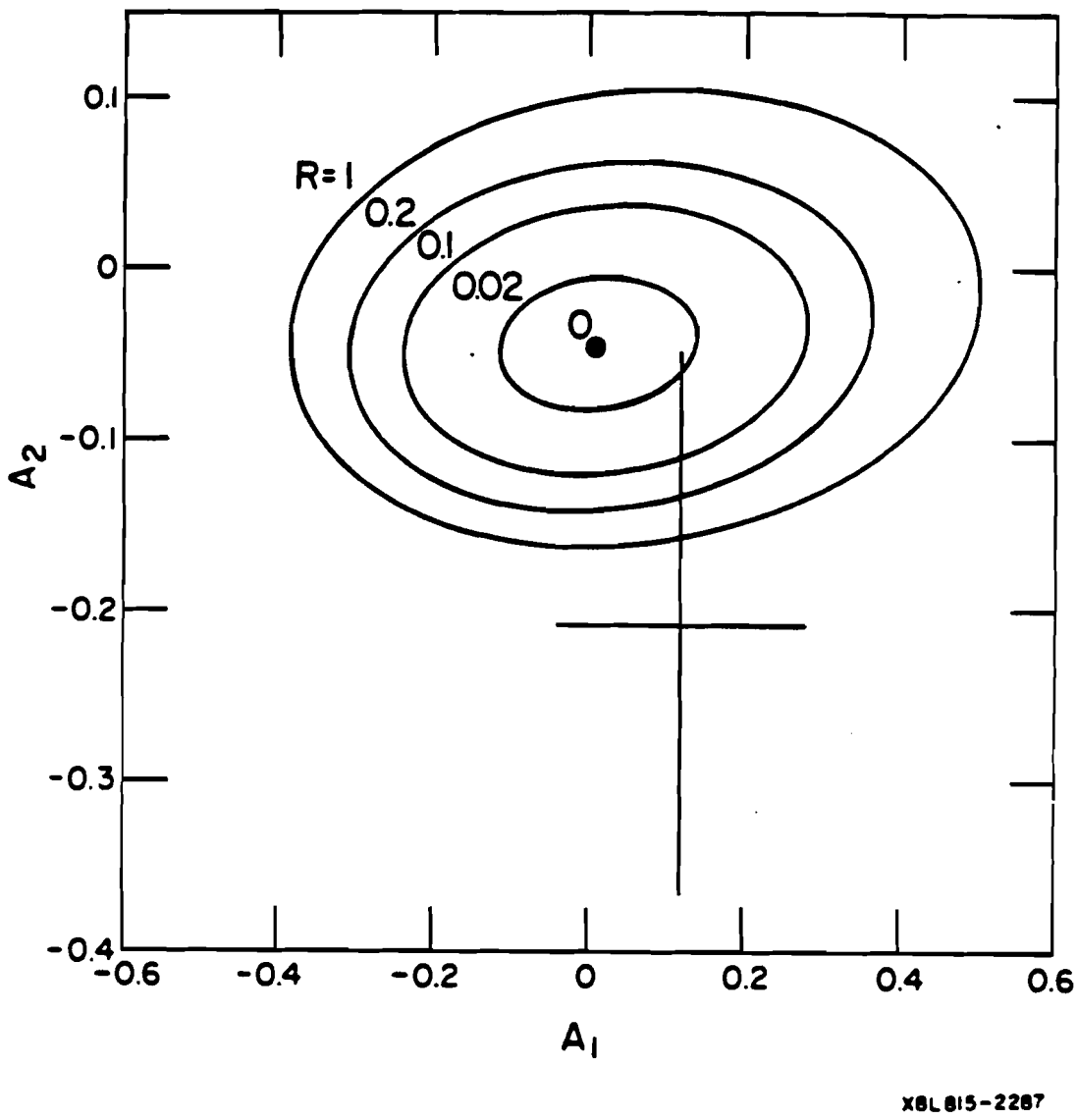

Figure IV.2 Evidence for the effect of single-spin-flip terms in the expression for the angular distribution of the μ^+ daughter from ψ decay. A_1 is the asymmetry expected from a term proportional to $\sqrt{R}\sin 2\theta \cos\phi \cos\delta$, and A_2 is that expected from a term proportional to $\sqrt{R}\sin 2\theta \sin\phi \sin\delta$. The expected values of A_1 and A_2 are calculated as a function of R and δ using the observed average values of $\cos^2\theta$, $\cos 2\phi$, $\cos\phi$, $\cos 2\theta$, ϵ, and Q^2. These are presented as a family of curves, where each curve is labeled by a value of R and δ is the parameter along the curve. The region allowed by the data is indicated, where the errors are statistical only. All values of R are allowed and $\pi < \delta < 2\pi$.

Figure IV.3 Angular dependence of the effective cross section for the reaction $\gamma_V \mathrm{Fe} \rightarrow \psi X$ (energy(X) <4.5 GeV). Data and statistical errors are presented *vs.* $|\cos\theta|$ for 4×3 bins of Q^2 and ϕ_F. Vertical columns correspond to $0 < \phi_F < \pi/6$ (left column, plots (a)–(d)), $\pi/6 < \phi_F < \pi/3$ (center column, plots (e)–(h)), and $\pi/3 < \phi_F < \pi/2$ (right column, plot (i)–(l)); horizontal rows correspond to $\log_{10} Q^2 < -0.4$ (row 1 ; plots (a), (e), and (i)), $-0.4 < \log_{10} Q^2 < 0.0$ (row 2, plots (b), (f), and (j)), $0.0 < \log_{10} Q^2 < 0.5$ (row 3, plots (c), (g), and (k)), and $0.5 < \log_{10} Q^2$ (row 4, plots (d), (h), and (l)). We define θ and ϕ in the text; ϕ_F is ϕ folded into one quadrant. The solid (dash) curve exhibits the results of fits 1 (2) in Table IV.4. Fit 1 (2) is to the SCHC angular distribution with $\sigma_L/\sigma_T = \xi^2 Q^2/m_\psi^2$ (=constant).

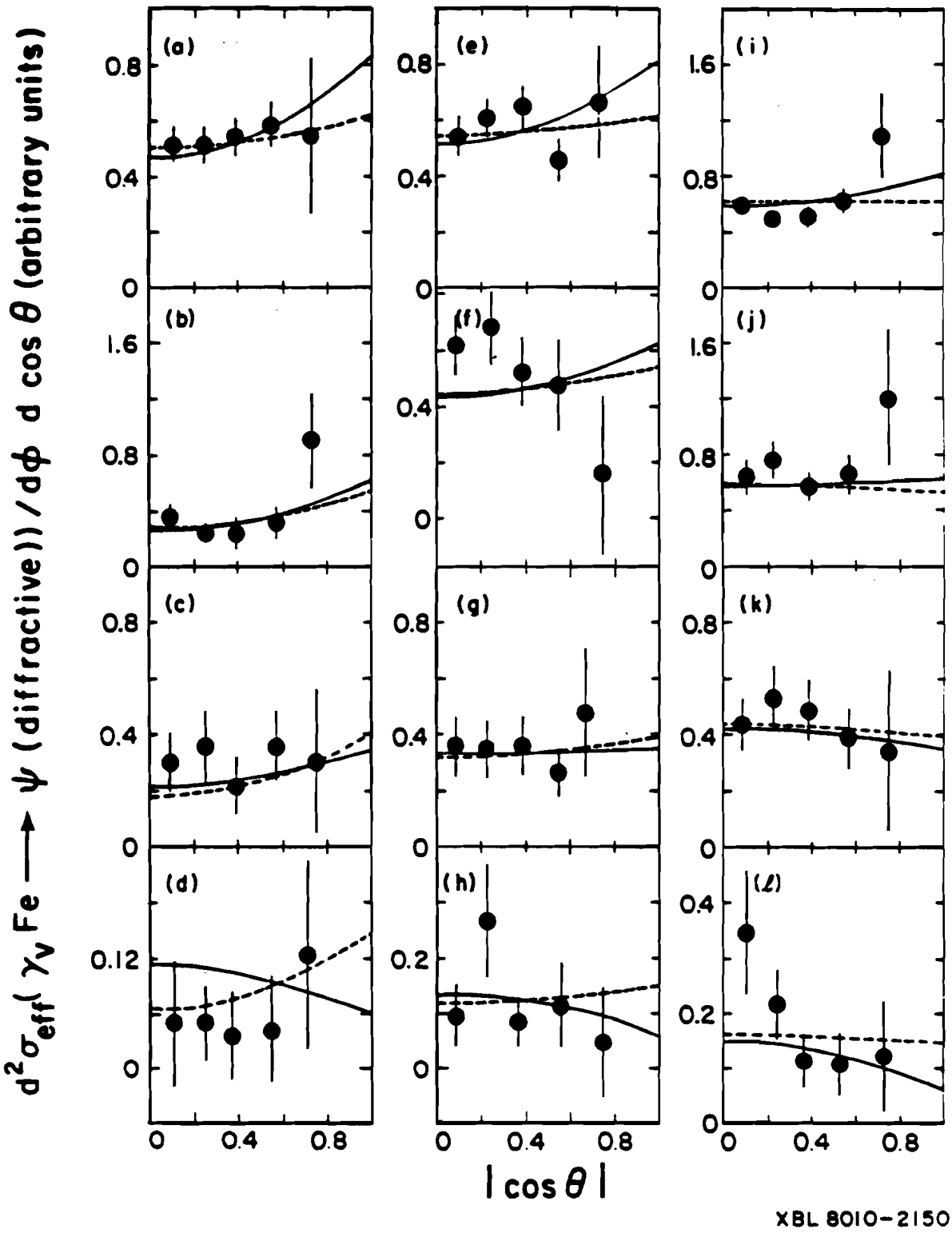

Figure IV.3 Angular dependence of $\sigma_{eff}(\gamma_V \mathrm{Fe} \rightarrow \psi X)$ for $E_X < 4.5$ GeV.

Figure IV.4 Angular dependence of the effective cross section for the reaction $\gamma_V \mathrm{Fe} \rightarrow \psi X$ (energy (X) < 4.5 GeV). Data and statistical errors are presented *vs.* $|\cos\theta|$ (left column) and ϕ_F (right column), where ϕ_F is ϕ folded into one quadrant; θ and ϕ are defined in the text. In (a) all data ($\langle Q^2 \rangle = 0.71$) are shown *vs.* $|\cos\theta|$, and data from all but the lowest Q^2 bin are shown *vs.* ϕ_F. Parts (b)–(e) divide the data into four Q^2 regions. Numbered solid lines exhibit the results of Fits 1–4 in Table IV.4. Fits 1, 2, and 4 are to the SCHC angular distribution with $\sigma_L/\sigma_T = \xi^2 Q^2/m_\psi^2$, constant, and zero, respectively; Fit 3 corresponds to the production of unpolarized ψ's. Each fit is made to all the data binned in Q^2, $|\cos\theta|$, and ϕ_F, with one adjustable normalization constant. For the purpose of display only, fits plotted *vs.* $|\cos\theta|$ (ϕ_F) have been summed over ϕ_F ($|\cos\theta|$) in the manner described in the text.

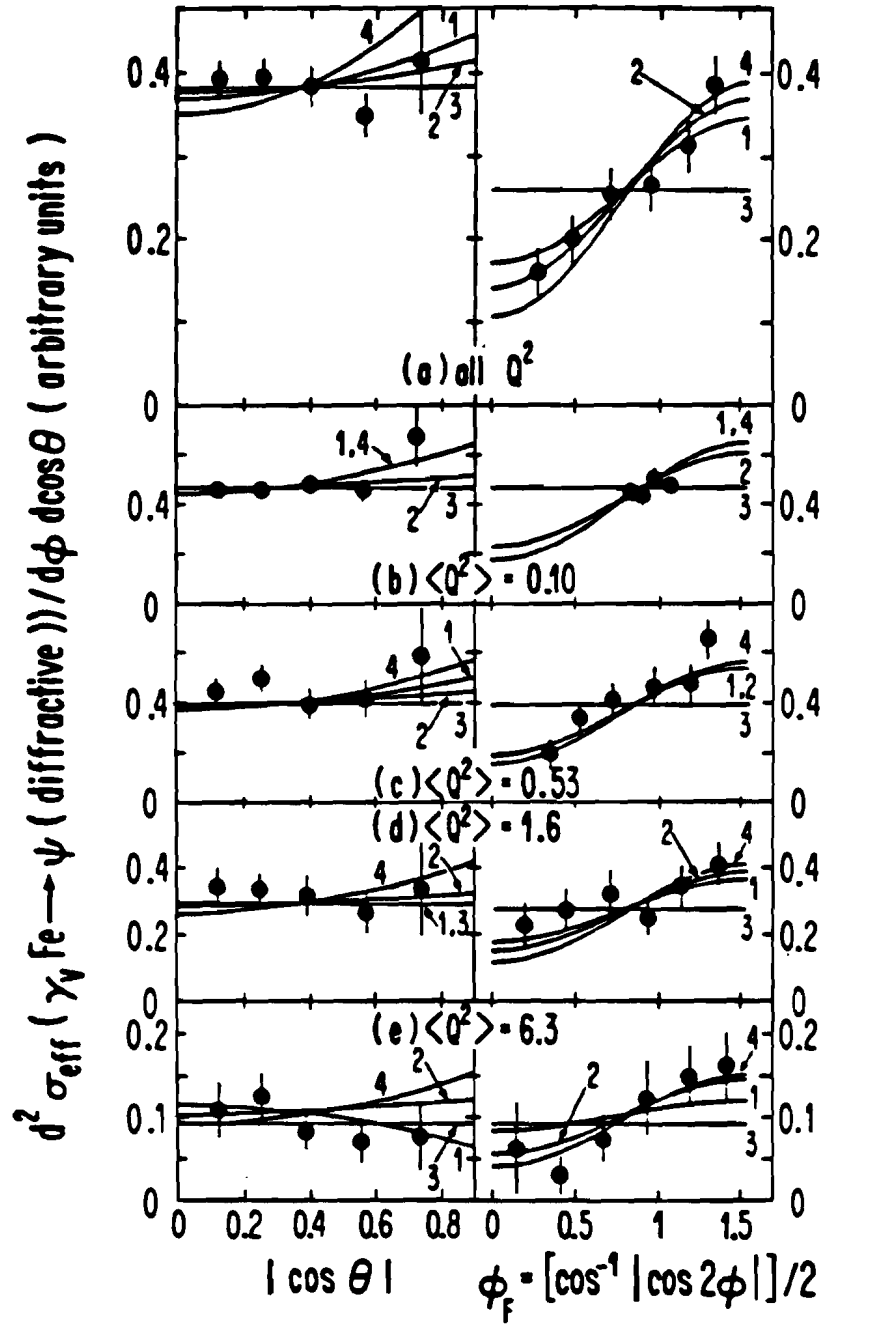

Figure IV.4 Angular dependence of $\sigma_{eff}(\gamma_V \mathrm{Fe} \rightarrow \psi X)$ for $E_X < 4.5$ GeV.

Figure IV.5 Q^2 dependence of the effective cross section for the reaction $\gamma_V \mathrm{Fe} \rightarrow \psi X$ (energy (X) <4.5 GeV). Statistical errors are shown. Typical Q^2 resolution is 3.1 (0.6) $(\mathrm{GeV}/c)^2$ at $Q^2 = 17$ (1.2) $(\mathrm{GeV}/c)^2$. The data are fit to $(1+Q^2/\mathrm{A}^2)^{-2}$ multiplied by the function $W(\eta, R)$ shown in Table IV.4. The best fits with free A (Table IV.4, Fit 1) and fixed A = 3.1 (Table IV.4, Fit 5) are shown. The data are normalized so that Fit 1 is unity at $Q^2 = 0$. Also exhibited is the γGF prediction (Table IV.4, Fit 7). The propagator fits are made to all data binned in Q^2, $|\cos\theta|$, and ϕ_F. For the purpose of display only, the data and these propagator fits have been summed over $|\cos\theta|$ and ϕ_F in the manner described in the text; this contributes to the *display* the weak Q^2-dependence of W arising from the Q^2 dependence of $R = \sigma_L/\sigma_T$ and the particular average values of the angular factors $\cos^2\theta$ and $\cos 2\phi$, as given in Table IV.3. The γGF fit has been done to the data as plotted. At high Q^2, Fits 5 and 7 are displayed as a solid band, with the upper (lower) edge indicating the result found by including (omitting) the screening factor $S(x')$. The curve representing Fit 1 has the fit value of $\mathrm{A} = 2.03^{+0.18}_{-0.12}$ GeV/c^2 when $S(x')$ is included, and the value $\mathrm{A} = 2.18^{+0.18}_{-0.13}$ GeV/c^2 when $S(x')$ is omitted.

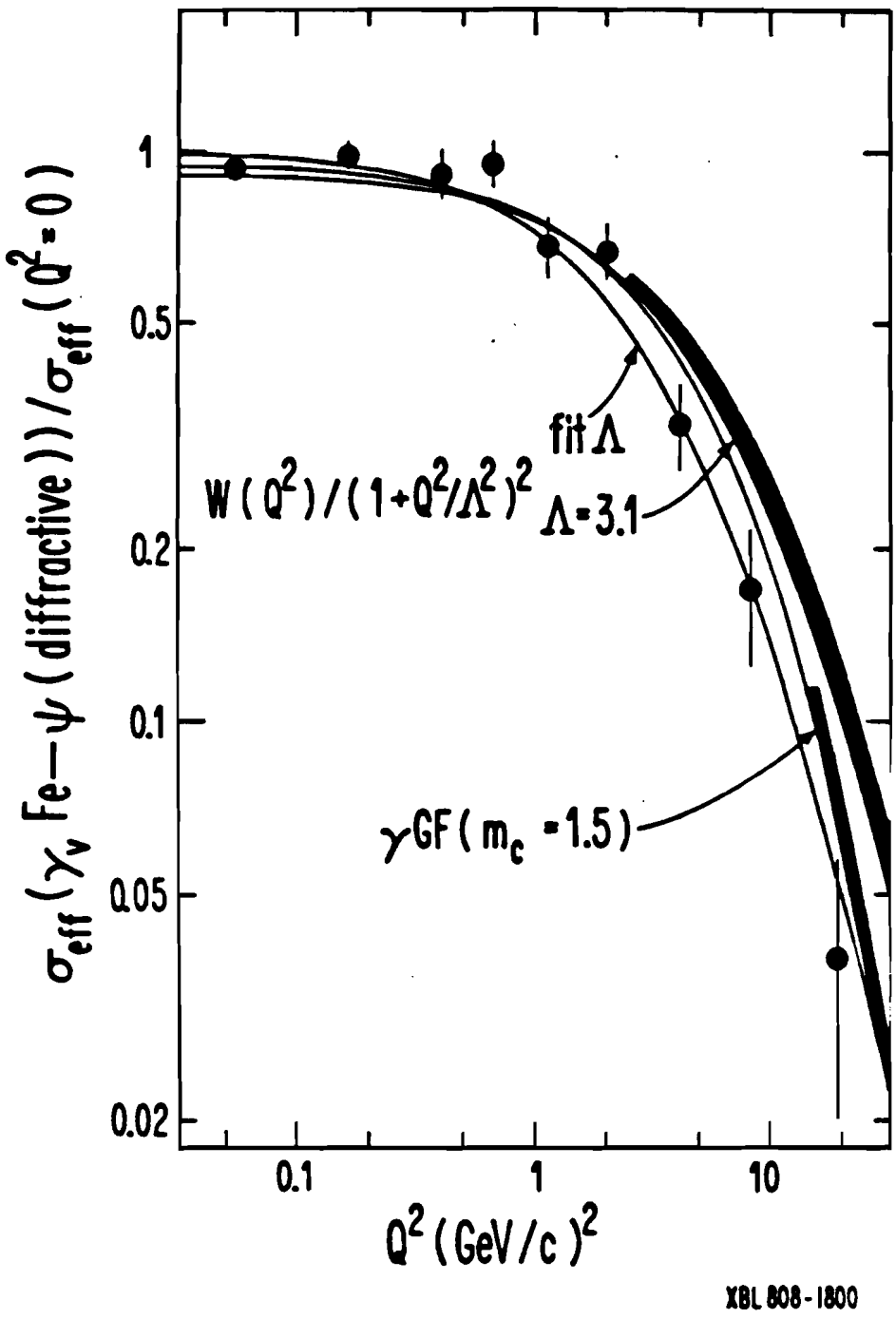

Figure IV.5 Q^2 dependence of $\sigma_{eff}(\gamma_V \mathrm{Fe} \to \psi X)$ for $E_X < 4.5$ GeV.

Figure IV.6 Part (a) displays the effective cross section σ_{eff} in nanobarns as a function of E_γ for the diffractive process $\gamma N \to \psi N$. These data are tabulated in Table IV.5(a). The results of Fits 3 (solid) and 5 (dash) from Table IV.6, extrapolated to $Q^2 = 0$, are plotted. The break in the curves arises from plotting the $E_\gamma < 25$ GeV data from a SLAC photoproduction experiment as published[29], while allowing for a relative normalization difference, consistent with quoted systematic errors, in the fits. In part (b) σ_{eff} is plotted as a function of E_γ for four Q^2 regions. These data are tabulated in Table IV.5(b). The curves plotted are the results of Fits 1 (dash) and 2 (solid) from Table IV.6, evaluated at the average Q^2 of each bin.

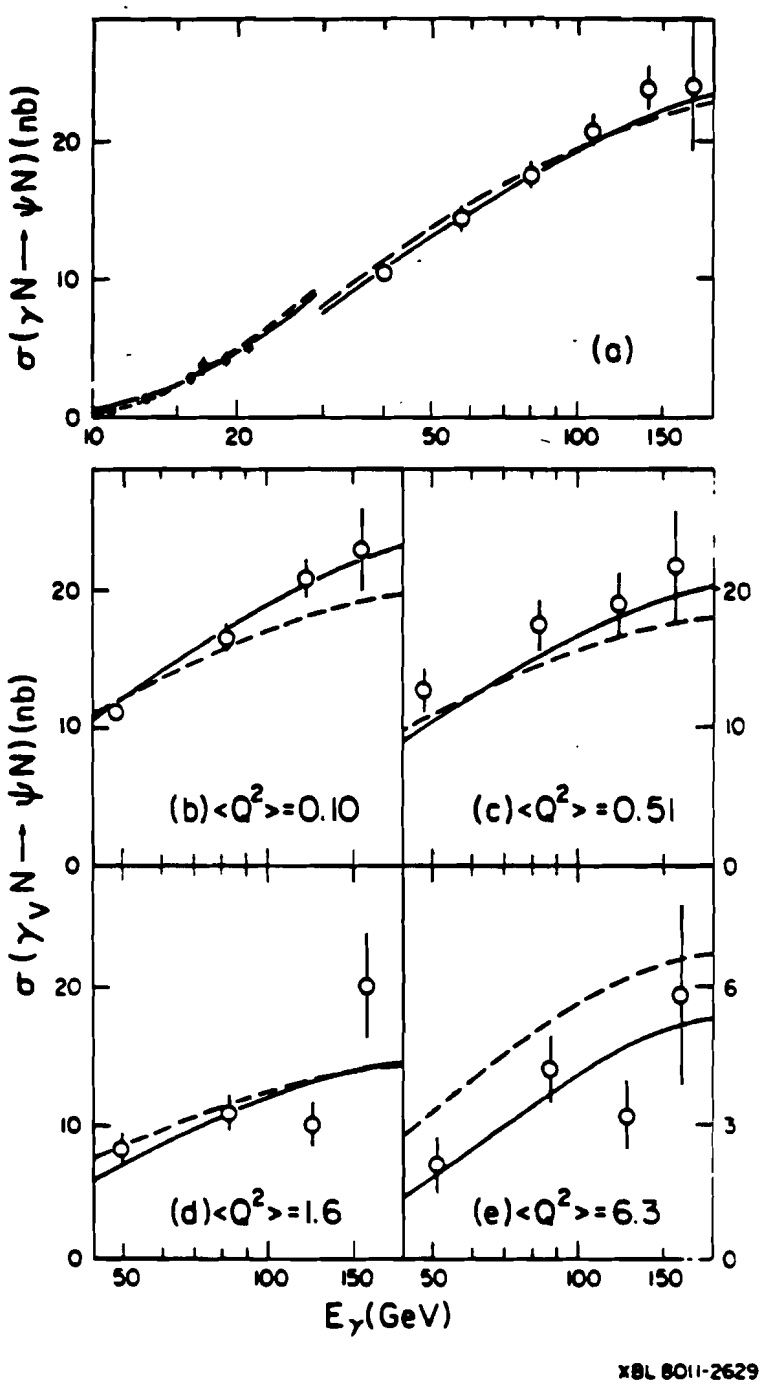

Figure IV.8 $\sigma_{eff}(\gamma N \to \psi N)$ as a function of E_γ.

Figure V.1 Part (a) displays the cross section, differential in elasticity $z \equiv E_\psi/E_\gamma$, in pb, for the process $\mu N \to \mu\psi X$ (energy (X)>4.5 GeV). The data have been corrected for elastic feed-down, as described on the text. Errors for $z < 0.7$ are statistical only; those for $z > 0.7$ have had the estimated error in the correction factor added in quadrature to the statistical error, whose contribution is indicated separately by horizontal marks on the error flag. We also show results[92] of the EMC muon experiment, normalized so as to minimize discrepency with our own data. Part (b) displays the effective cross section, differential in z and $p_\perp^2$, in arbitrary units, for the reaction $\gamma_V N \to \psi X$ (energy (X)>4.5 GeV), corrected as described above. In both parts, the solid line represents the result of an QCD based inelastic ψ photoproduction calculation. Also indicated are the contributions to the inelastic ψ sample we would expect from a MC simulation of the process $\mu N \to \mu\psi' N$, with $\psi' \to \psi X$, assuming $\sigma(\psi')/\sigma(\psi) = 0.38$. All plotted data are tabulated in Table V.1.

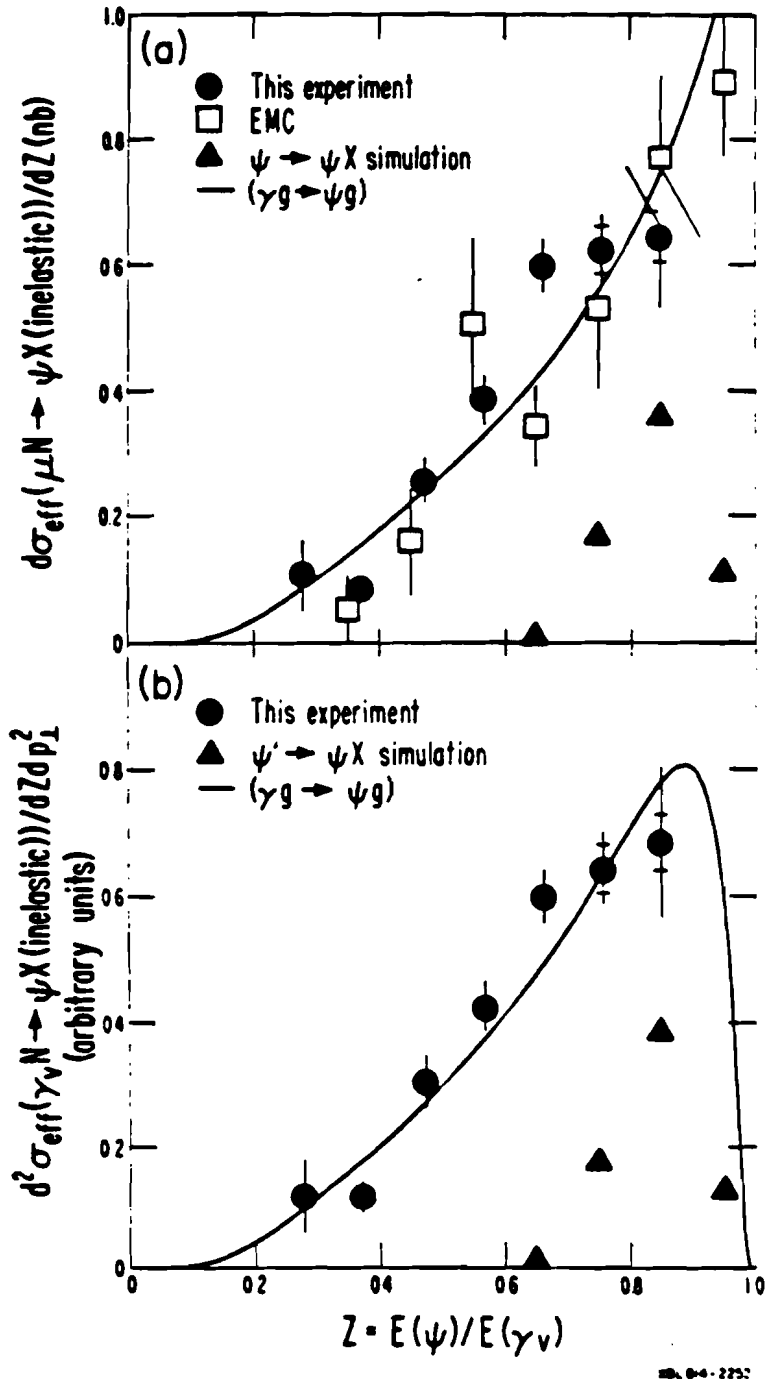

Figure V.1 The z dependence of σ_{eff} for inelastic ψ production.

Figure V.2 The effective cross section, differential in $\cos\theta$, for the reaction $\gamma_V \mathrm{Fe} \rightarrow \psi X$ ($E_X >$ 4.5 GeV), in arbitrary units. Results and statistical errors are presented *vs.* $|\cos\theta|$ for data with $0 < z < 0.7$ (left column) and $0.7 < z < 0.9$ (right column). In (a) all data are shown; parts (b) and (c) display the results for data having Q^2 less than or greater than 0.4(GeV/c)^2, respectively. The solid lines are fits to the results of the form $1 + \eta_C \cos^2\theta$. Plotted data and η_C values are listed in Table V.2.

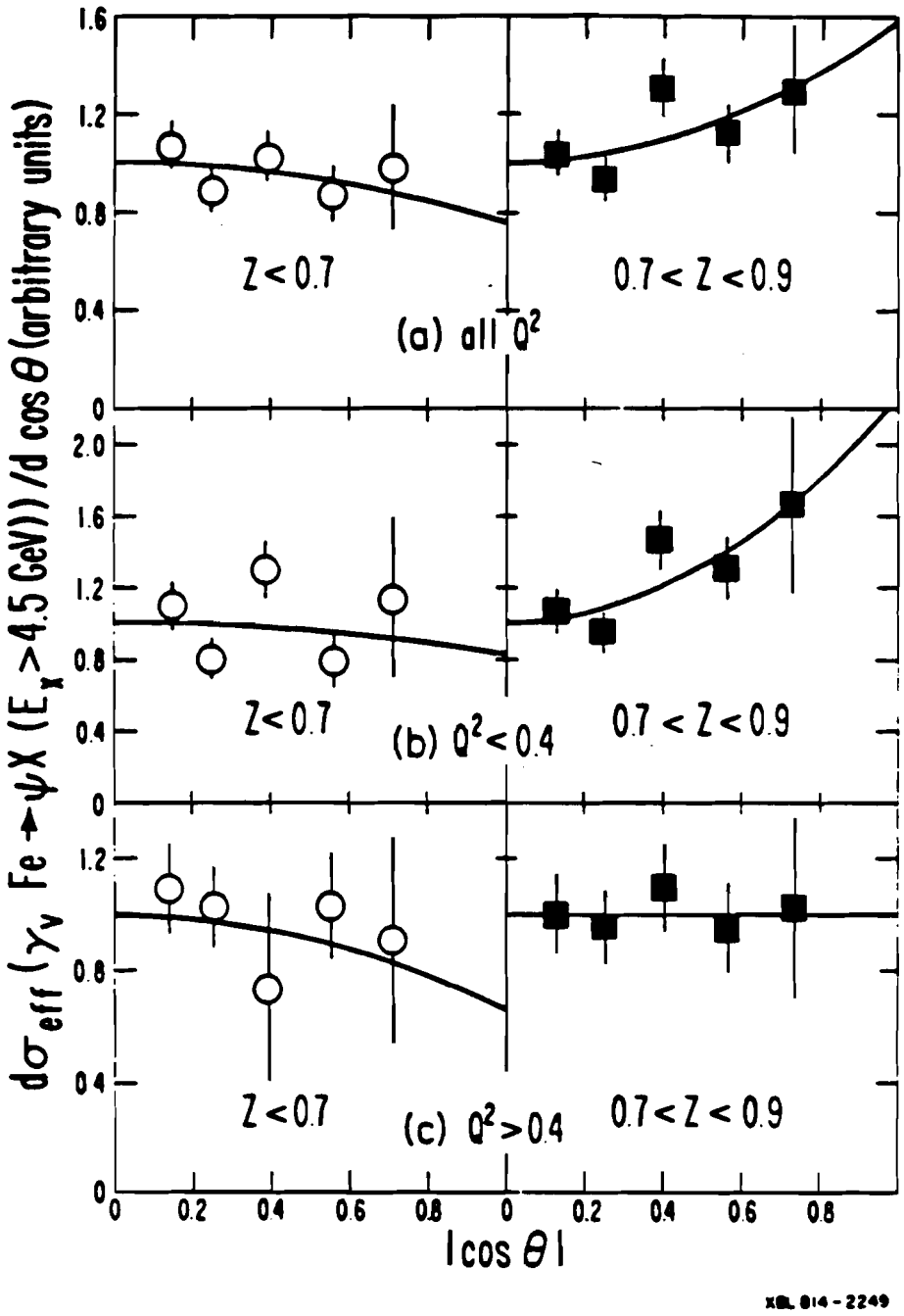

Figure V.2 $d\sigma_{eff}/d\cos\theta$ for the reaction $\gamma_V \mathrm{Fe} \rightarrow \psi X$ where $E_X > 4.5$ GeV.

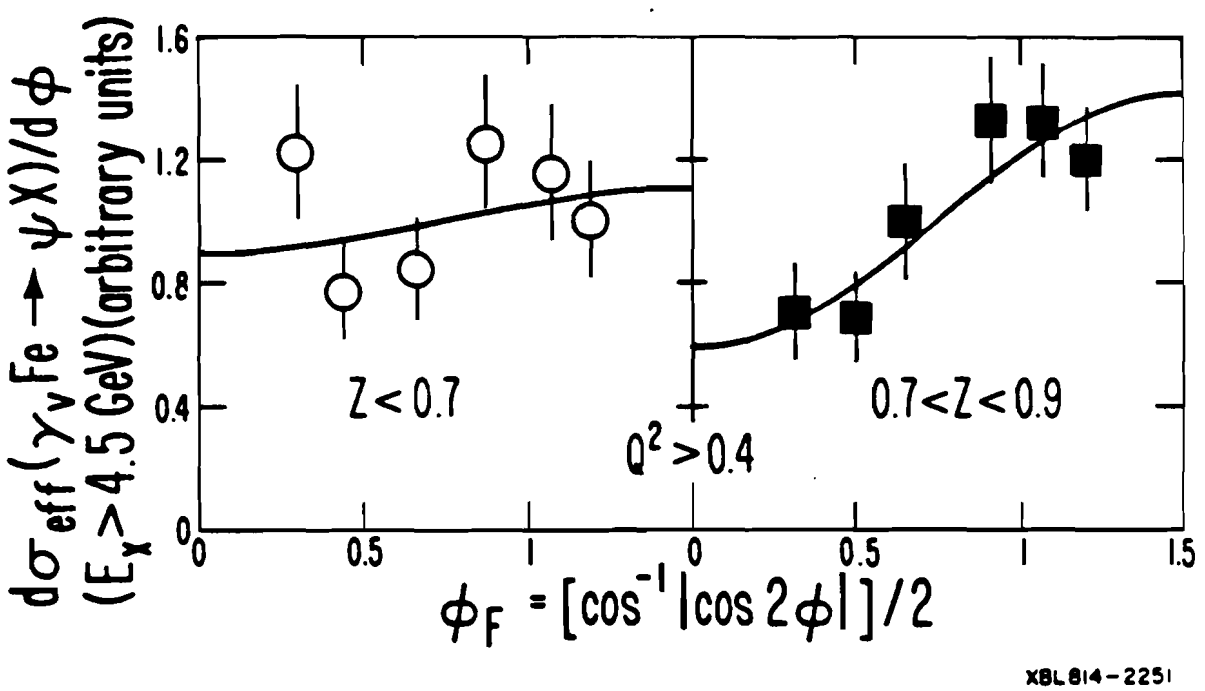

Figure V.3 The effective cross section, differential in ϕ, for the reaction $\gamma_V \mathrm{Fe} \rightarrow \psi X$ ($E_X >$ 4.5 GeV), in arbitrary units. Results and statistical errors are presented *vs.* ϕ_F for data satisfying $0 < z < 0.7$ (left column) and $0.7 < z < 0.9$ (right column). All data have $Q^2 > 0.4$(GeV/c)^2 to maintain adequate ϕ resolution. The solid lines represent fits to the data of the form $1 + \eta_A \cos 2\phi$. These data and the η_A values of the fits are listed in Table V.3.

Figure V.4 The effective cross section, differential in z and $p_\perp^2$, for the reaction $\gamma_V \mathrm{Fe} \rightarrow \psi X$ ($E_X > 4.5$ GeV) in arbitrary units. Data and statistical errors are presented *vs.* $p_\perp^2$ of the ψ, measured with respect to the γ_V momentum, for the elasticity regions $0 < z < 0.7$ (part (a)) and $0.7 < z < 0.9$ (part (b)). The solid curve is the result of $\gamma g \rightarrow \psi g$ calculation which attempts to describe inelastic ψ photoproduction. Table V.4 provides a tabulation of the data which is plotted here.

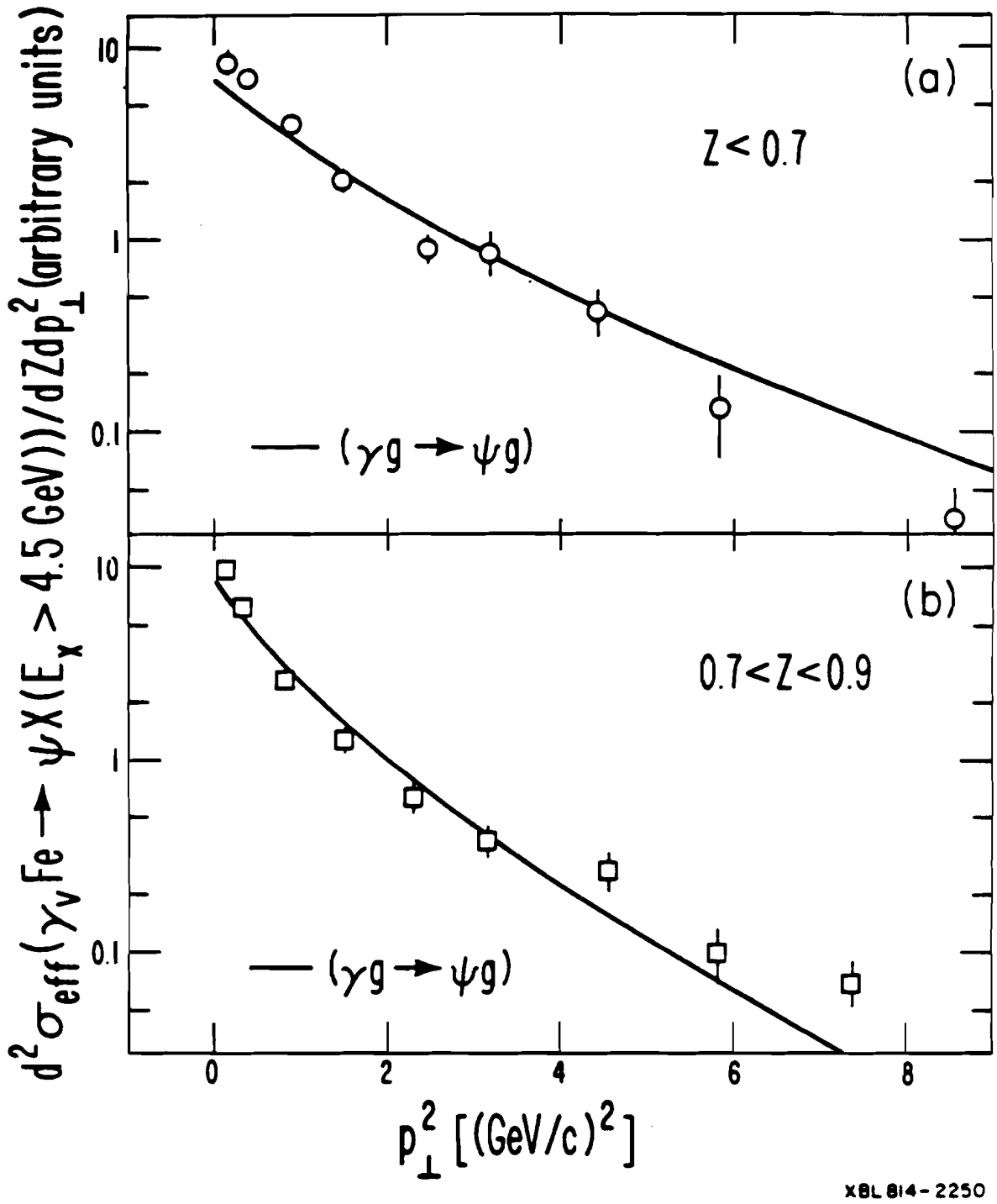

Figure V.4 The $p_\perp^2$ dependence of $d^2\sigma_{eff}/dzdp_\perp^2$ for inelastic ψ production.

Figure V.5 The Q^2 dependence of the effective cross section for the reaction $\gamma_V \mathrm{Fe} \rightarrow \psi X$ ($E_X >$ 4.5 GeV), normalized to unity at $Q^2 = 0$. Data and statistical errors are presented for the elasticity regions $z < 0.7$ (open circles), $0.7 < z < 0.9$ (filled squares), and $z < 0.9$ (filled circles). Also shown is the result from another inelastic ψ muoproduction experiment[92] (open squares). The data are fit to $(1 + Q^2/\mathrm{A}^2)^{-2}$; the resulting values of A, measured in GeV/c^2, are indicated. Table V.5 lists the data plotted here.

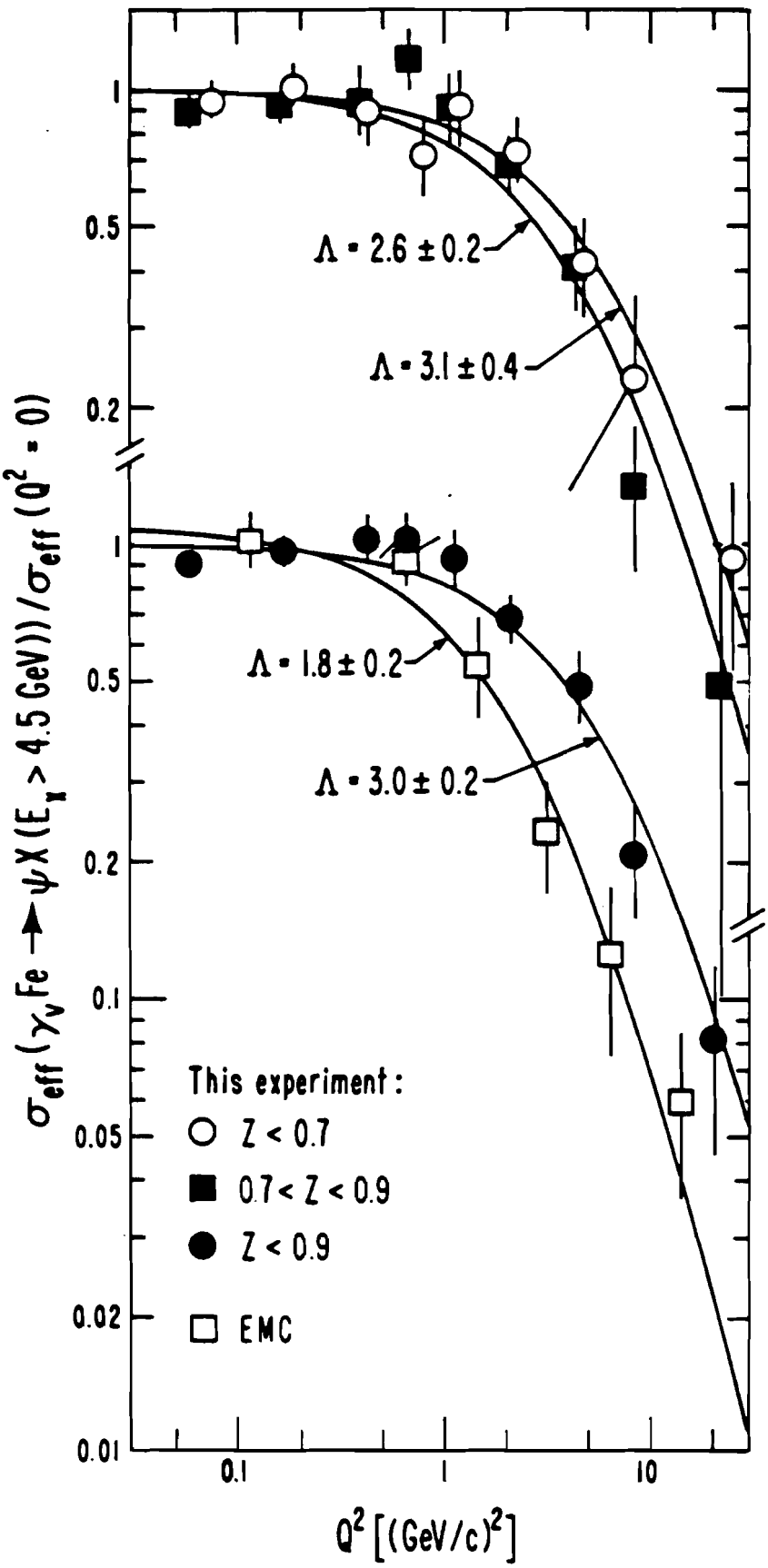

Figure V.5 The Q^2 dependence of $\sigma_{eff}(\gamma_V \mathrm{Fe} \rightarrow \psi X)$ for $E_X > 4.5$ GeV.

Figure V.6 The E_γ dependence of the effective cross section for the reaction $\gamma N \rightarrow \psi X$. The data for which $E_X > 4.5$ GeV have been corrected for contributions from elastic events and the results extrapolated to $Q^2 = 0$. The data, thus labeled as inelastic ψ photoproduction, and statistical errors are presented *vs.* E_γ for the elasticity regions $z < 0.7$ (part (b)), $0.7 < z < 0.9$ (part (c)), and $z < 0.9$ (part (a)). The data for which $z > 0.9$ have been excluded because of uncertainties in the large elastic feed-down correction and acceptance measurement. Also shown in part (a) are the results[92] of the EMC for inelastic ψ muoproduction, multipled by 0.726 – the fraction of events they observe with $z < 0.9$. The solid curve in each part of the figure is the result of a $\gamma g \rightarrow \psi g$ calculation which attempts to describe inelastic ψ photoproduction. The absolute normalization of the prediction has been increased by the indicated factor to maximize agreement with the data. The dash curve is the result of a fit to the E_γ dependence of the elastic ψ production data of Figure IV.6, adjusted in normalization in each z region by the indicated amount. Table V.6 lists the data plotted here.

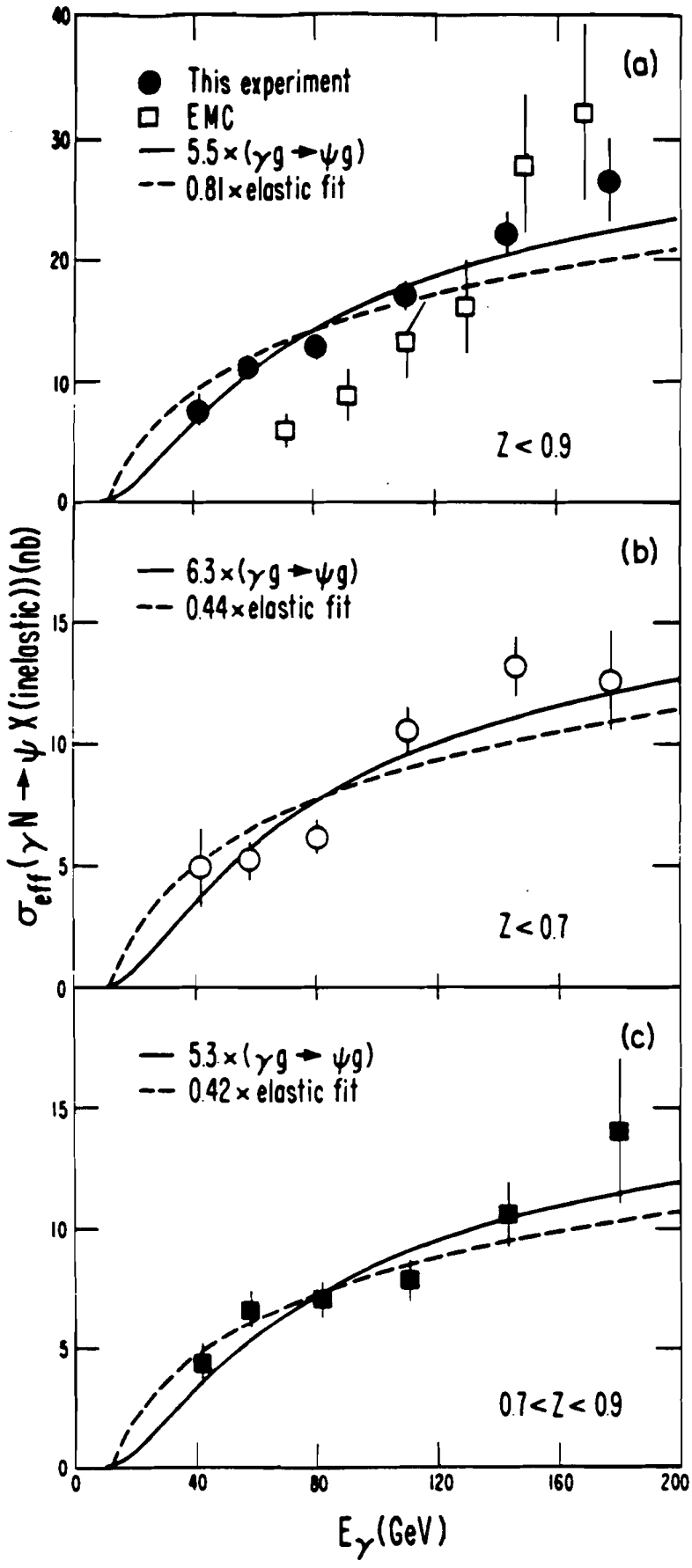

Figure V.8 The E_γ dependence of $\sigma_{eff}(\gamma N \to \psi X)$ for inelastic ψ production.